OPTICAL HYPERPOLARIZATION AND DETECTION OF ELECTRON AND NUCLEAR SPINS OF PHOSPHORUS DONORS IN HIGHLY ENRICHED ^{28}SI

by

Albion Yang

B.Sc., University of Manitoba, 2003

Thesis submitted in partial fulfillment

of the requirements for the degree of

Doctor of Philosophy

in the department

of

Physics

SIMON FRASER UNIVERSITY

Summer 2010

APPROVAL

Name: Albion Yang

Degree: Doctor of Philosophy

Title of Thesis: Optical Hyperpolarization and Detection of Electron and Nuclear Spins of Phosphorus Donors in Highly Enriched ^{28}Si

Examining Committee: Dr. Karen Kavanagh, Professor (Chair)

Dr. Michael L. W. Thewalt, Professor
Senior Supervisor

Dr. Simon P. Watkins, Professor
Supervisor

Dr. George Kirczenow, Professor
Supervisor

Dr. Patricia M. Mooney, Professor
Internal Examiner

Dr. Joshua A. Folk, Assistant Professor
University of British Columbia
External Examiner

Date Approved: May 28, 2010

Declaration of
Partial Copyright Licence

Abstract

The linewidths of optical transitions associated with shallow impurities have been shown in recent studies to be much narrower in isotopically enriched ^{28}Si as compared to natural Si. This is true of the no-phonon P donor bound exciton transition in ^{28}Si, and using photoluminescence excitation spectroscopy, fine structure previously not seen in natural Si is revealed. Under a small external magnetic field, the P bound exciton transition shows a complicated structure consisting of six sets of doublets, with the doublet splitting being due to the splitting of the donor ground state by the hyperfine interaction between the spin of the donor electron and that of the ^{31}P nucleus. The electron spin populations and the ^{31}P nuclear spin populations can be determined by measuring the relative intensities of the hyperfine components in the photoluminescence excitation spectrum. Additionally, the predominant Auger recombination channel of these bound excitons is used to observe the same resolved hyperfine components in the photocurrent spectrum. By selectively ionizing donors in a specific hyperfine state via optical pumping of a specific hyperfine component, large polarizations of the electron and nuclear spins of ^{31}P donors can be achieved at low field. Electron and nuclear polarizations of 90% and 76%, respectively, are obtained in less than a second, providing an initialization mechanism for qubits based on these spins, and enabling further ESR and NMR studies on dilute ^{31}P in ^{28}Si. A measurement of the homogeneous linewidth of the transitions associated with the ^{31}P bound exciton, determined by spectral hole burning, is also presented. The observed 10 neV linewidth is only four times the limit set by the bound exciton lifetime.

For my parents

Acknowledgments

First of all, I would like to express my deepest gratitude to my Ph.D. supervisor, Prof. Michael Thewalt, for the excellent mentorship that he has provided me over the past several years. I have greatly benefited from his exceptional experimental skills, his ability to explain things clearly and simply, and his enthusiasm for science.

I would like to thank my colleagues, Michael Steger and Dr. Takeharu Sekiguchi, for the help they provided me on many occasions, and for making 'the grotto' a more enjoyable place in which to work.

For their generous financial support, I would like to thank the Natural Sciences and Engineering Research Council of Canada (NSERC), Simon Fraser University, and Prof. Michael Thewalt.

A very special thanks goes to my close friend Ingrid, who was my greatest source of inspiration while writing this thesis.

Finally, I would like to thank my parents and my sisters for all the support they have provided me throughout my life.

Contents

Approval ii

Abstract iii

Dedication iv

Acknowledgments v

Contents vi

List of Tables viii

List of Figures ix

1 Introduction 1

1.1 Isotopically enriched silicon 1

1.2 Photoluminescence excitation spectroscopy of ^{28}Si 4

2 Theoretical Background 5

2.1 Silicon 5

2.2 Shallow donor impurities in silicon 8

2.3 Donor bound excitons in silicon 14

2.4 The phosphorus donor hyperfine interaction 19

3 Experimental Methods 21

3.1 ^{28}Si Samples 21

3.2 The PLE apparatus 24
3.2.1 Excitation sources 24
3.2.2 Locking and scanning system 27
3.2.3 Cryostat, magnet, and monochromator 30
3.2.4 Data collection 31
3.3 Alternative methods of measuring the ^{31}P D^0X spectrum 33
3.3.1 Photoconductivity measurement of bound exciton spectra . . 33
3.3.2 Laser absorption method 35

4 Experimental Results and Discussion **37**
4.1 ^{31}P bound exciton spectrum in ^{28}Si 38
4.1.1 ^{31}P bound exciton spectrum at zero magnetic field 40
4.1.2 ^{31}P bound exciton spectrum at low to intermediate magnetic field 46
4.1.3 The forbidden transitions 54
4.1.4 Photoconductivity measurement of ^{31}P bound exciton spectrum 58
4.1.5 Measurement of ^{31}P bound exciton spectrum by laser absorption 60
4.1.6 Possible applications in quantum computing 63
4.2 Hyperpolarization of the electron and nuclear spin states of ^{31}P donors in ^{28}Si 64
4.2.1 Preliminary attempts at obtaining electron and nuclear spin polarizations in p-type ^{28}Si 64
4.2.2 Hyperpolarization of electron and nuclear spins in n-type ^{28}Si 67
4.2.3 Nuclear polarization dynamics 77
4.2.4 Polarization of electron and nuclear spins in p-type ^{28}Si measured using the capacitive photoconductivity method 79
4.3 Homogeneous linewidth of the ^{31}P D^0X transition in silicon 82
4.3.1 Hole burning in ^{nat}Si 82
4.3.2 Hole burning in ^{28}Si under an applied magnetic field 84

5 Conclusions **90**

Bibliography **93**

List of Tables

3.1 List of ^{28}Si samples 22

4.1 D^0 populations and net electron and nuclear polarizations for dynamic pumping in n-type ^{28}Si 75

4.2 Polarization time and recovery time at different magnetic fields 78

4.3 Net electron and nuclear polarizations for optical pumping in p-type ^{28}Si 81

List of Figures

2.1 Crystal structure of silicon 6
2.2 Schematic band structure for silicon along the [001] direction 7
2.3 Surfaces of constant energy near the conduction band minimum in each of the six equivalent [001] directions 8
2.4 Schematic diagram of the donor electron wave function in real space . 10
2.5 Schematic diagram of some of the bound states of a shallow donor electron 12
2.6 Energy level diagram of transitions between D^0 and D^0X 17

3.1 PLE apparatus 25
3.2 PLE pump and probe systems 26
3.3 Locking and scanning system 28
3.4 PL spectrum showing the no-phonon and TO phonon-assisted ^{31}P D^0X transitions for an n-type sample of ^{28}Si 32
3.5 Photoconductivity method 34
3.6 Contactless capacitive photoconductivity method 34
3.7 Laser absorption method 36

4.1 PLE spectrum of the no-phonon ^{31}P D^0X transition for the p-type ^{28}Si a sample 39
4.2 Comparison of ^{31}P D^0X PLE spectra for a p-type sample of ^{28}Si at different levels of above-gap excitation 41
4.3 Comparison of ^{31}P D^0X PLE spectra at different sample temperatures 42

4.4 Plot of the natural log of the peak intensity ln(I) of the ^{31}P D^0X PLE spectrum versus 1/T 44
4.5 Comparison of ^{31}P D^0X spectra for four ^{28}Si with different ^{31}P concentrations 45
4.6 PLE spectrum of the no-phonon ^{31}P $D^0 \rightarrow D^0$X transitions for the ^{28}Si a sample under an applied magnetic field 47
4.7 Energy level diagram of the ^{31}P $D^0 \rightarrow D^0$X transitions under an applied magnetic field 48
4.8 Dependence of the ^{31}P D^0X PLE line shapes on temperature and isotopic enrichment 50
4.9 Comparison of ^{31}P D^0X spectra under an applied magnetic field for different levels of above-gap excitation 52
4.10 PLE spectra of the ^{31}P D^0X for the n-type ^{28}Si:P 3.3.6 sample at different magnetic fields 53
4.11 PLE spectrum of the ^{31}P D^0X for the n-type ^{28}Si:P 3.3.6 sample under a magnetic field 55
4.12 PLE spectrum of the ^{31}P D^0X for the n-type ^{28}Si:P 3.3.6 sample with a magnetic field of 100 G parallel to the [001] axis 57
4.13 Photocurrent spectrum of the ^{31}P D^0X under an applied magnetic field 59
4.14 Transmittance spectrum of the ^{31}P D^0X for an n-type ^{28}Si sample . . 61
4.15 Transmittance spectrum of the ^{31}P D^0X under an applied magnetic field for an n-type ^{28}Si sample 62
4.16 Polarization of electron and nuclear spin states in a p-type sample of ^{28}Si by optical pumping 66
4.17 Zeeman level diagram of $D^0 \rightarrow D^0$X transitions 69
4.18 Hyperpolarization of electron and nuclear spin states by optical pumping in n-type ^{28}Si 70
4.19 PLE spectrum of the ^{31}P D^0X for the n-type ^{28}Si:P 3.3.6 sample under an applied magnetic field with no above-gap excitation 71
4.20 Effects of above-gap excitation on ^{31}P D^0X spectrum in n-type ^{28}Si under an applied magnetic field 72
4.21 Stark broadening in n-type ^{28}Si 74

4.22 Nuclear polarization dynamics 78
4.23 Photoconductance spectra of the ^{31}P D^0X in p-type ^{28}Si with optical pumping 80
4.24 Hole burning in ^{nat}Si 83
4.25 Hole burning in ^{28}Si 85
4.26 Schematic diagram of hole burning with the pump laser tuned to the centre of the (5,6) transition 87
4.27 Plot of spectral hole width versus pump laser power 89

Chapter 1

Introduction

1.1 Isotopically enriched silicon

The elemental semiconductors carbon (diamond), germanium, and silicon in their natural form consist of mixtures of two or more stable isotopes. This is also seen in almost all compound semiconductors, where one or more of the constituent elements have similar isotopic mixtures. Silicon (Si), the most well-known semiconductor, consists of three stable isotopes: ^{28}Si, ^{29}Si, and ^{30}Si, with natural abundances of 92.23%, 4.67%, and 3.10%, respectively. The effects of isotopic composition on the vibrational, thermal, and electronic properties of semiconductors is a subject that has led to numerous recent studies, the results of which have been summarized in several comprehensive reviews [1–6]. The first isotopically purified semiconductors to be available in the form of bulk single crystals of reasonable purity were germanium (Ge) and diamond (C). Their availability allowed for the investigation of isotope effects on thermal conductivity, phonon energies and lifetimes, and electronic band gaps [1–19]. The isotope effect on band gap energy was first reported [7] for the case of ^{13}C vs. ^{12}C diamond, where it was shown that the band gap energy E_g has a dependence on the average isotopic mass $\bar{M}$. This is due to two separate effects: first, the renormalization of E_g by the electron-phonon interaction, and second, the dependence of the lattice constant on $\bar{M}$, which leads to a change in E_g through the hydrostatic deformation potential. Both effects vary as $\bar{M}^{-1/2}$ and the electron-phonon term, which is dominant, is often treated (approximately) as the only term.

The isotopic effects on the electronic properties of diamond and Ge were able to be explained within the virtual crystal approximation (VCA), which considers only the average isotopic mass, ignoring the effects of randomness. In the VCA, the actual crystal is approximated by a hypothetical one with identical constituent atoms (for a given chemical species in compound semiconductors) having the average isotopic mass.

Until recently, studies on isotope effects in Si had been limited to Raman scattering [20, 21] and thermal conductivity [22] due to the lack of samples of sufficient purity to study the isotope effects on indirect band gap transitions. When a high purity bulk sample of Si (enriched to 99.896% ^{28}Si) finally became available, the first study [23] using photoluminescence (PL) spectroscopy revealed significantly sharper no-phonon impurity bound exciton (BE) transition lines compared to those seen in natural Si ($^{\mathrm{nat}}$Si). In $^{\mathrm{nat}}$Si, the no-phonon phosphorus (P) donor BE transition has a linewidth of $0.041\,\mathrm{cm}^{-1}$ ($5.1\,\mu\mathrm{eV}$) full width at half maximum (FWHM), whereas the observed linewidth of the same transition in the highly enriched ^{28}Si sample was $0.014\,\mathrm{cm}^{-1}$ ($1.7\,\mu\mathrm{eV}$) FWHM, essentially identical to the maximum available instrumental resolution of the Fourier transform spectrometer used in the study. It appeared that the BE linewidth in $^{\mathrm{nat}}$Si was limited by inhomogeneous isotope broadening, an effect not accounted for within the VCA. This inhomogeneous broadening inherent in $^{\mathrm{nat}}$Si was attributed to local fluctuations in the band gap energy resulting from statistical fluctuations of the local isotopic composition within the effective volume of the BE of radius $\sim$3.5 nm. In the same study, it was found that there exists a $0.92\,\mathrm{cm}^{-1}$ ($110\,\mu\mathrm{eV}$) decrease in the indirect band gap energy of the highly enriched ^{28}Si sample relative to $^{\mathrm{nat}}$Si, which was explained as being due mainly to the renormalization of E_g by the electron-phonon interaction. Shifts of the wave vector conserving phonon energies were also observed.

A similar dramatic reduction of the linewidths in ^{28}Si was observed for the components of the no-phonon boron (B) BE transition, as well as for the no-phonon transitions of the deeper acceptors aluminum, gallium, and indium [24–26]. In addition to sharper PL lines, the infrared absorption resulting from transitions between the electronic ground state of neutral donor and acceptor impurities and their bound excited states revealed many transitions with reduced linewidths in ^{28}Si as compared

to ^{nat}Si [27–29]. Reductions in the linewidths of infrared absorption transitions were later seen in highly enriched ^{28}Si for the deep donors sulfur and selenium, yielding some of the narrowest impurity absorption transitions ever seen in any semiconductor [30, 31]. More recently, PL studies [32–35] on copper-related impurity centres in ^{28}Si have led to the discovery of four- and five-atom complexes in Si that contain combinations of copper, silver, gold, platinum and lithium atoms, thanks to the greatly reduced linewidths of the PL transitions associated with these centres in ^{28}Si as compared to ^{nat}Si.

As discussed earlier, the BE linewidths in ^{28}Si were narrower than the instrumental resolution available with a Fourier transform PL apparatus having the highest resolution available in that spectral region of any commercially available system. The only solution to this problem was to construct a new apparatus capable of providing a significant increase in resolution.

1.2 Photoluminescence excitation spectroscopy of ^{28}Si

The method of photoluminescence excitation (PLE) spectroscopy, using a tunable single-frequency laser source with sub-MHz linewidth, provides a huge increase in instrumental resolution compared to the Fourier transform PL method and is more than adequate to resolve the BE linewidths in ^{28}Si. In PL spectroscopy, above band gap excitation is used to generate bound excitons, while in PLE spectroscopy, a resonant laser source is scanned across the no-phonon BE transitions, and the very weak absorption in which BEs are created is monitored by observing the resulting PL in the relatively strong transverse-optical wave vector conserving phonon replica, which is well separated in energy from the no-phonon region.

PLE spectroscopy has previously been applied to the experimental determination of the band gap dependence on temperature in the limit of T$\rightarrow$0 [36]. By measuring the temperature shift of the remarkably sharp BE transitions in ^{28}Si across the liquid-He temperature region, the low-T behaviour of the silicon band gap was determined to vary as T^4. PLE spectroscopy has also been used to observe [37] the ^{10}B–^{11}B isotope splitting in the spectrum of the boron BE in ^{28}Si, and in this same PLE spectrum, several transition lines not previously resolved in the PL spectroscopy of ^{28}Si [23] were observed.

In this thesis, we present results obtained from the PLE spectroscopy of the P donor BE in ^{28}Si. We were able to observe the zero-field hyperfine splitting of the P donor ground state, and this led to an investigation of the P BE transition under an applied magnetic field, which subsequently resulted in our optical pumping experiments that produced hyperpolarizations of the electron and nuclear spins of ^{31}P donors. When we first set out to study the P donor BE transition in ^{28}Si using the new PLE apparatus, our goal was to determine the ultimate linewidth limit of the P BE transition with the removal of inhomogeneous isotope broadening in ^{28}Si samples of higher isotopic purity, but as new and surprising results were uncovered along the way, our goals expanded to include the measurement of quantities relevant for quantum computing schemes based on the spin states of ^{31}P donors in ^{28}Si [38–40].

Chapter 2

Theoretical Background

The basic concepts of impurities and impurity bound excitons in semiconductors relevant for this study are discussed in this chapter. Since phosphorus is the only impurity in silicon studied in this thesis, the discussion in this chapter focuses mainly on donor impurities and donor bound excitons.

2.1 Silicon

Silicon crystallizes in a diamond structure (shown in FIG. 2.1), where each atom sits at the centre of a tetrahedron built from its four nearest neighbours [41]. The lattice is face-centered cubic (fcc) with basis atoms located at (0,0,0) and at one quarter of the diagonal length along the [111] direction at $(\frac{a}{4},\frac{a}{4},\frac{a}{4})$, where $a = 5.43\,\text{Å}$ [42] is the lattice constant of silicon. The first Brillouin zone of the fcc lattice has three high-symmetry directions, along [001], [110], and [111].

The Brillouin zone of the fcc lattice is highly symmetrical and is invariant under various symmetry operations such as rotations about certain axes and reflections through certain planes. The transformation properties under certain symmetry operations of the crystal can be determined from group theory, and can be used to classify wave functions in crystals and deduce the selection rules for operators acting on these wave functions. Additionally, the symmetry properties at important points in the electronic energy band structure in the Brillouin zone can be obtained using group theory. [41, 43]

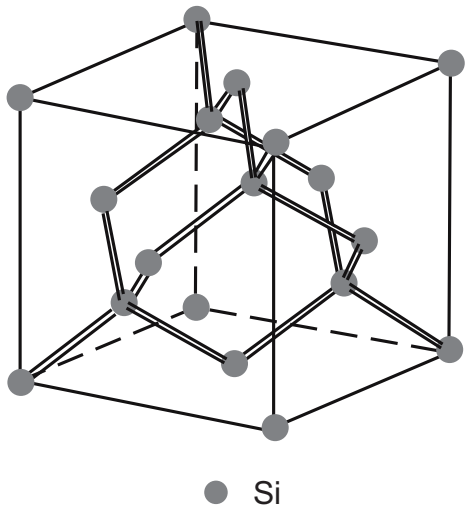

Figure 2.1: A unit cell of the face-centered cubic lattice with silicon basis atoms at (0,0,0) and at $(\frac{a}{4},\frac{a}{4},\frac{a}{4})$, where $a = 5.43\,\text{Å}$ [42] is the lattice constant of silicon. [43]

The band structure of the highest valence band and the lowest conduction band along the [001] direction in silicon is shown schematically in FIG. 2.2. The maximum of the valence band occurs at the Brillouin zone center ($\mathbf{k} = 0$) and a minimum of the conduction band is seen to occur at approximately 85% of the distance to the zone boundary along the [001] direction, so the band gap E_g of silicon is an indirect one. Since the conduction band minimum lies outside the $\mathbf{k} = 0$ point, symmetry considerations suggest that a number of equivalent extrema must also be present. Silicon belongs to the cubic O_h symmetry group, and as a result, has a conduction band minimum along each of the six equivalent directions: [001], [00$\bar{1}$], [010], [0$\bar{1}$0], [100], and [$\bar{1}$00]. This is called the many-valley structure, and near the conduction band minimum, the surfaces of constant energy are ellipsoids of revolution with a long axis in each of the six equivalent directions as shown in FIG. 2.3. [41, 43]

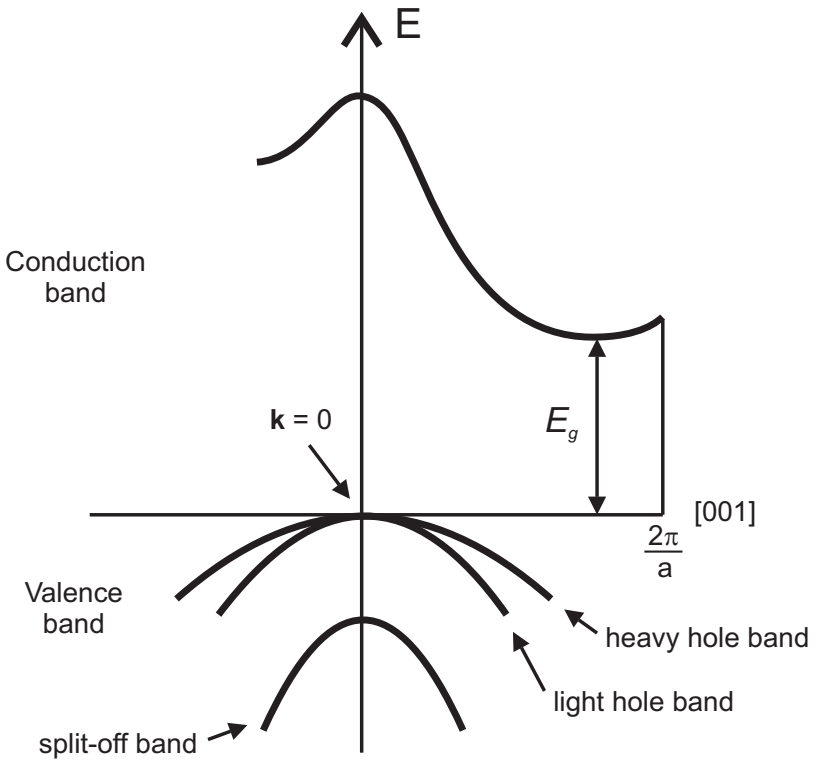

Figure 2.2: Schematic band structure for silicon along the [001] direction. Silicon has an indirect band gap E_g ($= 1.17\,\text{eV}$ at $4.2\,\text{K}$ [42]), with the valence band maximum at the Brillouin zone centre ($\mathbf{k} = 0$) and the conduction band minimum at approximately 85% of the distance to the zone boundary along the [001] direction. The spin-orbit interaction splits the j_h=1/2 valence band (referred to as the split-off band) from the j_h=3/2 bands (referred to as the light hole and heavy hole bands).

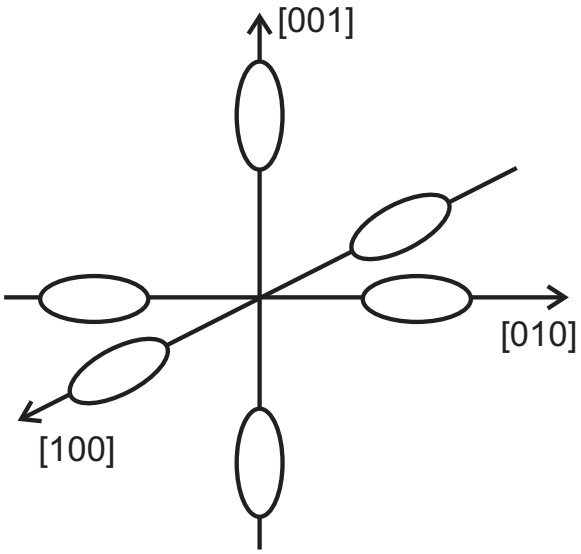

Figure 2.3: The ellipsoids represent surfaces of constant energy near the conduction band minimum in each of the six equivalent [001] directions.

2.2 Shallow donor impurities in silicon

Phosphorus (P) is a group V substitutional shallow donor in silicon (Si) that has one extra proton and one extra electron compared to the Si atom. The attractive Coulomb potential between this extra valence electron and the P nucleus is screened by the core electrons of the P atom as well as the remaining four valence electrons and all of the valence electrons of neighbouring Si atoms. The screened Coulomb potential seen by the extra valence electron can be approximated by that due to a proton screened by the valence electrons of the Si host, thus the P impurity effectively behaves like a hydrogen atom embedded in the Si lattice, with the difference being that the mass of the P nucleus is so much greater than the mass of the proton that it is assumed to be infinite. Additionally, the Coulomb attraction between the extra valence electron and the P nucleus is much weaker than the Coulomb attraction in the hydrogen atom, due to the screening by the large number of valence electrons in Si, so that the extra valence electron is only loosely bound to the P atom. This loosely bound electron can be easily ionized by thermal or electrical excitations, and as a result, the P atom 'donates' an electron to the Si conduction band. This is the

reason why P in Si is referred to as a donor impurity. [43–45]

An exact calculation of the Coulomb attraction between the loosely bound donor electron and the P donor ion is very difficult since the many-body interactions of the electrons in the donor atom with the valence electrons in the Si host need to be considered. This problem can be circumvented by assuming that the positive charge on the donor ion is screened by the dielectric constant of the host crystal. Using this approximation, the Coulomb potential of the donor can be expressed as:

$$V_S = +\frac{e}{\varepsilon_r r} \tag{2.1}$$

where ε_r is the dielectric constant of the host crystal. If the donor electron is assumed to be not too localized near the donor ion, then the static (i.e., zero frequency) dielectric constant can be used as ε_r in Equation 2.1. Since the donor electron is moving inside a semiconductor crystal, its motion is affected not only by the Coulomb potential of the donor, but also by the crystal potential, so its Schrödinger equation is given by:

$$(H_0 + U)\Psi(\mathbf{r}) = E\Psi(\mathbf{r}) \tag{2.2}$$

where $\Psi(\mathbf{r})$ is the donor electron wave function, H_0 is the one-electron Hamiltonian of the perfect crystal, and U is the potential energy of the donor electron in the screened Coulomb potential V_S, which is given by:

$$U = -eV_S \tag{2.3}$$

One way to solve the Schrödinger equation is to expand $\Psi(\mathbf{r})$ in terms of the Bloch functions of the perfect crystal, as they form a complete orthonormal set, but this approach requires extensive numerical calculations. Since the impurity breaks the translational symmetry of the crystal, the Bloch theorem cannot be used to simplify the problem. [43]

The most common approach to solving the Schrödinger equation is to use the 'effective mass approximation', which utilizes known electronic band structure parameters, such as the effective masses for the perfect crystal. Using this approach, the donor electron wave function, $\Psi(\mathbf{r})$, can be expressed in the form:

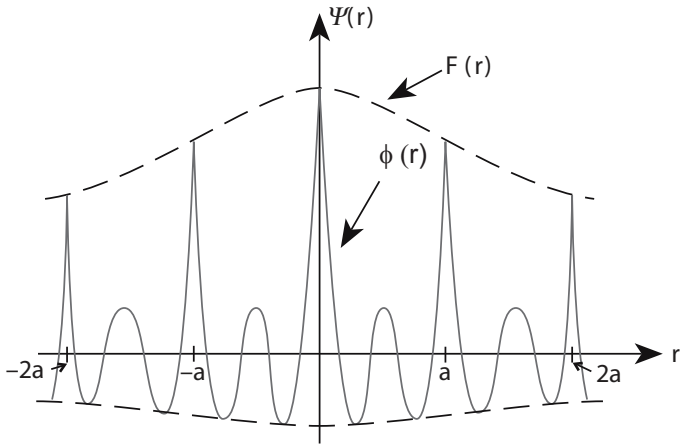

Figure 2.4: Schematic diagram of the donor electron wave function in real space. $\phi(\mathbf{r})$ is the Block function part and $F(\mathbf{r})$ is the slowly varying envelope function. a is the distance between lattice sites. [43]

$$\Psi(\mathbf{r}) = \sum_{j=1}^{N} \alpha_j F_j(\mathbf{r}) \phi_j(\mathbf{r}) \tag{2.4}$$

where N is the number of equivalent conduction band minima (equal to six for Si), α_j are numerical coefficients, $\phi_j(\mathbf{r})$ is the Bloch function at the jth minimum, and $F_j(\mathbf{r})$ are slowly varying envelope functions. The Bloch functions vary rapidly within each unit cell and are modulated by the slowly varying function $F_j(\mathbf{r})$ as a consequence of the weak Coulomb interaction between the donor electron and the donor ion. A schematic diagram of the donor electron wave function in real space is shown in FIG. 2.4. [44, 45]

If the lowest conduction band of the semiconductor crystal is assumed to be isotropic, nondegenerate, and parabolic, with the band minimum (E_c) located at the Brillouin zone centre, then Equation 2.2 will be of the form:

$$\left(-\frac{\hbar^2}{2m^*} \nabla^2 + U \right) F(\mathbf{r}) = (E - E_c) F(\mathbf{r}) \tag{2.5}$$

which is equivalent to the Schrödinger equation for a particle with effective mass m^* moving in a potential U, so that the motion of the donor electron is equivalent to that of the electron in the hydrogen atom. The net effect of the crystal potential

on the donor electron is that it changes the mass of the electron from its value in free space to the effective mass m^*. Equation 2.5 allows the envelope function $F(\mathbf{r})$ to be calculated, but this function must still be multiplied by the Bloch function to obtain the donor electron wave function $\Psi(\mathbf{r})$. It should be noted that Si does not satisfy the assumptions used here since its conduction band minima are degenerate and do not occur at the zone centre; however, these assumptions are valid in many semiconductors with the zinc-blende structure. A more detailed analysis of shallow impurities in silicon using the effective mass approximation can be found in the review article by Kohn [44].

Discrete and continuous eigenvalues similar to those for the hydrogen atom are obtained from solving Equation 2.5, with the continuum states being the delocalized conducting states. In the limit that U approaches zero in Equation 2.5, the donor electron energy E approaches the conduction band energy E_c, and the donor electron wave functions become equal to those of the nearest conduction band electrons. The discrete (or bound) states of the donor electron are classified by their principal quantum number n, angular momentum L, and spin. These states are denoted as $1s$, $2s$, $2p$, etc. in atomic physics, and similar notations are used to label the bound states of shallow impurities. A schematic diagram of some of the bound states of a shallow donor electron near a nondegenerate and parabolic conduction band is shown in FIG. 2.5. The relative position of the ground state ($1s$) with respect to the conduction band edge gives the donor ionization energy, which is typically of the order of 50 meV for shallow donors in silicon. The energies of the bound states of the donor electron are given by the Rydberg series:

$$E - E_c = -\frac{R}{n^2} = -\left(\frac{m^*}{m_0}\right)\left(\frac{1}{\varepsilon_r^2}\right)\left(\frac{e^4 m_0}{2\hbar^2}\frac{1}{n^2}\right) = -\left(\frac{m^*}{m_0}\right)\left(\frac{1}{\varepsilon_r^2}\right) R_H \qquad (2.6)$$

where R is the Rydberg constant for the donor electron and m_0 is the free electron mass. R_H is the Rydberg constant for the hydrogen atom, which has a value of 13.6 eV. The effective mass m^* of the donor electron reflects the curvature of the conduction band edge and characterizes the behaviour of electrons that are found in bound states near the band edge. In silicon, the effective mass is anisotropic, and as a result the effective mass tensor does not reduce to a scalar value m^*. The electron effective mass is characterized by a longitudinal and a transverse mass. [43–45]

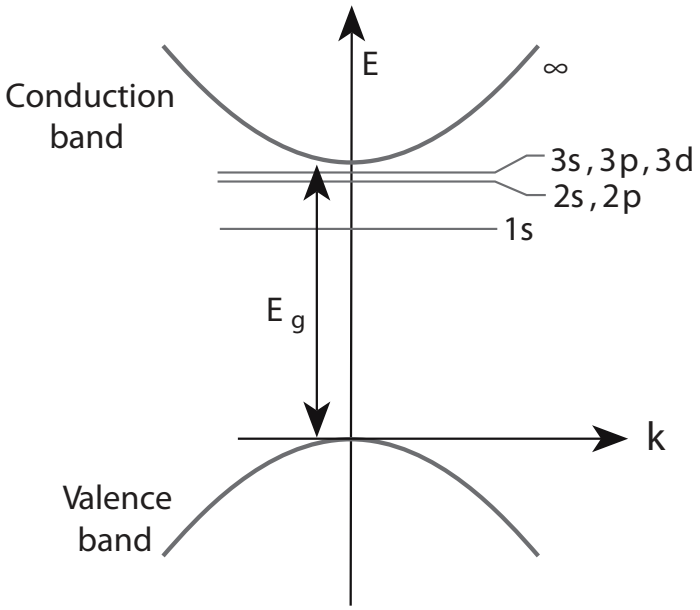

Figure 2.5: Schematic diagram of some of the bound states of a shallow donor electron near a nondegenerate and parabolic conduction band. E_g is the band gap. [43]

The extent of the donor electron wave function in real space is measured in terms of a donor Bohr radius a^*, which is given by:

$$a^* = \left(\frac{\varepsilon_r m_0}{m^*}\right)\left(\frac{\hbar^2}{m_0 e^2}\right) = \left(\frac{\varepsilon_r m_0}{m^*}\right) a_H^* \tag{2.7}$$

where a_H^* is the Bohr radius of the hydrogen atom, which has a value of 0.53 Å.

As mentioned earlier, the conduction band in silicon has six equivalent minima. When an impurity atom takes the place of a silicon atom in the lattice, the symmetry in the vicinity of the impurity is reduced from full cubic O_h symmetry to tetrahedral T_d symmetry, and as a result lifts the six-fold degeneracy of the conduction band minima. The resulting electron states, which involve different linear combinations of states near the six conduction band minima, are referred to as 'valley-orbit' states and can have different energies. The size of the 'valley-orbit' splitting of these states is dependent on the potential in the immediate vicinity of the impurity ion core, referred to as the central cell potential. In the absence of external perturbations, the $1s$ donor electron ground state decomposes into the irreducible representations Γ_1,

Γ_3, and Γ_5, of the T_d symmetry group (in Koster notation [46]). Γ_1 is a singlet state, while Γ_3 is two-fold degenerate, and Γ_5 is three-fold degenerate (not including spin).

The valence band maximum at the centre of the Brillouin zone ($\mathbf{k} = 0$) is, to a first approximation, six-fold degenerate. The hole states near the valence band maxima are classified by their angular momentum j_h and can have possible values of either j_h=3/2 or j_h=1/2. The j_h=3/2 states are split from the j_h=1/2 states by the spin-orbit interaction, and as a result, the six-fold degeneracy of the valence band maxima is lifted, giving a four-fold degenerate j_h=3/2 state belonging to the Γ_8 representation, at the top of the valence band, and a lower j_h=1/2 state belonging to the Γ_7 representation. [43, 44]

One of the main assumptions used when defining the screened Coulomb potential in Equation 2.1 was that the impurity was being screened by the dielectric constant of the host crystal. However, when the donor electron is in the immediate vicinity of the positively charged donor ion, the unscreened Coulomb attraction to the donor ion becomes dominant. Therefore, the screened Coulomb potential must be corrected with a short range potential, and the associated correction term is referred to as the 'central cell correction'. This correction is more important for the donor electron ground state than for the excited states, since the ground state has a smaller Bohr radius.

2.3 Donor bound excitons in silicon

An exciton is an electron-hole pair bound by the Coulomb interaction between the electron and the positively charged hole. This electron-hole pair is often referred to as a free exciton when it occurs in a semiconductor, and it is typically formed when a photon with above band gap energy excites an electron from the valence band to the conduction band, leaving behind a hole in the valence band. Typical lifetimes for excitons are in the range of 10^{-9}–10^{-3} s, after which the electron and hole recombine to emit a photon of characteristic energy. In indirect band gap semiconductors such as silicon, this process is assisted by a wave vector conserving phonon.

There are two types of excitons, which are classified according to the spatial extent of the exciton relative to the lattice spacing. The first type are known as Frenkel excitons and describe electron-hole pairs in which the electron and hole are tightly bound to each other. The radius of a Frenkel exciton is of the order of the lattice spacing. The second type of excitons are those consisting of a loosely bound electron-hole pair and have a radius much larger than the lattice spacing. These excitons, known as Wannier-Mott excitons, are most common in covalent crystals such as silicon. [43]

The energy of the free exciton E_{FE} is given by:

$$E_{FE} = E_g - E_b + E_{ke} \tag{2.8}$$

where E_g is the band gap, E_b is the energy of the 'bound' states of the free exciton, and E_{ke} is the kinetic energy associated with the centre-of-mass motion of the free exciton.

The electron and hole can be treated as particles with effective masses m_e^* and m_h^*, respectively, which are defined by the curvature of the local band extrema. The potential energy of the Coulomb attraction between the electron and hole can be written as:

$$U = -\frac{e^2}{4\pi\varepsilon_0\varepsilon_r r} \tag{2.9}$$

where ε_r is the dielectric constant of the host crystal and r is the particle separation.

In the effective mass approximation, the exciton centre-of-mass behaves like a free particle of mass $M = m_e^* + m_h^*$, and the exciton wave vector $\mathbf{K}$ is given by $\mathbf{k}_e + \mathbf{k}_h$, where $\mathbf{k}_e$ is the electron wave vector and $\mathbf{k}_h$ is the hole wave vector. If the lowest conduction band of the semiconductor crystal is assumed to be isotropic, nondegenerate, and parabolic, with the band minimum (E_c) located at the Brillouin zone centre, the kinetic energy E_{ke} of the exciton can be written in terms of M and $|\mathbf{K}|$ as:

$$E_{ke} = \frac{\hbar^2 |\mathbf{K}|^2}{2M} \tag{2.10}$$

Similar to the bound states of the donor electron which were discussed previously, the free exciton bound states form a hydrogen-like series below the band gap, with:

$$E_b = \frac{\mu e^4}{32\pi^2 \varepsilon_0^2 \varepsilon_r^2 \hbar^2 n^2} n = 1, 2, 3, ... \tag{2.11}$$

where $\mu = (\frac{1}{m_e^*} + \frac{1}{m_h^*})^{-1}$ is the reduced mass, and the value of E_b for n=1 is the exciton binding energy. Using typcial values of $\mu = 0.12 m_0$ (where m_0 is the electron mass in free space) [47] and ε_r (at 4.2 K) of 12.1 [42], the exciton binding energy in silicon is found to be 11 meV and the Bohr radius is 53 Å. This shows that the 'orbits' of the electron and hole about their centre of mass extend over many unit cells [48], and since the binding energies are small compared to k_BT at room temperature, excitonic processes must be studied in cryogenic environments.

A free exciton can be attracted to a neutral impurity via the van der Waals interaction to form a bound exciton. Since this attraction lowers the exciton energy, neutral impurities are very efficient at trapping free excitons. The existence of excitons bound to shallow neutral impurities was first proposed by Lampert [49] and later observed experimentally in silicon by Haynes [50] who noted the presence of sharp luminescence lines at energies lower than the free exciton energy. Shortly afterward, bound excitons were observed in many other semiconductors and photoluminescence (PL) spectroscopy of bound excitons was shown to be a very effective method for identifying different donor and acceptor impurities. This subsequently led to the development of a quantitative method for characterizing these impurities in silicon based on PL spectroscopy of bound excitons [51].

Since the kinetic energy contribution to the free exciton energy, which is responsible for the broadening of the free exciton luminescence line, is not present in the bound exciton energy, the PL spectroscopy of bound excitons produces sharp transition lines. The recombination of a bound exciton emits a photon of energy:

$$E_{BE} = E_g - E_b - E_L \tag{2.12}$$

where E_g is the band gap, E_b is the free exciton binding energy, and E_L is the localization energy, which is impurity specific.

Since silicon is an indirect band gap semiconductor, when impurity bound excitons are created or recombine, a wave vector conserving process is involved in addition to the absorption or emission of a photon. This typically involves the absorption or emission of a wave vector conserving phonon and results in the observed transitions being shifted in energy by an amount corresponding to the phonon energy. Another possibility is that the short range potential near the donor ion, known as the central cell potential, scatters the electron involved in the recombination to the Brillouin zone centre. This gives rise to what is referred to as the no-phonon transition. In the photoluminescence spectrum of the ground state of an impurity bound exciton in silicon, there is typically a no-phonon transition associated with the bound exciton as well as phonon-assisted transitions which occur at lower energy. Phonon-assisted transitions will generally be broader than no-phonon transitions due to the dispersion in the phonon spectrum, and to phonon lifetime broadening [52].

The donor bound exciton consists of two interacting electrons and one hole, as well as the fixed positive donor ion. In silicon, it is energetically favourable for the two electrons to occupy the lowest valley-orbit state Γ_1, forming a spin singlet. The hole wave function of the donor bound exciton belongs to the four-fold degenerate (j_h=3/2)-like Γ_8 state. Due to the valley-orbit splitting of the conduction band, the donor electron has a ground state with Γ_1 symmetry and two excited states with Γ_3 and Γ_5 symmetries. In the original shell model for bound excitons and bound multiexciton complexes proposed by Kirczenow [53, 54], the splitting between the Γ_3 and Γ_5 levels was considered to be negligible compared to their separations from the Γ_1 level, so the Γ_3 and Γ_5 levels can be approximated as being a single level – $\Gamma_{3,5}$. As a consequence, there are two possible states of the donor bound exciton:

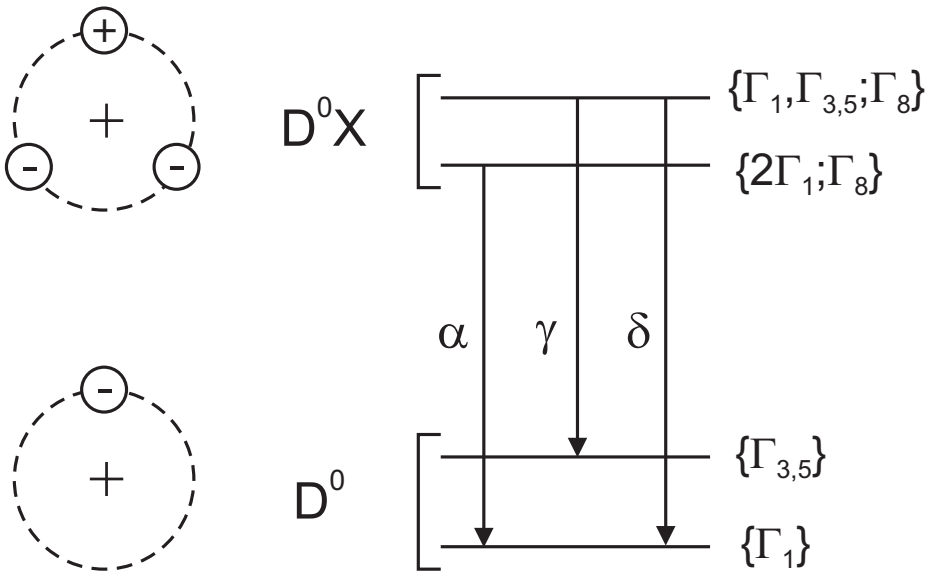

Figure 2.6: Energy level diagram showing the possible transitions between the donor (D^0) levels and the donor bound exciton (D^0X) levels.

one where both electrons are in the Γ_1 state and the hole is in a Γ_8 state, or the other, where one of the electrons is in the excited state $\Gamma_{3,5}$. In the first case, the donor bound exciton (D^0X) can be regarded as being in the ground state, which can be labelled by $\{2\Gamma_1;\Gamma_8\}$, and in the second, as being in an excited state labelled by $\{\Gamma_1,\Gamma_{3,5};\Gamma_8\}$. From the D^0X ground state, radiative electron-hole recombination leads only to the donor (D^0) ground state (Γ_1), while from the D^0X excited state, radiative electron-hole recombination can leave D^0 in either the Γ_1 ground state or a Γ_3 or Γ_5 excited state. An energy level diagram for the D^0X recombination process is shown in FIG. 2.6.

This model predicts three possible transitions labelled by α, γ, and δ. The α transition is the one corresponding to the D^0X ground state, where a donor bound exciton in the $\{2\Gamma_1;\Gamma_8\}$ state recombines, leaving behind a neutral donor in the Γ_1 state, while the γ and δ transitions involve recombination from the $\{\Gamma_1,\Gamma_{3,5};\Gamma_8\}$ excited state of the donor bound exciton. At pumped liquid helium temperatures ($< 4.2\,\mathrm{K}$), the D^0X excited state has negligible population, so only the α transition is observed.

In the present study, the α transition associated with the phosphorus donor bound

exciton is studied in highly enriched ^{28}Si using photoluminescence excitation (PLE) spectroscopy. In this method, the transition is studied in absorption rather than in emission, so unlike in PL spectroscopy, where above band gap photons are used to create free excitons which in turn form bound excitons, resonant excitation is used to create bound excitons in their ground state from the donor ground state. The resulting recombination and subsequent photon emission is then observed by detecting the corresponding transverse-optical phonon assisted transition.

It should be noted that shallow impurity bound excitons have very low radiative quantum efficiencies in indirect band gap semiconductors due to the dominance of nonradiative Auger recombination, in which the energy resulting from the recombination of the electron-hole pair is used to ionize the donor electron, leaving behind an ionized donor and an energetic free electron. For silicon, the luminescence quantum efficiency of the phosphorus donor bound exciton is $\sim 10^{-4}$ [55].

2.4 The phosphorus donor hyperfine interaction

A rather important perturbation to the phosphorus donor ground state energy, which has not yet been discussed, is the hyperfine interaction between the donor electron and the phosphorus nucleus. Only the ground state of the donor has a significant hyperfine interaction since this depends on the amplitude of the donor electron wavefunction near the donor nucleus. Additionally, a donor impurity such as bismuth, which has a larger binding energy than phosphorus due to its stronger central cell potential, also has a stronger hyperfine interaction in its donor ground state compared to phosphorus.

Phosphorus is monoisotopic with ^{31}P being the only stable isotope, and ^{31}P has a nuclear spin I_P of $\frac{1}{2}$, which can couple to the $S_e = \frac{1}{2}$ spin of the donor electron. This results in a three-fold degenerate state corresponding to total spin $F = 1$ and a singlet state corresponding to $F = 0$, with the energy separation between the $F = 1$ and $F = 0$ states being the hyperfine constant A, which has been previously measured by Feher [56] to be equal to 117.53 MHz for ^{31}P donors in silicon.

The degeneracy of the $F = 1$ triplet state can be lifted by the application of an external magnetic field. The donor ground state, under a static magnetic field $\mathbf{B} = B\hat{\mathbf{z}}$, can be described by the spin Hamiltonian:

$$\begin{aligned}\mathcal{H} &= \gamma_e \mathbf{S}_e \cdot \mathbf{B} - \gamma_P \mathbf{I}_P \cdot \mathbf{B} + A\mathbf{S}_e \cdot \mathbf{I}_P \\ &= \gamma_e S_z B - \gamma_P I_z B + A\left(S_z I_z + \frac{S_+ I_- + S_- I_+}{2}\right)\end{aligned} \tag{2.13}$$

where $\gamma_e(=g_e\mu_B)$ and $\gamma_P(=g_P\mu_n)$ are the gyromagnetic ratios of the donor electron and ^{31}P nucleus, respectively. The first and second terms in Equation 2.13 are the Zeeman energies of the donor electron and the ^{31}P nucleus, respectively, while the last term represents the contact hyperfine interaction between the donor electron spin and the ^{31}P nuclear spin. The eigenstates of the spin Hamiltonian can be given in the (m_e, m_I) representation, where m_e is the electron spin projection and m_I is the ^{31}P nuclear spin projection. There are two parallel spin states, $|\uparrow\Uparrow\rangle$ and $|\downarrow\Downarrow\rangle$, which are pure states, and two antiparallel spin states which tend to $|\uparrow\Downarrow\rangle$ and $|\downarrow\Uparrow\rangle$ at high field, but always have an admixture of the other component. In the notation used here, the first arrow indicates the electron spin projection and the second (double)

arrow indicates the ^{31}P nuclear spin projection, with an 'up' arrow denoting a value of $+\frac{1}{2}$ and a 'down' arrow denoting a value of $-\frac{1}{2}$.

The eigenvalues of the spin Hamiltonian give the energies of the four branches of the ^{31}P donor ground state:

$$\begin{aligned}
E_{|\uparrow\Uparrow\rangle}(B) &= +\left(\frac{\gamma_e - \gamma_P}{2}\right) B + \frac{A}{4} \\
E_{|\downarrow\Downarrow\rangle}(B) &= -\left(\frac{\gamma_e - \gamma_P}{2}\right) B + \frac{A}{4} \\
E_{|\uparrow\Downarrow\rangle}(B) &= +\sqrt{\left(\left(\frac{\gamma_e + \gamma_P}{2}\right) B\right)^2 + \left(\frac{A}{2}\right)^2} - \frac{A}{4} \\
E_{|\downarrow\Uparrow\rangle}(B) &= -\sqrt{\left(\left(\frac{\gamma_e + \gamma_P}{2}\right) B\right)^2 + \left(\frac{A}{2}\right)^2} - \frac{A}{4}
\end{aligned} \tag{2.14}$$

The energies of the two parallel spin states ($|\uparrow\Uparrow\rangle$ and $|\downarrow\Downarrow\rangle$) vary linearly with the magnetic field, while the energies of the two antiparallel spin states ($|\uparrow\Downarrow\rangle$ and $|\downarrow\Uparrow\rangle$) are non-linear functions of the field.

Chapter 3

Experimental Methods

The details of the ^{28}Si samples and the experimental apparatus used for photoluminescence excitation (PLE) spectroscopy in this study are discussed in this chapter. The final section of this chapter presents the alternative methods that were used to measure the ^{31}P donor bound exciton (D^0X) spectrum.

3.1 ^{28}Si Samples

Over the past several years, numerous samples of ^{28}Si have been made available for various experiments in this lab. The samples used for the experiments presented in this study are listed in TABLE 3.1, along with their associated isotopic purities, and phosphorus and boron concentrations. The impurity concentrations listed were determined from measurements of the bound exciton to free exciton intensity ratios in the photoluminescence (PL) spectra of the samples. This is a standard technique for the determination of shallow donor and acceptor concentrations in silicon [51, 57–61].

The n-type ^{28}Si c sample was provided by Prof. Eugene Haller of the University of California at Berkeley, while all other samples were provided by the group involved with the Avogadro Project [62], in which an accurate determination of the Avogadro constant will be made and will lead to a redefinition of the kilogram. The n-type ^{28}Si:P 3.3.1 to ^{28}Si:P 3.3.9 samples, which were specifically grown for the hyperpolarization experiments done in this lab, were produced from the same material used to grow the ^{28}Si a sample and intentionally doped with phosphorus by adding phos-

Table 3.1: List of ^{28}Si samples. The ^{28}Si isotopic enrichment, ^{31}P concentration, and B concentration are listed below for each of the samples used in this study. The ^{28}Si Avo, ^{28}Si a, and ^{28}Si b samples are p-type, while the ^{28}Si:P 3.3.1 to ^{28}Si:P 3.3.9 and ^{28}Si c samples are n-type. The asterisk ($*$) in the '% ^{28}Si' column denotes that the isotopic purity of the ^{28}Si:P 3.3.1 to ^{28}Si:P 3.3.9 may in fact be lower than the value listed below due to a possible unintentional reduction of the isotopic enrichment during the growth process.

Sample Name	% ^{28}Si	^{31}P Concentration (cm^{-3})	B Concentration (cm^{-3})
^{28}Si c	99.92	5×10^{14}	3×10^{13}
^{28}Si b	99.983	2×10^{13}	2×10^{14}
^{28}Si a	99.991	2×10^{12}	5×10^{13}
^{28}Si:P 3.3.1	99.991$*$	2×10^{14}	1×10^{14}
^{28}Si:P 3.3.6	99.991$*$	7×10^{14}	1×10^{14}
^{28}Si:P 3.3.7	99.991$*$	7×10^{14}	1×10^{14}
^{28}Si:P 3.3.9	99.991$*$	1×10^{15}	1×10^{14}
^{28}Si Avo	99.995	5×10^{11}	1×10^{13}

phine gas to the growth chamber. The crystal was delivered as a single boule and was later cut into nine 1.5 mm thick discs. The ^{28}Si Avo, ^{28}Si a, and ^{28}Si b samples are p-type, with a higher concentration of boron than phosphorus. The ^{28}Si Avo sample (99.995% ^{28}Si) is currently the most isotopically and chemically pure ^{28}Si available.

The samples listed in TABLE 3.1 came from single crystal boules grown along the [001] direction, and were cut into discs with (001) faces, with the exception of ^{28}Si a, which is a 1.5 cm by 3 cm rectangle with (001) faces, and the ^{28}Si Avo sample, which is a quarter disc. The discs are $\sim$1 cm in diameter and 1 to 1.5 mm thick. Before performing the experiments, the samples were chemically etched in a 10/1 HNO_3/HF solution to remove any damage resulting from the saw cuts and any oxide on the surface.

All ^{28}Si samples were produced from isotopically purified silane gas which was used to grow high purity polysilicon. The polysilicon was converted to single crystal silicon using the float zone (FZ) method, which is based on the zone-melting principle [63]. A polysilicon rod is mounted inside a growth chamber which is under vacuum or purged with an inert gas. A radio frequency (RF) heating coil melts a narrow region of the polysilicon rod, establishing a liquid molten zone. As the molten zone is moved along the polysilicon rod, the molten silicon solidifies into a single crystal. To start the growth, the ^{28}Si seed crystal at the bottom of the growth chamber is moved up to make contact with the molten silicon, and a necking process is carried out to establish dislocation-free growth before the boule is allowed to increase in diameter. The shape of the molten zone and the diameter of the boule are adjusted by changing the RF power of the coil and the travel speed, and are monitored by infrared sensors. [64] The crystal orientation of the boule is the same as that of the seed crystal. The advantage of the FZ method over the Czochralski method, which is commonly used in the electronics industry for growing large silicon single crystals (from which large diameter wafers are obtained), is that in the FZ method, the absence of a container used to hold the polysilicon melt results in single crystals of much higher chemical purity. [63] The lower concentrations of carbon and oxygen are especially important in the optical spectroscopy of silicon, as high concentrations of these impurities have been shown [65] to contribute to severely broadened optical transitions.

3.2 The PLE apparatus

The basic PLE apparatus used in this study is shown in FIG. 3.1. It consists of a distributed feedback Yb-doped fibre laser that is fed into an Yb-doped fibre amplifier and is locked and scanned with respect to a stabilized reference cavity, providing a long-term frequency stability of one part in 10^8, and sub-MHz frequency resolution. For the hyperpolarization experiments, a second Yb-doped fibre laser is used and is locked and scanned with respect to the same reference cavity. The amplified beam is mechanically chopped to allow for lock-in detection of the signal, and focussed (using a cylindrical lens) onto the edge of the sample, which is loosely mounted (to avoid strain) in a reflecting cavity to optimize the weak luminescence signals, and immersed in superfluid He at a temperature of 1.4 K. A $\frac{3}{4}$ m double monochromator is used to separate the transverse optical (TO) phonon-assisted luminescence signal from the scattered excitation radiation. The signal is then detected using a liquid-nitrogen-cooled germanium photodetector, which is very sensitive in the energy region of bound exciton transitions in silicon.

3.2.1 Excitation sources

Two tunable single-frequency Yb-doped fibre lasers, both manufactured by Koheras, were used for the present study. The one used as the PLE probe laser has a tunable range that spans both the no-phonon ^{31}P and B bound exciton transitions. The fibre temperature over which it operates is 20°C to 50°C, with a corresponding wavelength range of 1078.118 nm to 1078.795 nm. The laser used as the PLE pump spans only the no-phonon ^{31}P D^0X spectrum and has a wavelength range of 1077.3641 nm to 1078.3842 nm, corresponding to a fibre temperature range of 10°C to 50°C.

The PLE probe laser is an original equipment manufacturer part, which requires an external current supply (providing ∼200 mA) to drive it and requires a connection to a temperature controller to tune the wavelength by varying the fibre temperature. The PLE pump laser on the other hand, is a turn-key laser system with a built-in temperature controller, a piezoelectric driver for fine wavelength tuning, and a fibre optic output to connect to a wavemeter.

In the experimental setup, the output from the PLE probe laser is split using a

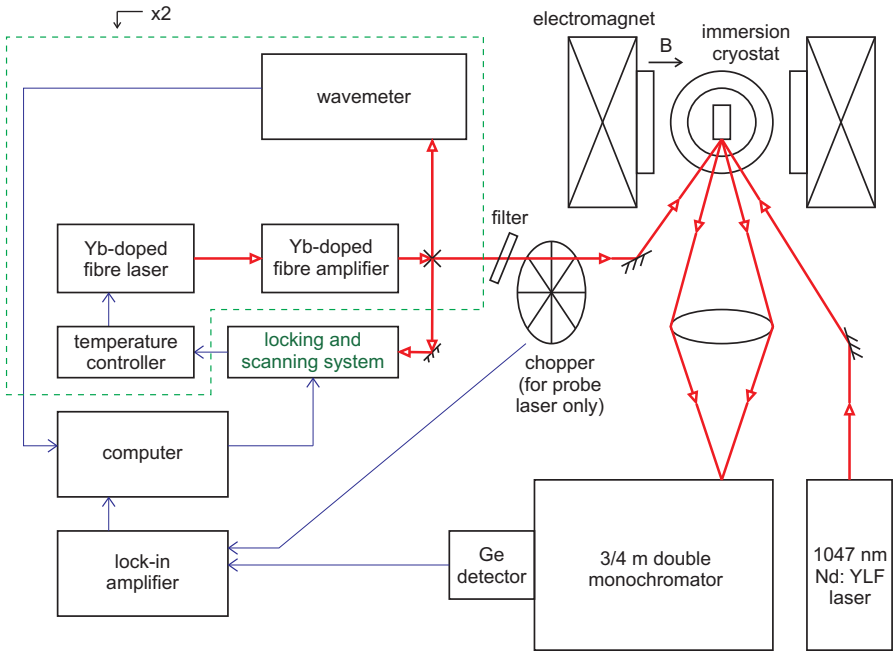

Figure 3.1: The basic PLE apparatus used for all experiments in this study.

50/50 fibre coupler, with 50% of the signal going to the input of an Yb-doped fibre amplifier (manufactured by Keopsys) and the other 50% being further split using a second 50/50 fibre coupler so that each output provides 25% of the original signal. One output goes to a wavemeter (manufactured by Burleigh) for monitoring the wavelength of the laser, while the other output goes to the reference cavity in the locking and scanning system. A schematic diagram of the PLE probe laser system is shown in FIG. 3.2.

The output from the PLE pump laser is split using a 90/10 fibre coupler, with 90% of the signal going to the input of an Yb-doped fibre amplifier (manufactured by IPG Photonics) and the other 10% going to the reference cavity in the locking and scanning system, as illustrated in FIG. 3.2. A wavemeter (manufactured by Bristol) is connected to the PLE probe laser system to monitor the wavelength of its output.

It should be noted that the primary source of background in the Yb-doped lasers is due to the spontaneous emissions produced by the Yb-doped fibre amplifiers. Most of this is removed using a 1080 nm band pass filter before the excitation reaches the

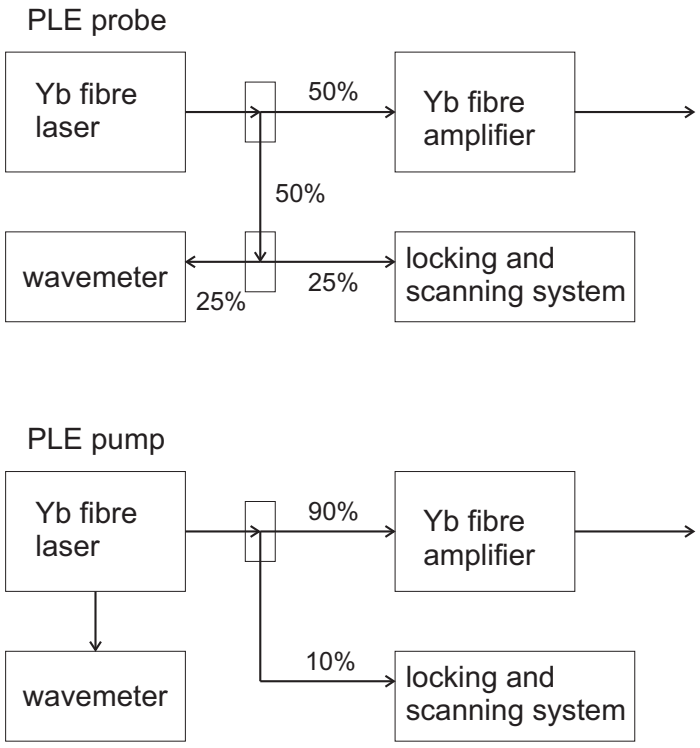

Figure 3.2: Schematic diagram showing the PLE pump and probe systems. The output from the PLE probe laser is split off using fibre couplers to send the beam to a fibre amplifier, a wavemeter, and to the locking and scanning system. The PLE pump laser goes to a fibre amplifier and to the locking and scanning system.

sample. This filter, however, also reduces the intensity of the resonant laser signal, by approximately a factor of two.

In addition to the two tunable Yb-doped fibre lasers, a 1047 nm Nd:YLF laser (manufactured by CrystaLaser) was used in the PLE apparatus. The above band gap excitation provided by this laser was needed for photoneutralization of ionized ^{31}P in the p-type ^{28}Si samples.

3.2.2 Locking and scanning system

At the heart of the locking and scanning system used in the PLE apparatus is a temperature stabilized reference cavity based on a 3 m long quartz cylindrical tube. At one end of the tube, through which the beams enter, is a window with a 4% reflecting concave inner surface, and at the other end is a mirror with a ∼100% reflecting concave surface. These are epoxied to the quartz tube at both ends and the inside of the tube is filled with N_2. A heating coil is wound around the quartz tube and a layer of insulating foam surrounds the tube and coil, which all sits inside a cylindrical copper tube.

Quartz has a low thermal expansion coefficient, but has a moderate thermal conductivity (1.4 W/(m·K)), so as a result, the length of the quartz tube is still fairly susceptible to change with varying temperature. In order to keep the quartz tube at a constant length, it is kept at a constant temperature using the heating coil. Whenever there is a slight change in the ambient temperature, feedback must somehow be provided to the coil's power supply to adjust its output and compensate for the change. This is done by using the 3 m long cavity to generate an interference pattern from a frequency stabilized helium-neon laser. The incoming beam is directed through the transmitting end of the cavity so that the direct reflection from the window (without entering the cavity) can be combined with the outgoing beam that has gone through three reflections inside the cavity and has acquired a path length difference of four times the length of the cavity, as shown in FIG. 3.3 for the Yb laser beam. The interference of these two beams results in a pattern of alternating bright and dark fringes. This pattern is projected onto a split photodiode with the two halves being straddled by a bright fringe and receiving the same amount of light. This ensures

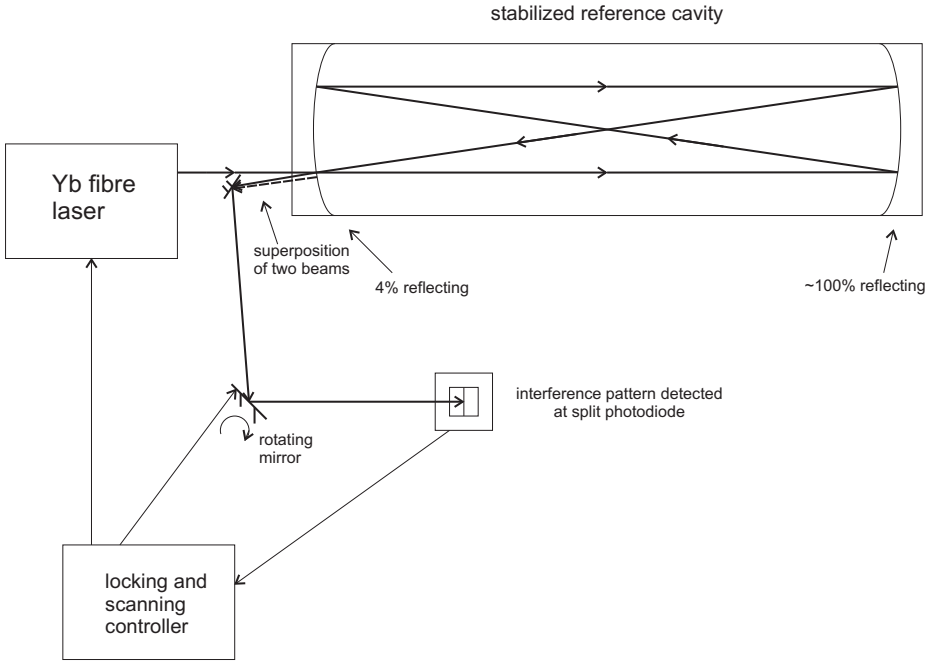

Figure 3.3: A schematic diagram of the system used to lock and scan the PLE lasers. This system is based around a 3 m long stabilized reference cavity.

that the difference signal of the split photodiode is zero when the reference cavity is stable. This signal is fed back to the heating coil power supply. When there is a slight change in the ambient temperature, the length of the cavity changes slightly and the interference pattern at the split photodiode drifts, which would make the difference signal either go positive or negative. The feedback circuit of the heating coil power supply receives this signal and adjusts the output to re-stabilize the length of the cavity and drive the difference signal back to zero. The use of a laser that is frequency stabilized is essential, as it produces a stable interference pattern when the quartz tube is at constant length.

With the reference cavity stabilized, the Yb-fibre lasers which provide the PLE pump and probe beams can be frequency locked using the same approach. For each laser, the direct reflection of the incoming beam off the window (without entering the cavity) is combined with the outgoing beam that has gone through three reflections inside the cavity to produce an interference pattern. A bright fringe is centered on a split photodiode so that the difference signal is zero. This signal is fed to a controller

circuit that sends feedback to the fibre laser. For both Yb lasers, slow feedback spanning the tuning range was achieved by temperature control, while fast feedback over a narrower range was achieved by modulating the pump laser power for the probe laser, and a piezoelectric tuner for the pump laser. A drift in the laser frequency will result in a shift of the interference pattern on the split photodiode and produce either a positive or negative difference signal depending on the direction of the frequency drift. The controller circuit takes this signal and adjusts the fibre temperature to send the laser back to its original frequency, at the same time driving the difference signal of the split photodiode back to zero. A schematic diagram of the locking and scanning system is shown in FIG. 3.3.

In order to scan the frequency of the laser using this system, there needs to be a method of shifting the interference pattern in a controlled manner. This was achieved with the use of a galvanometer-driven rotating mirror to reflect the interference pattern onto the split photodiode. The galvanometer was driven by a 256 step up/down counter connected to a digital-to-analog converter. Rotating the mirror by one step causes a small shift of the interference pattern on the split photodiode, resulting in a positive or negative difference signal, depending on the direction of rotation. In order to counteract this shift and drive the difference signal back to zero, the controller circuit adjusts the frequency of the laser. This technique allows the laser frequency to be changed in a controllable way. The full range of the mirror movement consists of 256 steps, and the step size is calibrated such that exactly one fringe of the reference cavity (or one free spectral range) is traversed in 256 steps. This ensures that whenever the mirror has reached its limit in one direction, it can swing all the way back to its starting position and continue scanning the laser frequency in the same direction without any uncontrolled jumps. The mirror swings back to its starting position faster than the controller's feedback circuit can realize it has moved, thus locking onto the next fringe.

The free spectral range can be determined by considering the phase difference between the two interfering beams. If $\mathbf{E}_1$ describes the beam that does not enter the cavity and $\mathbf{E}_2$ describes the beam that acquires a path length difference of four times the cavity length:

$$\mathbf{E}_1 = \mathbf{A}_1 e^{\mathbf{k}\cdot\mathbf{x}-\omega t} \tag{3.1}$$

$$\mathbf{E}_2 = \mathbf{A}_2 e^{\mathbf{k}\cdot\mathbf{x}-\omega(t+\tau)} \tag{3.2}$$

where $\omega\tau$ is the acquired phase difference and $A_1 \approx A_2$, then the condition for constructive interference is given by:

$$\begin{aligned} \omega\tau &= 2m\pi \\ \Rightarrow f\tau &= m \\ \Rightarrow f &= m\frac{c}{OPD} \end{aligned} \tag{3.3}$$

where m is an integer and $OPD \approx 12\,\text{m}$ is the optical path difference, so that the free spectral range is FSR $= \frac{c}{OPD} \approx 25\,\text{MHz}$, or $\approx 100\,\text{neV}$. The step size of $\frac{1}{256}$ of this value, or $\approx 0.4\,\text{neV}$, provides a measure of the maximum possible resolution for this system.

3.2.3 Cryostat, magnet, and monochromator

The cryostat used in the PLE apparatus is a helium-immersion dewar, in which the sample is directly submerged in the liquid helium bath. The dewar has quartz windows on three sides of the tail. The sample is mounted loosely (to avoid strain) inside a slot in a brass holder with gold mirrors on two sides to form a reflecting cavity and with a sliver of glass placed on the front side to keep it from falling out. The holder is suspended by a rod at a height inside the cryostat that places the sample at the centre of the window.

An electromagnet with 4-inch diameter pole faces capable of generating magnetic fields of up to $\sim$2000 Gauss is used in the PLE apparatus. The tail of the cryostat is placed between the pole faces and the sample is oriented so that the field is applied parallel to the [001] axis of the sample. The spectra are collected in Voigt geometry, with the 1x10 mm pump and probe beams illuminating the same edge of the sample from which the PL is collected. A Gauss probe, placed between the cryostat tail and one of the pole faces, is used to measure the magnetic field.

A $\frac{3}{4}$ m double monochromator is used to separate the TO phonon-assisted luminescence signal from the scattered excitation radiation. The ^{31}P D^0X TO wave vector conserving phonon replica is well-separated in energy from the no-phonon ^{31}P D^0X transition ($\sim$58 meV lower in energy), as shown in FIG. 3.4, which is a plot of the ^{31}P D^0X PL spectrum for an n-type sample of ^{28}Si. The monochromator is tuned to the TO region of the ^{31}P D^0X spectrum by rotating the diffraction grating to select the energy band centered at $\sim$1140 nm. The spectral resolution of $\sim$2 meV is sufficient to reject both the scattered laser excitation as well as the zone centre optical phonon Raman scattering, but is much wider than the ^{31}P D^0X spectrum, so the detection is not selective. Rejection of the scattered laser excitation could in the future be achieved using custom filters, which might lead to better throughput and signal-to-noise ratio.

3.2.4 Data collection

Scanning of the PLE pump and probe lasers and recording of the PLE signal is performed using LABView software, which interfaces with the locking and scanning system and the lock-in amplifier. This provides a simplified process for automated collection of spectra and for changing of experimental parameters such as scan range, scan speed, and resolution. To record a PLE spectrum, the software first needs to communicate with the lasers and have them scan through the desired energy range. The lasers are scanned by two stepping motor controller modules interfaced by USB, which generate the up/down pulses to the counters that drive the galvanometers and which in turn drive the rotating mirrors (as previously described). This allows the computer to send one command containing the desired number of steps, scan rate, and scan direction, for any size of move of the laser energy. The resulting chopped luminescence signal collected by the germanium detector is measured by a GPIB controlled lock-in amplifier, which digitizes the signal for recording by the software.

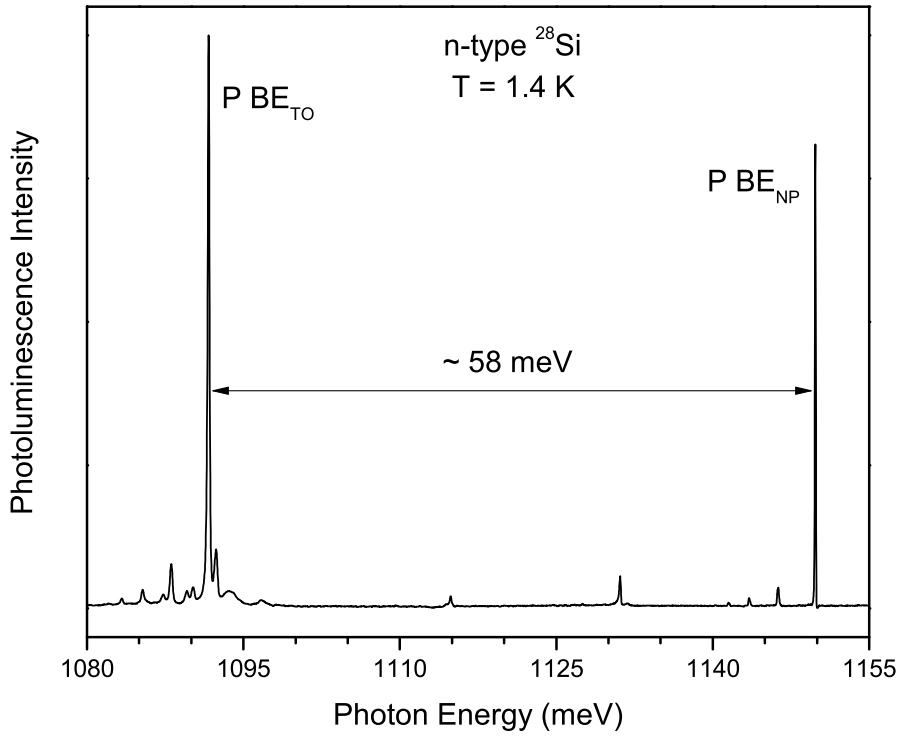

Figure 3.4: PL spectrum showing the no-phonon and TO phonon-assisted ^{31}P D^0X transitions for an n-type sample of ^{28}Si. The ^{31}P D^0X TO wave vector conserving phonon replica (P BE_{TO}) is ∼58 meV lower in energy compared to the no-phonon ^{31}P D^0X transition (P BE_{NP}).

3.3 Alternative methods of measuring the ^{31}P D^0X spectrum

3.3.1 Photoconductivity measurement of bound exciton spectra

Due to the dominance of nonradiative Auger recombination in indirect band gap semiconductors, shallow impurity bound excitons have very low radiative quantum efficiencies. For silicon, the luminescence quantum efficiency of ^{31}P bound excitons is $\sim 10^{-4}$ [55]. The near-unity efficiency of the Auger process presents an alternative method of measuring the D^0X spectrum, by detecting the free electrons released in Auger recombination. Simple electrical contacts were made to opposite ends of the sample by rubbing on a thin layer of In-Ga eutectic and using fine copper wires to connect an external 1.5 V bias source and a transimpedance current amplifier. A schematic of this setup is shown in FIG. 3.5. The apparatus used for this photoconductivity method is mostly unchanged from the PLE apparatus presented in the previous section, with the only difference being the removal of the double monochromator and Ge detector, as the output of the amplifier is taken directly to the lock-in amplifier.

The method for obtaining D^0X photoconductivity spectra was later improved by developing a contactless technique, in which a 180 kHz RF signal is capacitively coupled through the sample using two Cu foil discs, parallel to but not in contact with the two faces of the sample. The RF current coupled through the sample is amplified and measured with a phase sensitive detector. The main advantage of this capacitive method compared to the previous photocurrent method is that it removes the need for physical contacts, which tend to strain the sample and broaden the D^0X spectral lines.

In this contactless capacitive method, the sample can be viewed as a combination of a resistor R in parallel with a capacitor C. An equivalent circuit for the scheme is shown in FIG. 3.6. In order for there to be a change in current across the sample as the laser is tuned over a D^0X transition, the frequency of the RF signal must be chosen such that the resistance of R is approximately equal to the reactance of C. Since the values for R and C were not known a priori, the frequency of the RF signal

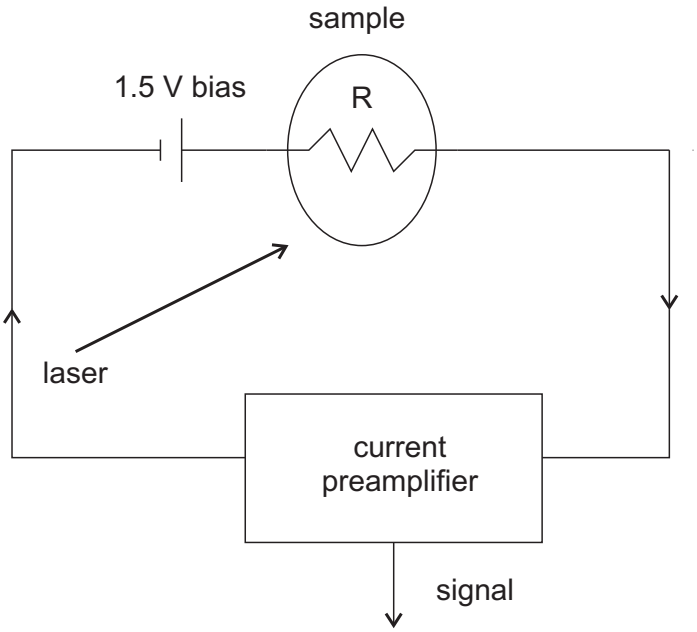

Figure 3.5: A schematic diagram of the photoconductivity method.

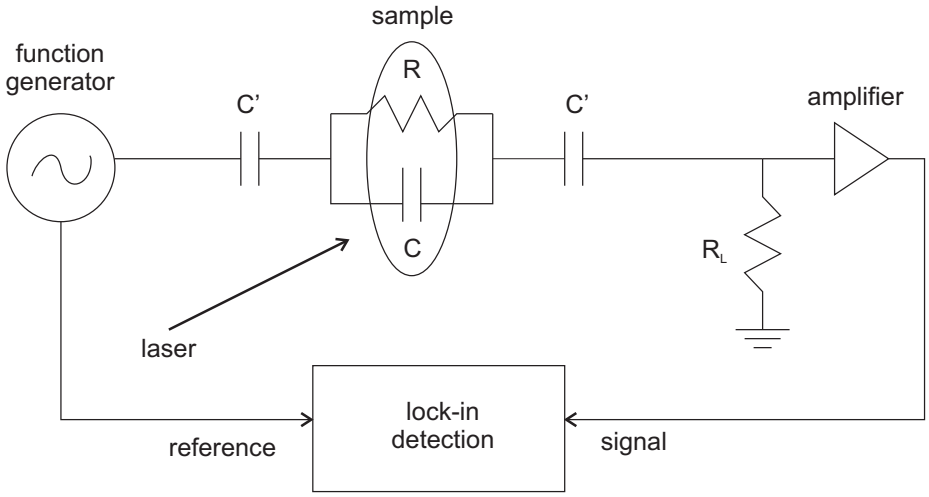

Figure 3.6: A schematic diagram of the contactless capacitive photoconductivity method.

was adjusted until there was an optimal change in current while scanning across a D^0X transition. If the frequency is set too high, then the reactance of C is too small compared to the resistance of R, and the signal shorts out through C, resulting in no change in current across the sample. If the frequency is set too low, then the reactance of C' is too large compared to the resistance of R, which results in too little current through C' and the capacitive coupling being broken. The load resistor R_L is chosen such that a noticeable change in signal occurs as the laser is tuned over a D^0X transition.

3.3.2 Laser absorption method

Another method of obtaining the ^{31}P D^0X spectrum is by measuring the transmission of the resonant laser through the sample. Since the absorbed laser signal is used to generate D^0X, which subsequently recombine either radiatively to give the D^0X spectrum or nonradiatively via the Auger process, the transmitted laser signal yields the inverse of the D^0X spectrum. A schematic of the laser absorption setup is shown in FIG. 3.7. For this type of experiment, a slightly modified sample holder with openings on both the front and back to allow the resonant laser through was used. Another opening on one side of the holder was required for side illumination of the sample by the 1047 nm photoneutralizing laser so that only the resonant laser is detected by the photodiode mounted behind the sample. Since the changes in the transmitted signal that are produced as the laser is scanned across the ^{31}P D^0X transition are very small, the noise due to the spontaneous emissions generated by the resonant fibre laser greatly lowers the signal-to-noise observed in the transmission spectrum. In order to remove this noise, a balanced detector was used. In addition to the photodiode mounted behind the sample to measure the transmitted signal, a second photodiode was placed near the front of the sample to detect one of the beams reflected by the front window of the cryostat so that the unabsorbed signal could be measured. An output signal proportional to the difference signal from the two photodiodes was then used to produce a transmission spectrum in which the noise due to the spontaneous emissions from the resonant laser is absent.

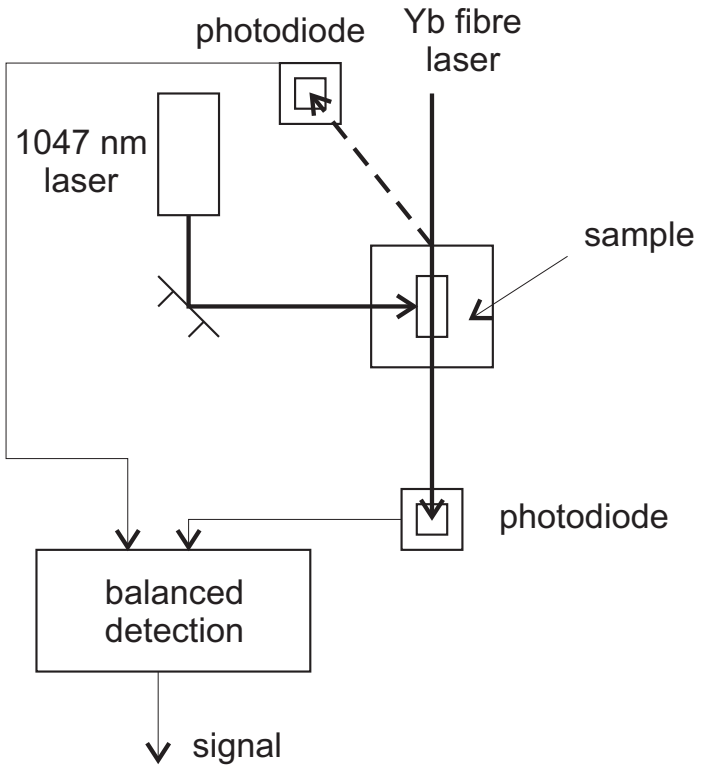

Figure 3.7: A schematic diagram of the laser absorption method.

Chapter 4

Experimental Results and Discussion

In this chapter, the photoluminescence excitation (PLE) spectroscopy of the ^{31}P donor bound exciton (D^0X) in ^{28}Si is presented, beginning with the zero magnetic field and low magnetic field spectra of the no-phonon ^{31}P D^0X transition. The ability to resolve the individual hyperfine components of the ^{31}P D^0X transition under an applied magnetic field led to the possibility of selective optical pumping into specific donor electron and nuclear spin states. While preliminary attempts at polarizing the spin states in a p-type sample yielded modest electron and nuclear polarizations of approximately 50% and 25%, respectively, the electron and nuclear polarizations achieved in a recently grown n-type ^{28}Si sample were 90% and 76%, respectively. The nuclear polarization dynamics of this process were captured and it was found that the polarization builds up in less than a second. In the final section of this chapter, a study of the spectral hole burning that occurs with optical pumping is presented, in which the homogeneous linewidth of the ^{31}P D^0X transition is determined.

4.1 ^{31}P bound exciton spectrum in ^{28}Si

In the shell model of bound exciton and bound multiexciton complex structure in Si [53, 54], the ^{31}P D^0X is expected to have a very simple unsplit ground state transition, as described previously in Section 2.3. The single line observed [23] for the no-phonon photoluminescence (PL) transition of the ^{31}P D^0X in ^{nat}Si and ^{28}Si seemed to validate this prediction, but a higher resolution PLE spectrum of the ^{31}P D^0X in ^{28}Si, as shown in FIG. 4.1 for a ^{28}Si sample with isotopic enrichment of 99.991%, reveals that the ^{31}P D^0X is more complicated than expected. The smaller splitting (indicated by the two small brackets), which is different depending on the ^{28}Si sample being studied, varies with temperature and the amount of above-gap excitation used to achieve photoneutralization. The ^{31}P D^0X transition line is further split by a larger splitting that remains constant between different ^{28}Si samples. This sample-independent splitting is approximately equal to 486 neV (or approximately 117 MHz in frequency units) and can be identified as the hyperfine splitting [56] of the ^{31}P neutral donor (D^0) ground state.

It should be noted that the addition of above-gap excitation, provided by a 1047 nm Nd:YLF laser, was required to produce the spectrum in FIG. 4.1. The above-gap excitation has the effect of photoneutralizing the donors, which in this p-type sample are ionizied due to compensation from the higher boron acceptor concentration. Electrons in the valence band are excited to the conduction band by the above-gap light to produce free electrons and free holes, which can in turn be captured by the ionized donors and ionized acceptors, respectively, thus forming neutral impurities.

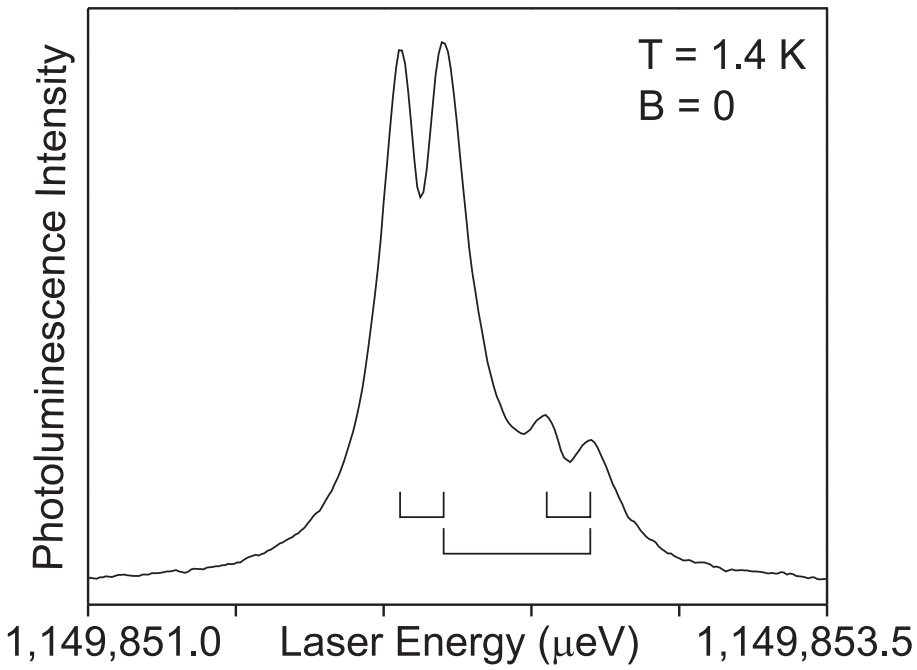

Figure 4.1: The PLE spectrum of the no-phonon ^{31}P D^0X transition for the p-type ^{28}Si a sample. The smaller sample-dependent splitting, indicated by the two small brackets, varies with excitation conditions, temperature, and sample purity, while the larger sample-independent splitting remains constant, and is equal to the zero field hyperfine splitting of the ^{31}P neutral donor ground state in Si.

4.1.1 ^{31}P bound exciton spectrum at zero magnetic field

The shape of the ^{31}P D^0X spectrum has a significant dependence on the amount of above-gap excitation used, as shown in FIG. 4.2, which shows a comparison of spectra for various above-gap excitation levels between 0 and 1000 mW for a p-type sample of ^{28}Si enriched to 99.992% (^{28}Si a). At the bottom of FIG. 4.2 is the spectrum produced with 1000 mW of above-gap excitation, in which both the small sample-dependent splitting and the sample-independent hyperfine splitting are resolved. As the excitation power is decreased to 300 mW, the ^{31}P D^0X spectrum becomes broader and the features on the high energy shoulder are barely resolvable, while at 100 mW they are not resolved at all. Below 100 mW of above-gap excitation power, the signal becomes weaker and the broadening becomes more severe, and essentially only a single broad feature with a low energy shoulder is resolved. The broadening of the ^{31}P D^0X spectrum at low above-gap excitation levels is likely due to random electric fields resulting from the presence of ionized donors and acceptors. At higher above-gap excitation levels, as more ionized donors and acceptors are neutralized, this effect is reduced and the features in the ^{31}P D^0X spectrum become better resolved.

A comparison of the ^{31}P D^0X spectra at four different temperatures between 2.0 K and 4.2 K for a p-type sample of ^{28}Si enriched to 99.983% (^{28}Si b) is shown in FIG. 4.3. These spectra were collected without the addition of above-gap excitation and this comparison reveals a thermally activated mechanism which can generate neutral donors without above-gap excitation. Compared to the spectrum at 4.2 K, the one at 2.0 K is approximately 16 times less intense. An activation energy for the mechanism responsible for this reduction in intensity with decreasing temperature can be determined by assuming that the intensity I of the ^{31}P D^0X spectrum has a dependence on temperature of the form:

$$I = Ce^{-E_a/k_BT} \tag{4.1}$$

where E_a is the activation energy and C is a constant.

Using the peak intensity of the largest feature in the ^{31}P D^0X spectrum, obtained from curve fitting, an Arrhenius plot was generated from the data, which was collected over the temperature range of 1.3 to 4.2 K, and is shown in FIG. 4.4. The data

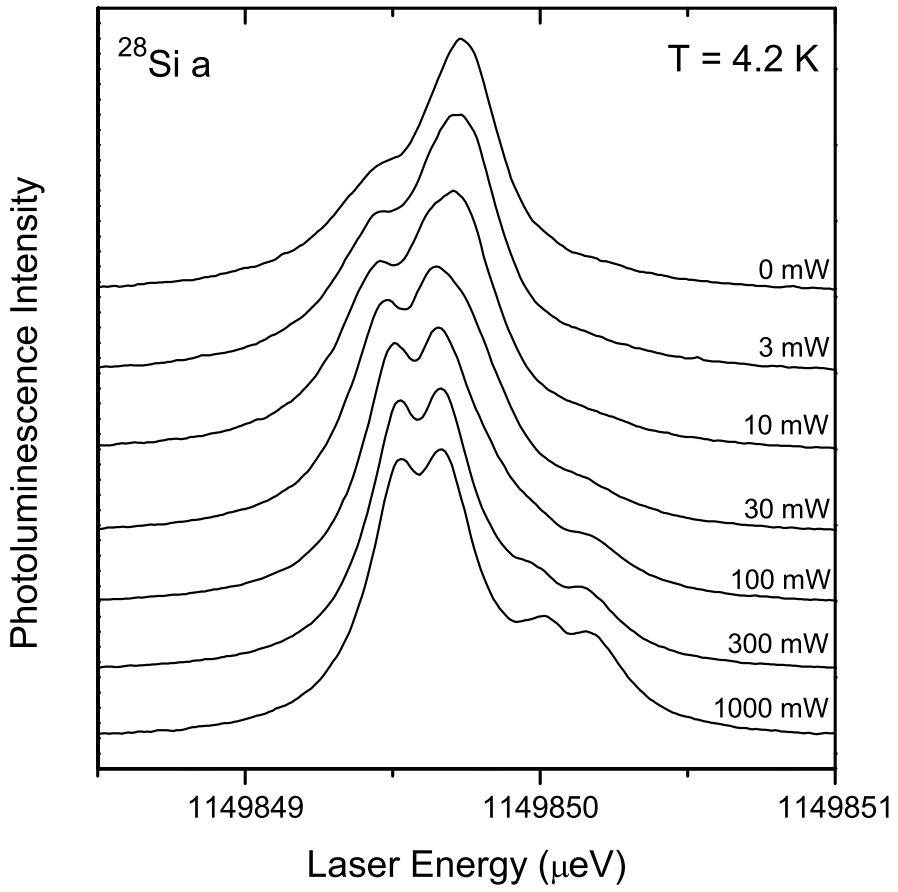

Figure 4.2: A comparison of the ^{31}P D^0X PLE spectra for a p-type sample of ^{28}Si enriched to 99.992% (^{28}Si a) at seven different levels of above-gap excitation ranging from 0 to 1000 mW. As the above-gap excitation power is reduced, the features become broader and not as well resolved.

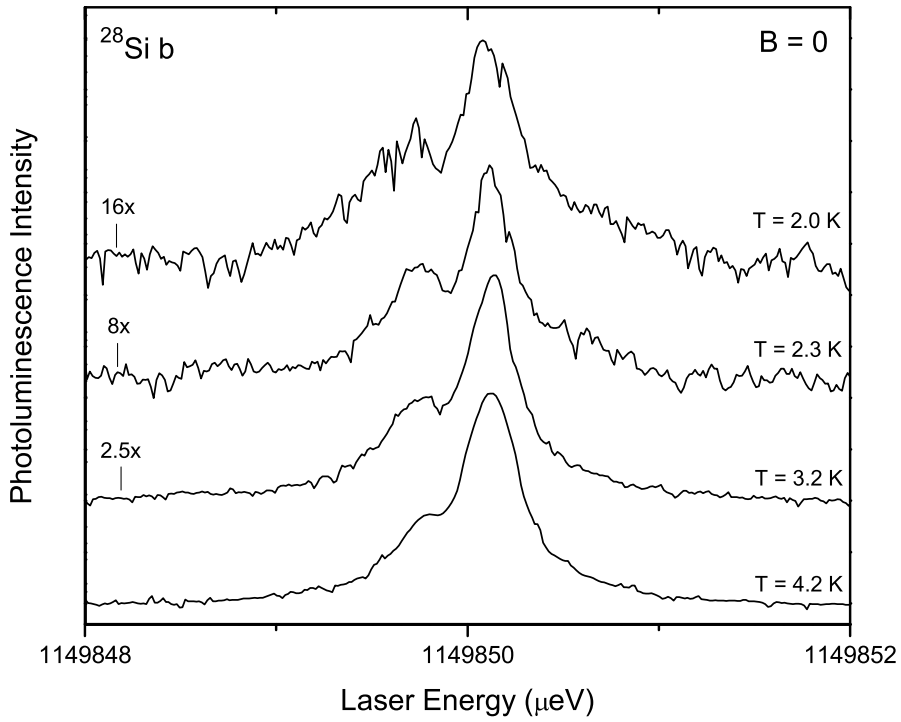

Figure 4.3: A comparison of the ^{31}P D^0X PLE spectra at sample temperatures of 4.2, 3.2, 2.3, and 2.0 K for a p-type sample of ^{28}Si enriched to 99.983% (^{28}Si b), in the absence of any above-gap light to photoneutralize D^0. The vertical scales of the 3.2, 2.3, and 2.0 K spectra have been expanded by 2.5, 8, and 16 times, respectively.

deviates from the overall linear trend only at the lowest temperature points. This is likely the result of significant variations in the actual temperature of the sample from the He bath temperature in the lowest temperature region due to poor thermal contact. Therefore, the three lowest temperature data points have been omitted from the curve fit, which yields a slope of -10.1 K. This corresponds to an activation energy of 0.9 meV. The only known energy value in this vicinity is the A^+ ionization energy for boron acceptors in silicon, which is 1.9 meV [66]. The ionization energies for neutral impurities in silicon are at least one order of magnitude larger.

Even though the excitation light is below-gap, low concentrations of free holes (h^+) and free electrons (e^-) can be generated via the processes $A^0 + h\nu \rightarrow A^- + h^+$ and $A^- + h\nu \rightarrow A^0 + e^-$. At low temperature, some of the free holes can bind to A^0 centres to form A^+ ions [67], and these A^+ ions will compete with ionized donors (D^+) in capturing these free electrons ($A^+ + e^- \rightarrow A^0X$). Thus the presence of A^+ ions might be responsible for the significant decrease in D^0X PLE intensity with decreasing temperature in p-type samples in the absence of above-gap illumination.

A comparison of the ^{31}P D^0X spectrum for four ^{28}Si samples with different ^{31}P concentrations ranging from $5 \times 10^{11}\,cm^{-3}$ to $1 \times 10^{15}\,cm^{-3}$ is shown in FIG. 4.5. The two p-type samples (^{28}Si Avo and ^{28}Si a) have the lowest ^{31}P concentrations, while the two n-type samples (^{28}Si:P 3.3.1 and ^{28}Si:P 3.3.9) have the highest. When comparing the bottom two spectra in FIG. 4.5, it is apparent that the smaller sample-dependent splitting is larger for the sample with higher ^{31}P concentration (^{28}Si a). This initial observation led to the belief that this splitting was due to interactions between ^{31}P donors and therefore dependent on ^{31}P concentration. However, when the newer n-type samples were obtained, the two samples with the lowest and highest ^{31}P concentrations were compared, and their respective ^{31}P D^0X spectra looked rather similar, as seen in the top two spectra of FIG. 4.5. The sample-dependent splitting that was seen in the two p-type samples are much larger in the n-type samples; in fact, it is comparable to the hyperfine splitting in the n-type samples, but there is virtually no difference in the size of the splitting when comparing the ^{28}Si:P 3.3.1 and ^{28}Si:P 3.3.9 samples, which have ^{31}P concentrations of $2 \times 10^{14}\,cm^{-3}$ and $1 \times 10^{15}\,cm^{-3}$, respectively. This observation suggests that the splitting may not be due to interactions between ^{31}P donors as initially believed, but that it is more likely

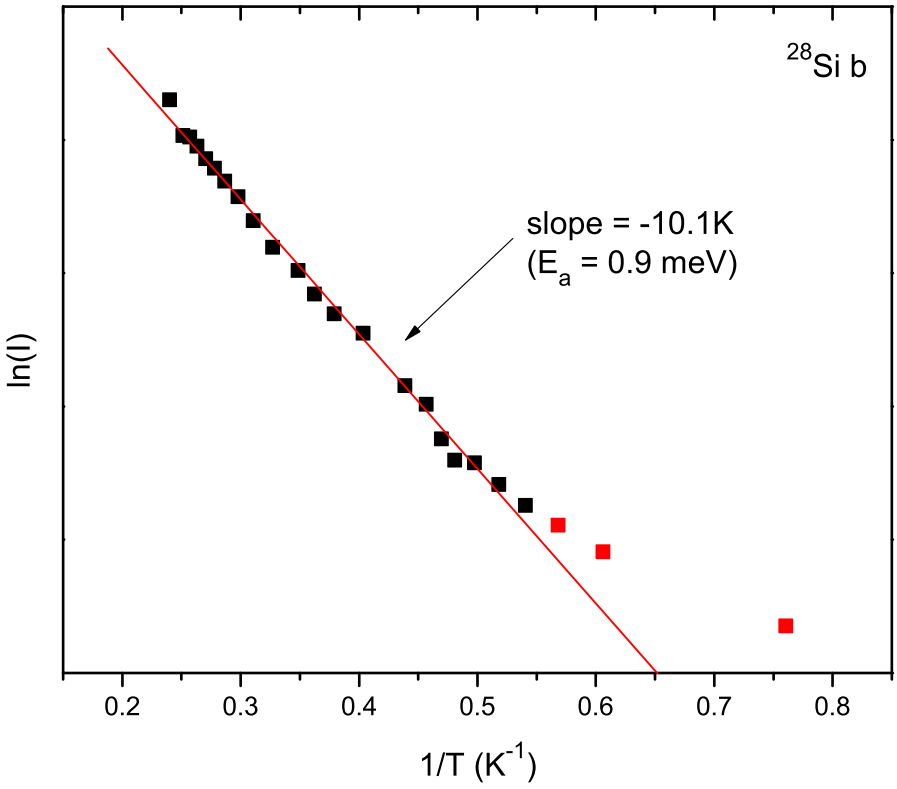

Figure 4.4: A plot of the natural log of the peak intensity ln(I) of the ^{31}P D^0X PLE spectrum versus 1/T yields a slope of -10.1 K, corresponding to an activation energy of 0.9 meV. The data displayed in the plot was collected from a p-type sample of ^{28}Si enriched to 99.983% (^{28}Si b), in the absence of any above-gap illumination. The data points for the three lowest temperature spectra were not used in the determination of the slope.

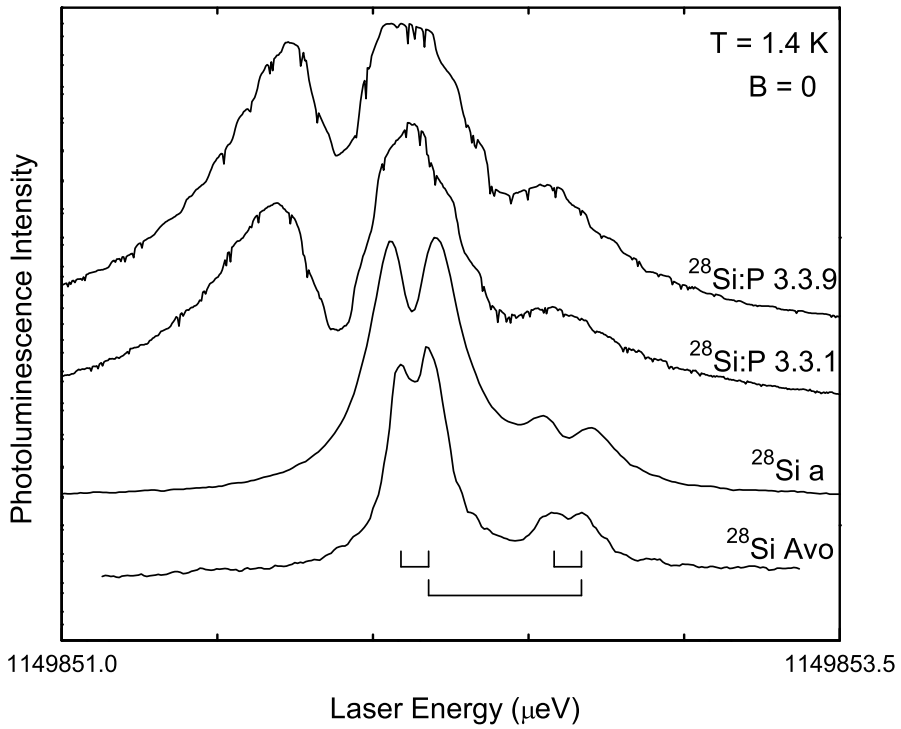

Figure 4.5: A comparison of the ^{31}P D^0X spectrum at zero field for four different ^{28}Si samples with ^{31}P concentrations ranging from $5 \times 10^{11}\,\mathrm{cm}^{-3}$ to $1 \times 10^{15}\,\mathrm{cm}^{-3}$. The bottom two spectra are for p-type samples, while the top two are for n-type samples. The sample-dependent splitting (indicated by the two small brackets), which is different for the two p-type samples, is essentially the same in the two n-type samples where it is much larger.

due to a random splitting of the degenerate light hole and heavy hole bands by the remaining inhomogeneous broadening, which could result from the small amounts of ^{29}Si and ^{30}Si present in the samples, or from other impurities such as carbon. [65] The application of a moderate magnetic field dominates over the zero field effects, and produces spectra for the different samples that differ only in the linewidth of the Zeeman and hyperfine components.

4.1.2 ^{31}P bound exciton spectrum at low to intermediate magnetic field

In the presence of a small applied magnetic field parallel to the [001] axis, the resulting spectrum of the ^{31}P D^0X transition becomes even more complex, revealing six sets of doublets, as shown in FIG. 4.6. This structure can be explained by the Zeeman level diagram shown in FIG. 4.7. The two electrons in the D^0X ground state form a spin singlet, so only the projection of the hole spin, m_h, affects the D^0X energy, which splits into four levels under a magnetic field. The D^0 ground state splits into two levels under a magnetic field as a result of the spin $\frac{1}{2}$ donor electron, thus there are six electric-dipole allowed $D^0 \rightarrow D^0X$ transitions. These six main transitions are further split by the donor hyperfine interaction into doublets, which at intermediate fields have a splitting of approximately one half of the zero field hyperfine splitting (the sum of the two donor hyperfine doublet splittings equals the zero field splitting). It should be noted that at the fields and temperatures used here, all of the splittings are much less than k_BT.

The 12 electric-dipole allowed $D^0 \rightarrow D^0X$ transitions are labeled 1 to 12 in order of increasing energy in FIG. 4.7. The D^0 hyperfine states consist of two parallel spin states $|\uparrow\Uparrow\rangle$ and $|\downarrow\Downarrow\rangle$ which are not coupled by the hyperfine interaction, and two anti-parallel states $|\uparrow\Downarrow\rangle$ and $|\downarrow\Uparrow\rangle$ which are somewhat mixed by the hyperfine interaction. The $D^0 \rightarrow D^0X$ transitions labelled π, corresponding to $\Delta m = 0$, occur when the polarization of the resonant excitation light is parallel to the magnetic field direction, while the transitions labelled σ, corresponding to $\Delta m = \pm 1$, occur when the polarization is perpendicular to the field.

The electron and hole g factors can be determined from the ^{31}P D^0X spectrum by measuring the energy difference between transition lines that give the corresponding electron and hole Zeeman splittings according to the energy level diagram in FIG. 4.7. From FIG. 4.6, the electron and hole g factors are found to be $g_e = 1.97$, $g_{h(1/2)} = 0.83$, and $g_{h(3/2)} = 1.3$, which are in good agreement with earlier studies [68] of the phosphorus bound exciton at much higher fields, and the sum of the x and y hyperfine splittings agrees with the 486 neV (117.53 MHz) phosphorus donor hyperfine splitting determined by EPR [56].

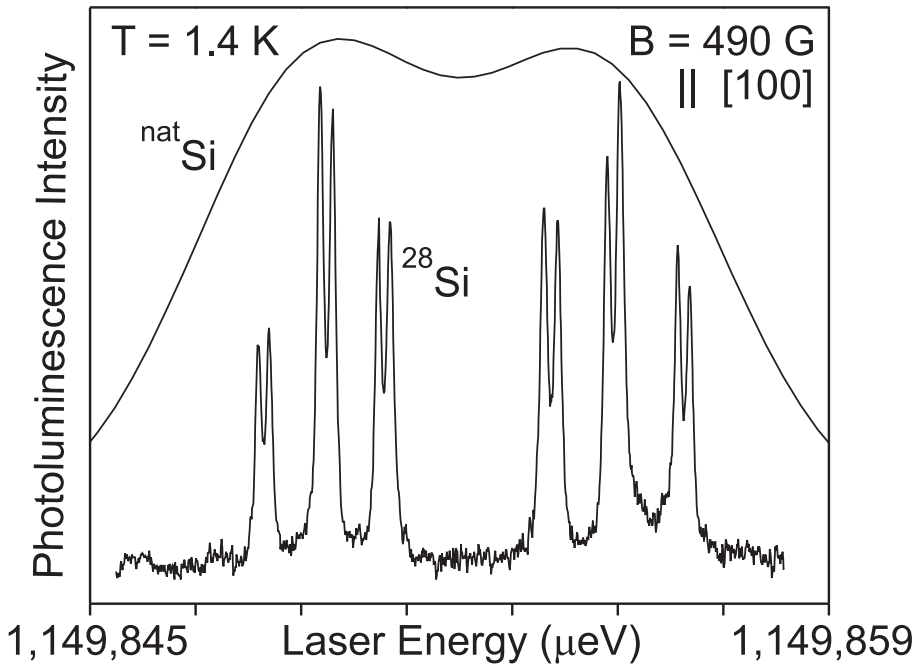

Figure 4.6: The PLE spectrum of the no-phonon ^{31}P $D^0 \rightarrow D^0X$ transitions for the ^{28}Si a sample with an applied magnetic field of 490 G parallel to the [001] axis. For comparison, a simulated spectrum of the ^{31}P $D^0 \rightarrow D^0X$ transitions is shown for ^{nat}Si at the same magnetic field. This was generated by convolving 12 transition lines positioned at the energies of the 12 hyperfine components in ^{28}Si, with each line having the 5 μeV FWHM of the ^{31}P D^0X transition in ^{nat}Si.

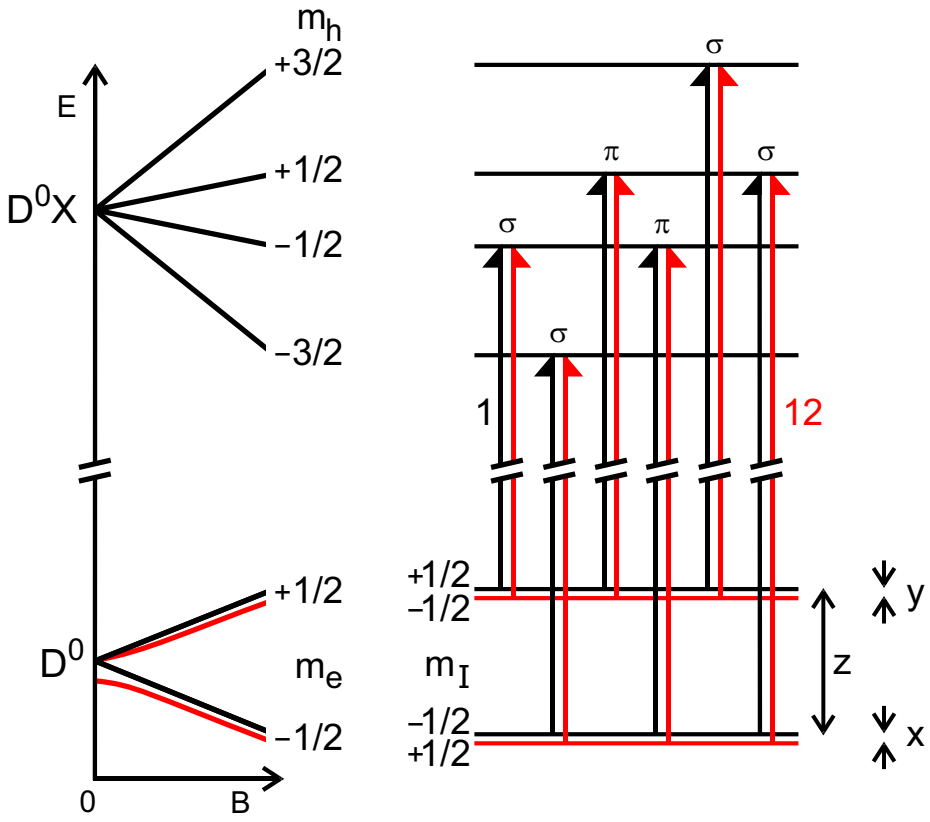

Figure 4.7: An energy level diagram showing the origin of the ^{31}P $D^0 \rightarrow D^0X$ transitions seen in FIG. 4.6. D^0 is the neutral donor ground state, which at zero field is split into a singlet and a triplet by the ∼486 neV ^{31}P hyperfine splitting. When a magnetic field is applied, the Zeeman splitting (z) resulting from the electron spin projection, m_e, grows, and the donor ground state transforms into two doublets, with splittings x and y which depend on the projection of the nuclear spin, m_I. At any given field, the sum of the x and y splittings is equal to the zero field splitting. The two electrons in the donor bound exciton ground state, D^0X, form a spin singlet, therefore, only the projection of the hole spin, m_h, affects the D^0X energy. There are six electic-dipole allowed transitions between the two D^0 Zeeman levels and the four D^0X states, resulting in three x and three y doublets due to the donor hyperfine splitting. The two 'forbidden' transitions with $\Delta m = \pm 2$ are not shown.

A curve fit of the 12 hyperfine components using Lorentzian lineshapes yields an average FWHM of 150 neV, and a selectivity of 25 for one hyperfine state over the other when pumping at the peak of a hyperfine component. To emphasize the remarkable improvement in spectral resolution resulting from the near-elimination of the inhomogeneous isotope broadening that is present in ^{nat}Si, a simulated spectrum of the ^{31}P $D^0 \rightarrow D^0X$ transitions in ^{nat}Si at the same magnetic field is also shown in FIG. 4.6. This was generated by convolving 12 transition lines positioned at the energies of the 12 hyperfine components in ^{28}Si, with each line having the 5 μeV FWHM of the ^{31}P D^0X transition in ^{nat}Si. At the same field, only a broad doublet would be resolved in ^{nat}Si, merely revealing an envelope of the underlying structure. The 272 ns lifetime [55] of the phosphorus D^0X sets a lower limit of ∼2.4 neV on the FWHM.

In FIG. 4.8, one of the hyperfine doublets is compared for three ^{28}Si samples of different enrichment at 1.4 K. The spectrum at 4.2 K for the sample of highest enrichment is also shown, and only a 27% increase in linewidth is observed for an increase in temperature from 1.4 K to 4.2 K. This suggests that temperature does play a role, but it is not a major contributor to the low temperature linewidth. Compared to the well resolved splittings for the sample enriched to 99.991%, the hyperfine splitting for the sample with 99.983% enrichment is barely resolved, while for the sample with 99.92% ^{28}Si it is not resolved. An even more highly resolved spectrum of the ^{28}Si Avo sample, with enrichment of 99.995%, is shown in Section 4.2.4.

These differences can be explained by a simple argument which assumes that inhomogeneous isotope broadening remains the dominant mechanism even at the highest enrichment shown here. Ignoring for simplicity the fact that the proportions of ^{29}Si and ^{30}Si may vary between ^{nat}Si and the enriched ^{28}Si samples, the inhomogeneous isotope broadening will vary as the square root of 100% minus the enrichment (which for ^{nat}Si is 92.23%). The 5 μeV FWHM of the ^{31}P D^0X in ^{nat}Si scales by this simple argument to widths of 510, 230, and 170 neV for the samples shown in FIG. 4.8, in order of increasing enrichment, in remarkably good agreement with what is observed. This suggests that even narrower ensemble linewidths should be achievable in samples with a higher isotopic enrichment.

It should be noted that the spectra shown with an applied magnetic field have so

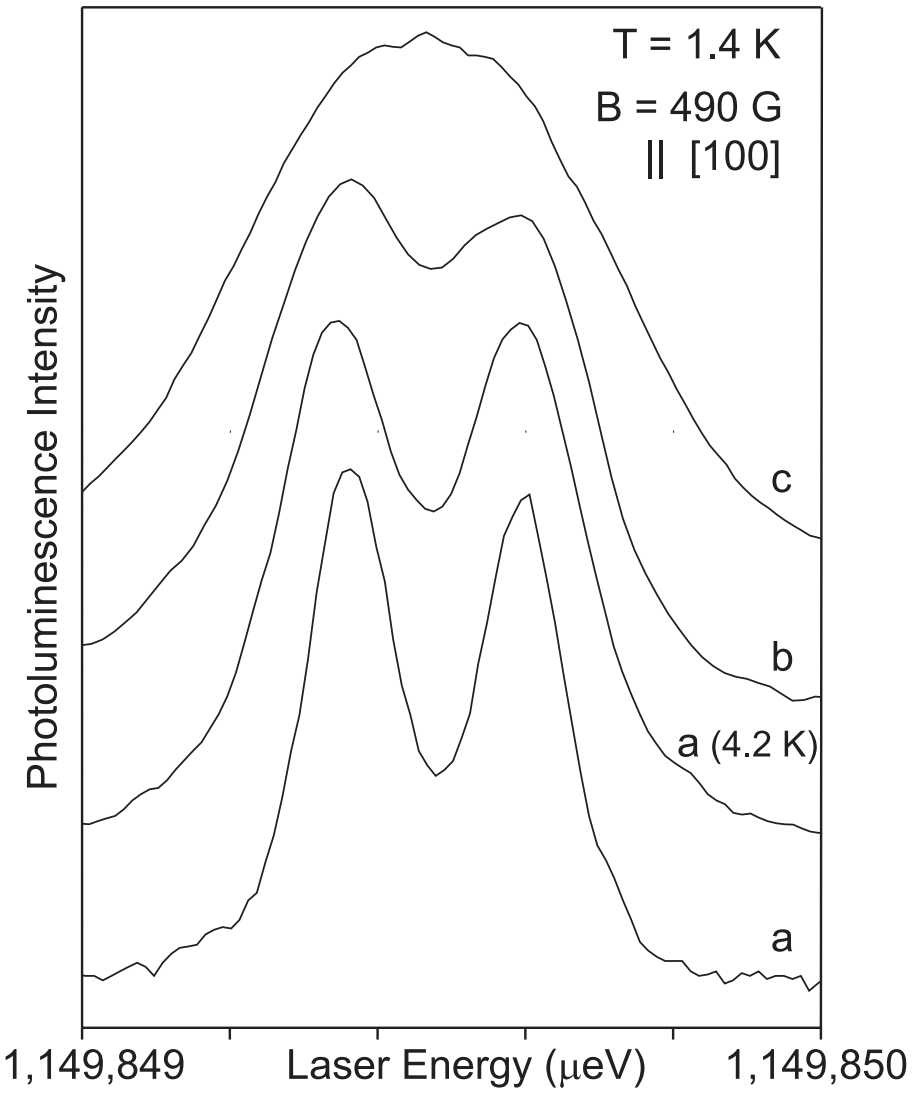

Figure 4.8: Dependence of the ^{31}P D^{0}X PLE line shapes on temperature and isotopic enrichment. The bottom spectrum shows one of the hyperfine doublets for the sample enriched to 99.991% (^{28}Si a), as seen in FIG. 4.6, while directly above it is a spectrum of the same sample at a temperature of 4.2 K (shifted up in energy to compensate for the temperature dependence of the band gap energy). The spectrum labeled b is for a sample enriched to 99.983% ^{28}Si, and the spectrum labeled c is for a sample enriched to 99.92% ^{28}Si, both at 1.4 K.

far been produced using an appropriate amount of above-gap excitation so as to give the best resolved ^{31}P D^0X transition lines and a strong PLE signal. A comparison of the ^{31}P D^0X spectrum for the ^{28}Si a sample (99.991% ^{28}Si) with an applied magnetic field of 490 G parallel to the [001] axis is shown in FIG. 4.9 for different above-gap excitation levels. With 1000 mW of above-gap excitation, the hyperfine doublets are well resolved, similar to those seen in FIG. 4.6, while with only 15 mW, they are just barely resolved. With 5 mW, the hyperfine doublets are not resolved, and with no above-gap excitation, the Zeeman splittings are just barely resolved. As the above-gap excitation power is decreased, the PLE signal decreases significantly, as can be seen in the signal-to-noise of the spectra in FIG. 4.9. The above-gap excitation has several effects: for p-type samples, it photoneutralizes D^+ to give D^0, which is necessary to observe any PLE signal, it also reduces the broadening due to the random electric fields resulting from ionized impurities, and it reduces the saturation effect of the PLE pump laser by randomly ionizing donors (D^0 + free exciton $\rightarrow$ D^0X $\rightarrow$ D^+ + e^-).

Figure 4.10 shows a comparison of the ^{31}P D^0X spectrum at different magnetic fields ranging from 0 to 440 G for the n-type ^{28}Si:P 3.3.6 sample. Although the Zeeman splitting is much smaller at 240 G than at 440 G, all twelve of the hyperfine components are still resolved. In the spectrum collected at 190 G however, different components begin to overlap as the Zeeman splitting becomes even smaller and the hyperfine splittings of the two D^0 branches are no longer equal. At fields under 100 G, the ^{31}P D^0X spectrum no longer resembles the 440 G spectrum that has well-spaced components, but begins to slowly take the shape of the zero-field spectrum shown at the top of FIG. 4.10, which is similar to that previously seen in the top two spectra of FIG. 4.5.

It is also interesting to note that at both ends of each spectrum in FIG. 4.10, a small feature which appears to grow in intensity as the magnetic field decreases, can be observed. This feature, which has not been shown explicitly in any of the previous spectra, is due to the small luminescence signal from the forbidden D^0X transitions, which will be discussed next.

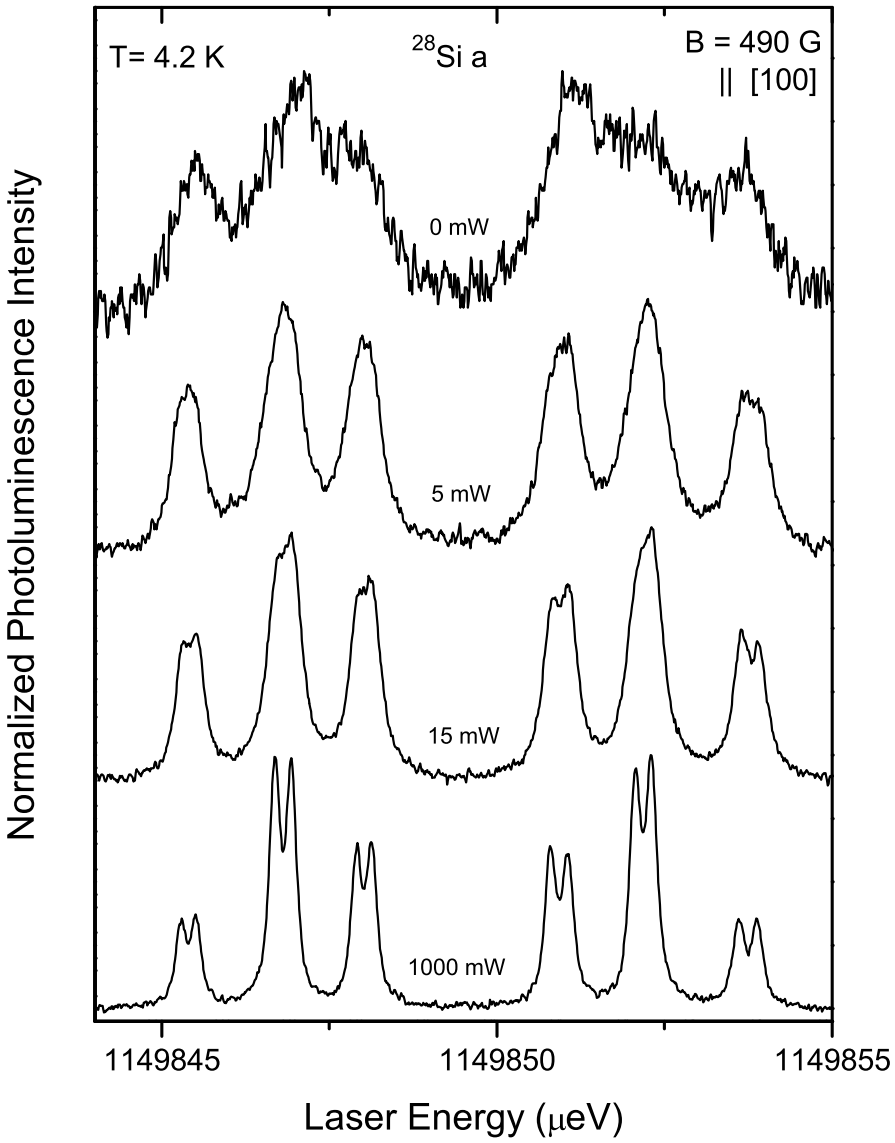

Figure 4.9: A comparison of the ^{31}P D^0X spectra for four different levels of above-gap excitation ranging from 0 to 1000 mW. These spectra for a p-type sample of ^{28}Si enriched to 99.991% (^{28}Si a) under an applied magnetic field of 490 G parallel to the [001] axis show that at low above-gap excitation levels, the hyperfine doublets are not resolved.

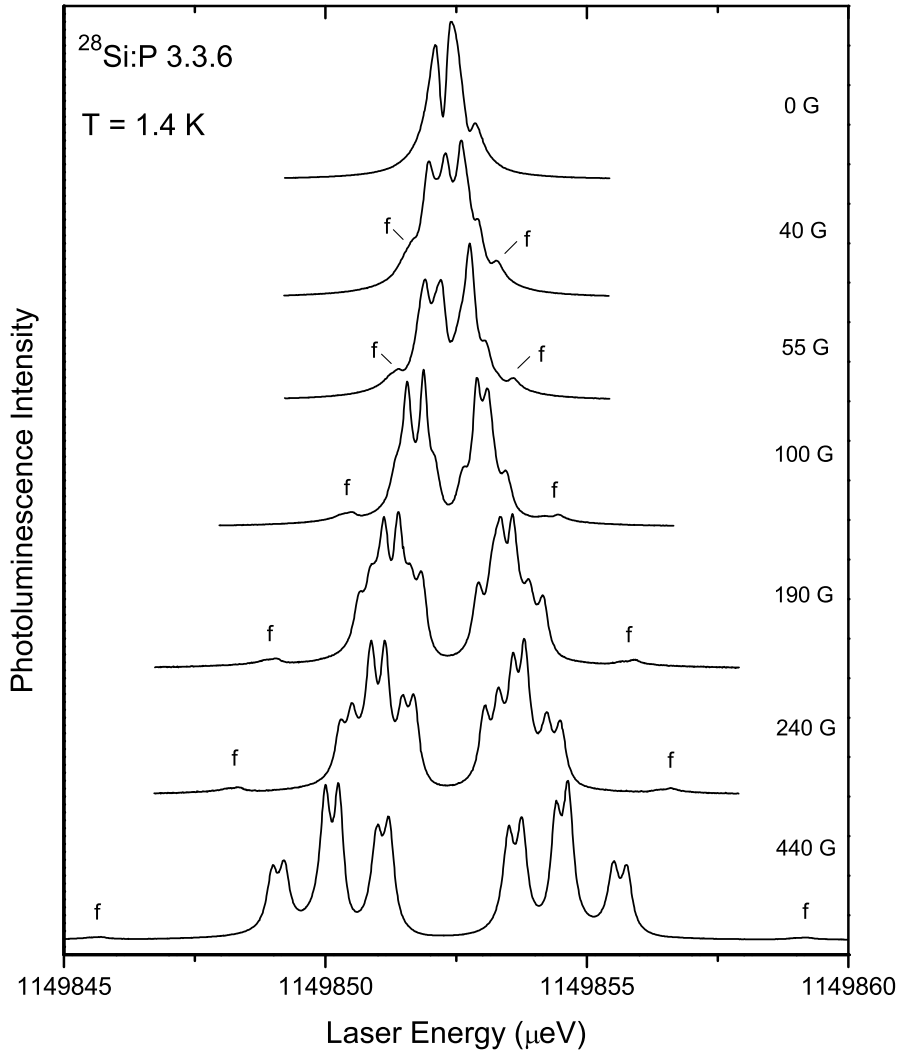

Figure 4.10: PLE spectra of the ^{31}P D^0X for the n-type ^{28}Si:P 3.3.6 sample at different magnetic fields ranging from 0 to 440 G, parallel to the [001] axis. f labels the electric-dipole forbidden transitions.

4.1.3 The forbidden transitions

As seen in FIG. 4.10, the electric-dipole forbidden transitions do indeed produce a small luminescence signal in the ^{31}P D^0X spectrum. The two pairs of doublets which correspond to a change in the projection of the spin angular momentum, Δm, of ± 2 between D^0 and D^0X can be seen at the low and high energy ends of the spectrum in FIG. 4.11. This ^{31}P D^0X spectrum was collected with a magnetic field of 440 G parallel to the [001] axis for the n-type ^{28}Si:P 3.3.6 sample. The $m_e = +1/2 \rightarrow m_h = -3/2$ transition in the $D^0 \rightarrow D^0X$ process is responsible for the forbidden doublet at the low energy end, while the doublet at the high energy end is due to the $m_e = -1/2 \rightarrow m_h = +3/2$ transition. In the spectrum shown in FIG. 4.11, the forbidden transitions have a relative intensity of only approximately 1% when compared to the strongest allowed hyperfine doublets at this field. A ten times magnification of the forbidden doublets, also shown in FIG. 4.11, reveals that in both cases, the higher energy component is slightly more intense than the one at lower energy.

As shown in FIG. 4.7, the donor hyperfine states consist of two parallel spin states $|\uparrow\Uparrow\rangle$ and $|\downarrow\Downarrow\rangle$, which are not coupled by the hyperfine interaction, and two anti-parallel states $|\uparrow\Downarrow\rangle$ and $|\downarrow\Uparrow\rangle$, which are somewhat mixed by the hyperfine interaction. In the notation used here, the first label is used to indicate the electron spin state (m_e) and the second label indicates the nuclear spin state (m_I). The lower energy component of the forbidden doublets is due to donors in the $|\uparrow\Uparrow\rangle$ and $|\downarrow\Downarrow\rangle$ states at the low and high energy ends of the spectrum, respectively, while the higher energy component at the low and high energy ends is due to donors in the $|\uparrow\Downarrow\rangle$ and $|\downarrow\Uparrow\rangle$ states, respectively. This suggests the possibility that the hyperfine mixing present in the $|\uparrow\Downarrow\rangle$ and $|\downarrow\Uparrow\rangle$ states is responsible for the higher relative intensities since the admixtures include states that have electric-dipole allowed transitions.

The forbidden transitions become relatively stronger in intensity as the magnetic field decreases, as can be seen in FIG. 4.12, which shows the ^{31}P BE spectrum with a magnetic field of 100 G parallel to the [001] axis. A curve fit of the forbidden doublets reveals the deconvolved components, also shown in FIG. 4.12. Since the hyperfine splitting of the lower D^0 branch becomes larger and that of the upper branch becomes smaller at lower magnetic field, the forbidden doublet at the high energy end is better

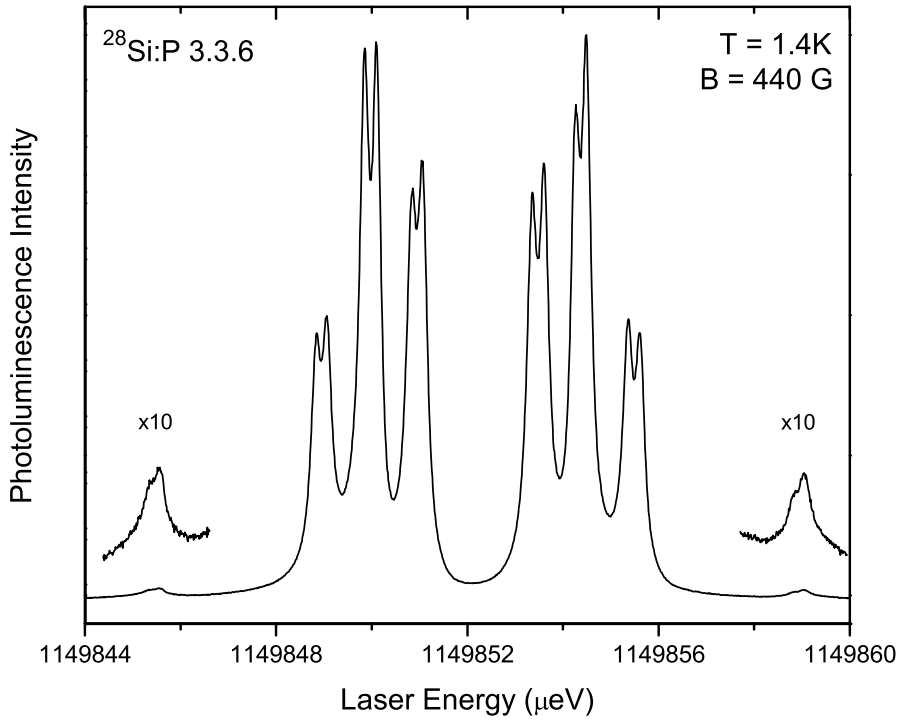

Figure 4.11: PLE spectrum of the ^{31}P D^0X for the n-type ^{28}Si:P 3.3.6 sample with a magnetic field of 440 G parallel to the [001] axis. At the low and high energy ends of this spectrum are small doublets resulting from the forbidden transitions. A ten times magnification of the two doublets is shown for clarity.

resolved than the doublet at the low energy end.

Comparing with the 440 G spectrum in FIG. 4.11, there does not appear to be a noticeable difference in the relative intensities of the doublet components. At lower magnetic field, as the hyperfine mixing of the anti-parallel hyperfine states ($|\uparrow\Downarrow\rangle$ and $|\downarrow\Uparrow\rangle$) increases, the higher energy ('mixed') component would be expected to increase in intensity relative to the lower energy ('pure') component, but the fact that this is not observed suggests that further investigation in the future is required to determine the full details of the forbidden transitions.

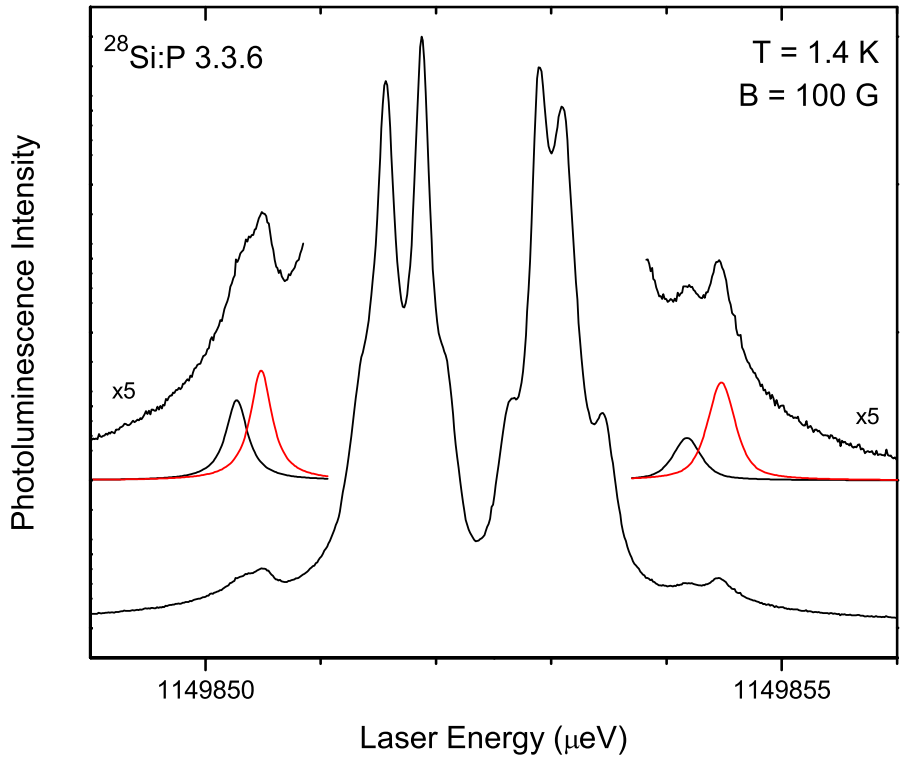

Figure 4.12: PLE spectrum of the ^{31}P D^0X for the n-type ^{28}Si:P 3.3.6 sample with a magnetic field of 100 G parallel to the [001] axis. At this field, there is significant overlap of the individual hyperfine components, while the forbidden transitions have increased in intensity as compared to the spectrum at 440 G shown in FIG. 4.11. The forbidden transitions at the low and high energy ends of the spectrum are shown magnified by five times, and the deconvolved components, obtained from curve fitting, are also shown.

4.1.4 Photoconductivity measurement of ^{31}P bound exciton spectrum

Shallow donor and acceptor bound excitons in silicon and other indirect band gap semiconductors have very low radiative quantum efficiencies due to the dominance of nonradiative Auger recombination, which is a drawback for optical detection of bound excitons as in PL or PLE. For the ^{31}P D^0X, the observed 272 ns lifetime is essentially equal to the Auger lifetime, since the radiative lifetime is $\sim$2 ms. [55] However, it is possible to make use of the near-unity efficiency of the Auger process by detecting the free electrons released in Auger recombination. The absorption spectrum of the ^{31}P D^0X, as revealed by photocurrent spectroscopy rather than by PLE, is shown in FIG. 4.13 for conditions similar to those used in FIG. 4.6. Strains generated by the electrical contacts to the sample are likely responsible for the reduced resolution of FIG. 4.13 as compared to FIG. 4.6, but the hyperfine splittings are still clearly resolved. Since the sample used to produce the spectrum in FIG. 4.13 is p-type, the dominant impurity, boron, produces a large nonresonant hole photocurrent, and the electrons released from the Auger recombination cause a reduction in the nonresonant background so that the ^{31}P D^0X spectrum appears inverted. Although a significantly higher signal-to-noise ratio would be expected to be observed in the photocurrent spectrum compared to the PLE spectrum previously shown in FIG. 4.6, as a result of the near-unity quantum efficiency of the Auger process, this is in fact not the case for the spectrum in FIG. 4.13, which suggests that the method used to prepare the electrical contacts does not yield a good ohmic contact to the sample. A variation of the photoconductivity method using a contactless capacitive technique is discussed in Section 4.2.4.

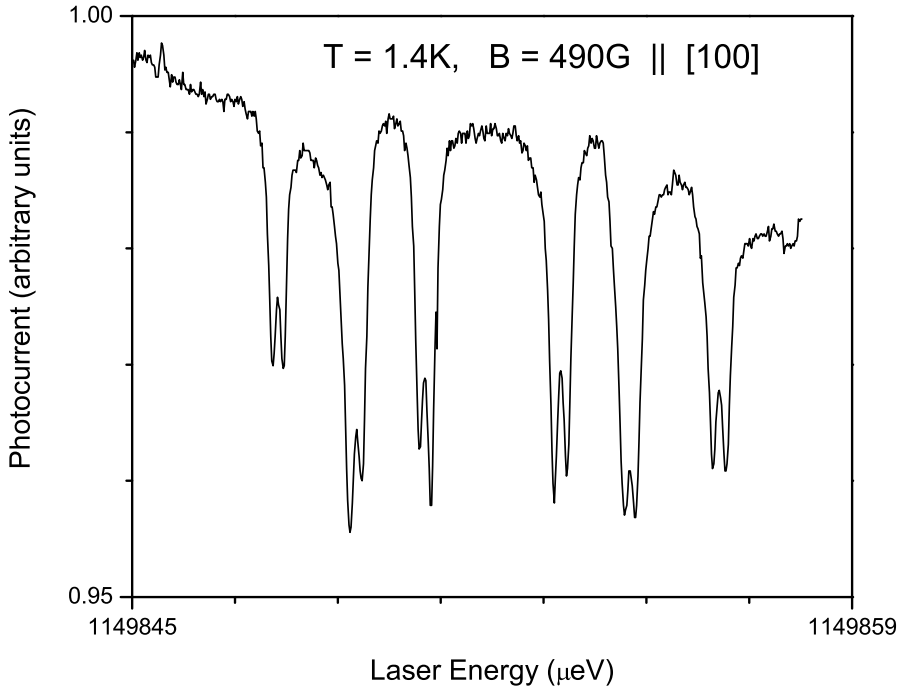

Figure 4.13: Photocurrent spectrum of the ^{31}P D^0X for a p-type ^{28}Si sample enriched to 99.991% (^{28}Si a) with a magnetic field of 490 G applied parallel to the [001] axis. The electrons released from the D^0X Auger recombination reduce the larger nonresonant hole photocurrent from the dominant impurity, boron.

4.1.5 Measurement of ^{31}P bound exciton spectrum by laser absorption

Another method of measuring the ^{31}P D^0X spectrum is by measuring the transmission of the resonant laser through the sample. The zero field transmittance spectrum of the ^{31}P D^0X transition is shown in FIG. 4.14 for the n-type ^{28}Si:P 3.3.7 sample. The peak absorbance of 4.3% can be used to determine the absorption coefficient of this sample. The absorption coefficient is given by:

$$\alpha = \frac{-ln\left(\frac{I_{trans}}{I_0}\right)}{t} \tag{4.2}$$

where I_0 is the incident laser intensity, I_{trans} is the transmitted laser intensity and t is the distance of material through which the laser travels (i.e., the thickness of the sample). Using $I_{trans} = (1-0.043)I_0$ and $t = 8.97\,\text{mm}$, the peak absorption coefficient is $\alpha_{peak} = 0.049\,/\text{cm}$. The integrated absorption can be measured approximately by comparing the integrated area with the area of a triangle of height equal to the peak absorption of 0.043 and with a base of $\sim$1.4 μeV. This yields an integrated absorption of $\sim 3.0 \times 10^{-8}\,\text{eV}$, and using $I_{trans} = (1 - 3.0 \times 10^{-8})I_0$, the integrated absorption coefficient is found to be $\alpha = \sim 3.4 \times 10^{-8}\,/\text{cm}$. The ^{28}Si:P 3.3.7 sample has a ^{31}P concentration of $\sim 7 \times 10^{14}\,\text{cm}^{-3}$, so that the absorption coefficient per ^{31}P donor is $\sim 5 \times 10^{-23}\,/\text{cm}/\text{cm}^{-3}$.

The transmittance spectrum of the ^{31}P D^0X distribution for the same sample with an applied magnetic field of 440 G parallel to the [001] axis is shown in FIG. 4.14. In this case, the peak absorbance is only 0.8%. The fact that the two transmittance spectra shown here are similar in appearance to the PLE spectra shown previously confirms that PLE and absorption are eqivalent processes for measuring the spectrum of the ^{31}P D^0X transition, but the advantage of PLE over absorption for such a weakly absorbing transition is obvious from the relative signal-to-noise levels.

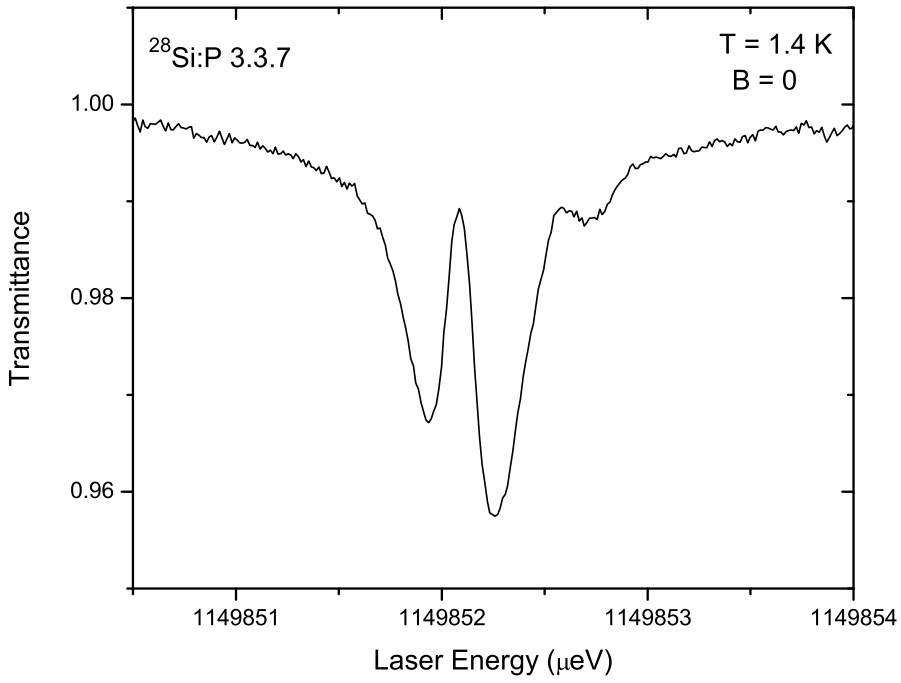

Figure 4.14: Transmittance spectrum of the ^{31}P D^0X for the n-type ^{28}Si:P 3.3.7 sample. This zero magnetic field spectrum has a peak absorbance of 4.3%, for a path length of $\sim$9 mm.

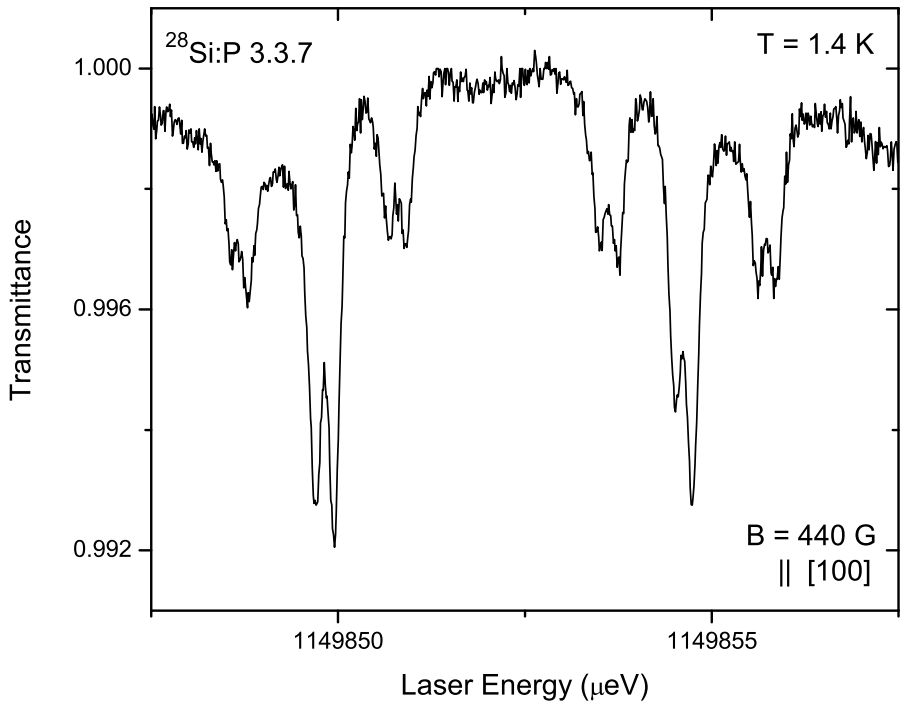

Figure 4.15: Transmittance spectrum of the ^{31}P D^0X for the n-type ^{28}Si:P 3.3.7 sample with a magnetic field of 440 G applied parallel to the [001] axis. The peak absorbance in this spectrum is 0.8%.

4.1.6 Possible applications in quantum computing

The results presented thus far suggest a number of applications related to silicon-based quantum computing. Kane's [38] proposal that the nuclear spins of ^{31}P in Si could be used as the basis for qubits in quantum computation, led to many subsequent proposals related to the problem of detecting the nuclear spin state. Many of these were based on Kane's [38] original idea of spin-to-charge conversion, while others suggested approaches such as magnetic resonance force microscopy on single nuclear spins [69] or on ensembles of identical nuclear spins [70]. Based on the observation [23] of reduced ^{31}P D^0X linewidths in ^{28}Si as compared to ^{nat}Si, Fu et al. [71] suggested that it might be possible to detect the state of a single ^{31}P nuclear spin using the hyperfine splitting of the D^0X PL transition. With ensemble linewidths of 150 neV and well resolved hyperfine splittings it may be possible to adopt an optical readout scheme for measuring the nuclear spin state.

One drawback of the optical readout scheme is the very low radiative quantum efficiency of these bound excitons. It was demonstrated in FIG. 4.13 that the near-unity efficiency Auger recombination can be used to observe the D^0X spectrum, via the photocurrent spectrum, showing well-resolved hyperfine splittings. The ability to resonantly ionize neutral ^{31}P donors in specific electron and nuclear spin states suggests a potential readout mechanism for single nuclear spins: the optical-nuclear spin transistor. In this scheme the spin-selective Auger photoionization of a single neutral ^{31}P by the resonant creation of a bound exciton would be detected by the resulting change in current in a nearby narrow channel field-effect transistor (FET) or single electron transistor.

The spectrum in FIG. 4.6 shows that there is a small degree of polarization of the nuclear spins, even though the experiment was not optimized to achieve such polarization. This suggests the possibility of achieving electron and nuclear polarizations by dynamic optical pumping using a second tunable single-frequency laser. Obtaining a highly polarized nuclear spin state is essential for initializing the qubits in a quantum computer.

4.2 Hyperpolarization of the electron and nuclear spin states of ^{31}P donors in ^{28}Si

In most silicon-based quantum computing schemes involving electron or nuclear spins [38–40, 72, 73], ^{28}Si is used, since the removal of the ^{29}Si nuclear spin results in very long coherence times [72, 74–76]. Several methods for achieving quantum logic using spin states of ^{31}P in ^{28}Si have been proposed [38–40] and the manipulation of electron and nuclear spin coherences have been demonstrated [72], but the problem of the detection of single spins, and also of the initialization (or polarization) of these spins, remain largely unsolved.

Electron and nuclear spin polarization in silicon has been studied for decades [77–86], but the nuclear polarization obtained to date has typically been less than a few percent, and requires thousands of seconds to establish. Recently, a ^{31}P nuclear polarization of 68% has been reported [86] in a high magnetic field, using a variation of a mechanism first proposed in 1959 [79], and demonstrated in InSb in 1963 [80], but the time constant was still a relatively long 150 s. The optical pumping method presented in this section works at low magnetic field, and can simultaneously hyperpolarize both the electron and nuclear spins of ^{31}P in less than a second.

4.2.1 Preliminary attempts at obtaining electron and nuclear spin polarizations in p-type ^{28}Si

Prior to the implementation of the locking and scanning mechanism described in Section 3.2, preliminary attempts were made to achieve electron and nuclear polarizations in ^{28}Si by dynamic optical pumping. These attempts however yielded only relatively small net electron and nuclear polarizations [87] of approximately 50% and 25%, respectively, due to the fact that the available samples of ^{28}Si with sufficiently high enrichment to resolve the D^0X hyperfine transitions were p-type, with residual boron acceptor concentrations typically ten times the ^{31}P concentration. All donors in these samples would therefore be ionized (D^+) at low temperature, unless above-gap excitation was used to provide photoneutralization. The addition of above-gap excitation has a strong negative effect on the achievable electron and nuclear polarizations,

since it acts to equalize the populations in the four D^0 hyperfine states.

The PLE spectrum that results when the pump laser is tuned to line 4 (the $m_e = -1/2, m_I = +1/2 \rightarrow m_h = -3/2$ transition) is shown in FIG. 4.16. This spectrum shows that there is an electron polarization of ∼50%, since the electron spin state alternates for each successive hyperfine doublet. It appears that the nuclear polarization is also ∼50%, but because the energies of the nuclear spin states of the hyperfine doublets reverse for the opposite electron spin, the net nuclear polarization is only ∼25%.

The net electron and nuclear polarizations are determined from the populations in the four hyperfine states. The net electron polarization P_e is given by:

$$P_e = \frac{\left(\rho_{|\uparrow\Uparrow\rangle} + \rho_{|\uparrow\Downarrow\rangle}\right) - \left(\rho_{|\downarrow\Uparrow\rangle} + \rho_{|\downarrow\Downarrow\rangle}\right)}{\left(\rho_{|\uparrow\Uparrow\rangle} + \rho_{|\uparrow\Downarrow\rangle}\right) + \left(\rho_{|\downarrow\Uparrow\rangle} + \rho_{|\downarrow\Downarrow\rangle}\right)} \tag{4.3}$$

where $\rho_{|\uparrow\Uparrow\rangle}$, $\rho_{|\uparrow\Downarrow\rangle}$, $\rho_{|\downarrow\Uparrow\rangle}$, and $\rho_{|\downarrow\Downarrow\rangle}$ are the populations in the $|\uparrow\Uparrow\rangle$, $|\uparrow\Downarrow\rangle$, $|\downarrow\Uparrow\rangle$, and $|\downarrow\Downarrow\rangle$ states, respectively. A positive value of P_e corresponds to a net electron polarization in the $m_e = +\frac{1}{2}$ spin state, while a negative value corresponds to polarization in the $m_e = -\frac{1}{2}$ spin state.

Since each transition in the PLE spectrum shown in FIG. 4.16 is associated with a specific electron spin state and nuclear spin state, the populations in the four hyperfine states can be determined from the relative intensities of these transitions, so that the net electron polarization P_e is given by:

$$P_e = \frac{[(I_1 + I_5 + I_9) + (I_2 + I_6 + I_{10})] - [(I_4 + I_8 + I_{12}) + (I_3 + I_7 + I_{11})]}{\sum_{n=1}^{12} I_n} \tag{4.4}$$

where I_n is the integrated intensity found by curve fitting to transition n.

Similarly, the net nuclear polarization P_n is given by:

$$P_n = \frac{\left(\rho_{|\uparrow\Uparrow\rangle} + \rho_{|\downarrow\Uparrow\rangle}\right) - \left(\rho_{|\uparrow\Downarrow\rangle} + \rho_{|\downarrow\Downarrow\rangle}\right)}{\left(\rho_{|\uparrow\Uparrow\rangle} + \rho_{|\downarrow\Uparrow\rangle}\right) + \left(\rho_{|\uparrow\Downarrow\rangle} + \rho_{|\downarrow\Downarrow\rangle}\right)} \tag{4.5}$$

and in terms of the integrated intensities of the transitions in the PLE spectrum, Equation 4.5 can be written as:

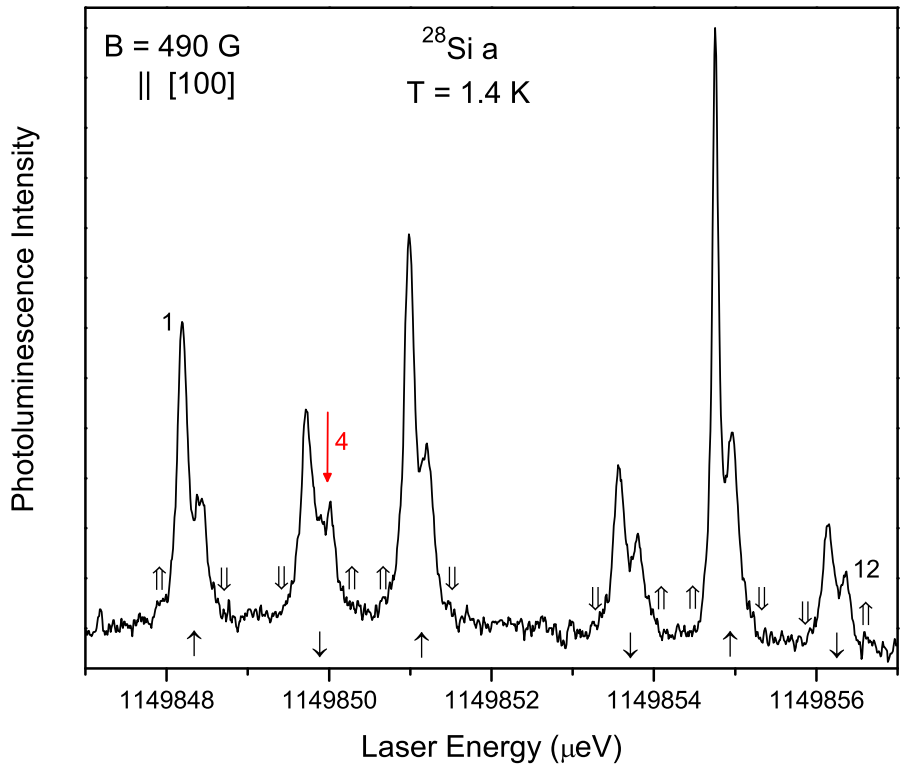

Figure 4.16: PLE spectrum of the ^{31}P D^{0}X for a p-type ^{28}Si sample (^{28}Si a), with the pump laser tuned to line 4 (the $m_e = -1/2, m_I = +1/2 \rightarrow m_h = -3/2$ transition), as indicated by the arrow above the transition. The resulting net electron and nuclear polarizations are $\sim$50% and $\sim$25%, respectively. The arrows below each of the doublets indicate the electron spin projection of each corresponding doublet, while the double arrows beside each of the hyperfine components indicate the ^{31}P nuclear spin projection of each corresponding component.

$$P_n = \frac{[(I_1 + I_5 + I_9) + (I_4 + I_8 + I_{12})] - [(I_2 + I_6 + I_{10}) + (I_3 + I_7 + I_{11})]}{\sum_{n=1}^{12} I_n} \tag{4.6}$$

The populations in the four hyperfine states can be determined using the integrated intensities of only four of the transitions in the PLE spectrum which have the same oscillator strength, for example, lines 5, 6, 7, and 8, so that P_e and P_n can be expressed simply as:

$$P_e = \frac{(I_5 + I_6) - (I_7 + I_8)}{(I_5 + I_6) + (I_7 + I_8)} \tag{4.7}$$

and

$$P_n = \frac{(I_5 + I_8) - (I_6 + I_7)}{(I_5 + I_8) + (I_6 + I_7)} \tag{4.8}$$

4.2.2 Hyperpolarization of electron and nuclear spins in n-type ^{28}Si

The results presented here were made possible by a recently grown crystal of ^{28}Si intentionally doped with ^{31}P. This n-type sample allowed for optical pumping of the $D^0 \rightarrow D^0X$ transitions without any additional above-gap excitation, resulting in dramatically larger polarizations than those obtained in the preliminary attempts. An electron polarization of 90% and nuclear polarization of 76% were obtained simultaneously in less than a second, in a magnetic field and temperature regime where the equilibrium electron polarization was only ∼2%, and the nuclear polarization $\sim 3 \times 10^{-3}$ %.

The 12 electric-dipole allowed $D^0 \rightarrow D^0X$ transitions are shown in FIG. 4.17, and are labeled 1 to 12 in order of increasing energy. The D^0 hyperfine states consist of two parallel spin states $|\uparrow\Uparrow\rangle$ and $|\downarrow\Downarrow\rangle$ which are not coupled by the hyperfine interaction, and two anti-parallel states $|\uparrow\Downarrow\rangle$ and $|\downarrow\Uparrow\rangle$ which are somewhat mixed by the hyperfine interaction. The $D^0 \rightarrow D^0X$ transitions labelled π, corresponding to $\Delta m = 0$, occur when the polarization of the resonant excitation light is parallel to the magnetic field

direction, while the transitions labelled σ, corresponding to $\Delta m = \pm 1$, occur when the polarization is perpendicular to the field.

The unpumped spectrum for the n-type ^{28}Si:P 3.3.6 sample is shown at the bottom of FIG. 4.18, and is very similar to the spectrum for the p-type sample shown in FIG. 4.6, with the only difference being that the spectral resolution of the hyperfine transitions is slightly lower, with a FWHM of 220 neV (54 MHz) for the n-type sample as compared to 150 neV (37 MHz) for the p-type sample. This small increase in linewidth is likely due either to concentration broadening from the ^{31}P, or to an unintentional reduction of the isotopic enrichment. As expected, the populations in the four D^0 hyperfine states are essentially equal under these conditions. It is important to note that in order to obtain the unpumped spectrum at the bottom of FIG. 4.18, a small amount of above-gap excitation from a 1047 nm Nd:YLF laser was required in addition to the PLE probe laser. This is not because of a need for photoneutralization, as for the p-type samples, but rather because in the absence of any excitation other than the PLE probe laser, the probe itself strongly polarizes the D^0 hyperfine populations. This pumping effect of the probe laser results in a weak and distorted PLE spectrum in which the hyperfine doublets are not resolved, as shown in FIG. 4.19, but these saturation effects can be circumvented by repopulating the hyperfine states equally with a small amount of above-gap excitation from the 1047 nm laser.

For the other PLE spectra shown in FIG. 4.18, a much stronger pump laser ($\sim$ 2.8 Wcm^{-2}) was tuned to the desired energy while the PLE probe laser ($\sim$ 6.5×10^{-2} Wcm^{-2}) was scanned across the transitions. No above-gap excitation was necessary for these spectra, since the pump laser held the populations of the hyperfine states essentially fixed, and any above-gap excitation would act to reduce the electron and nuclear polarizations. A drawback of not using any above-gap excitation for this particular n-type sample is that the PLE lines are slightly broadened and develop a low energy tail. This results from Stark broadening due to the $\sim 1 \times 10^{14}$ cm^{-3} of ionized boron and phosphorus that are present in the absence of above-gap excitation. This broadening could be made negligible in a sample with a lower boron concentration.

A comparison of the resulting ^{31}P D^0X spectrum when the PLE pump laser is

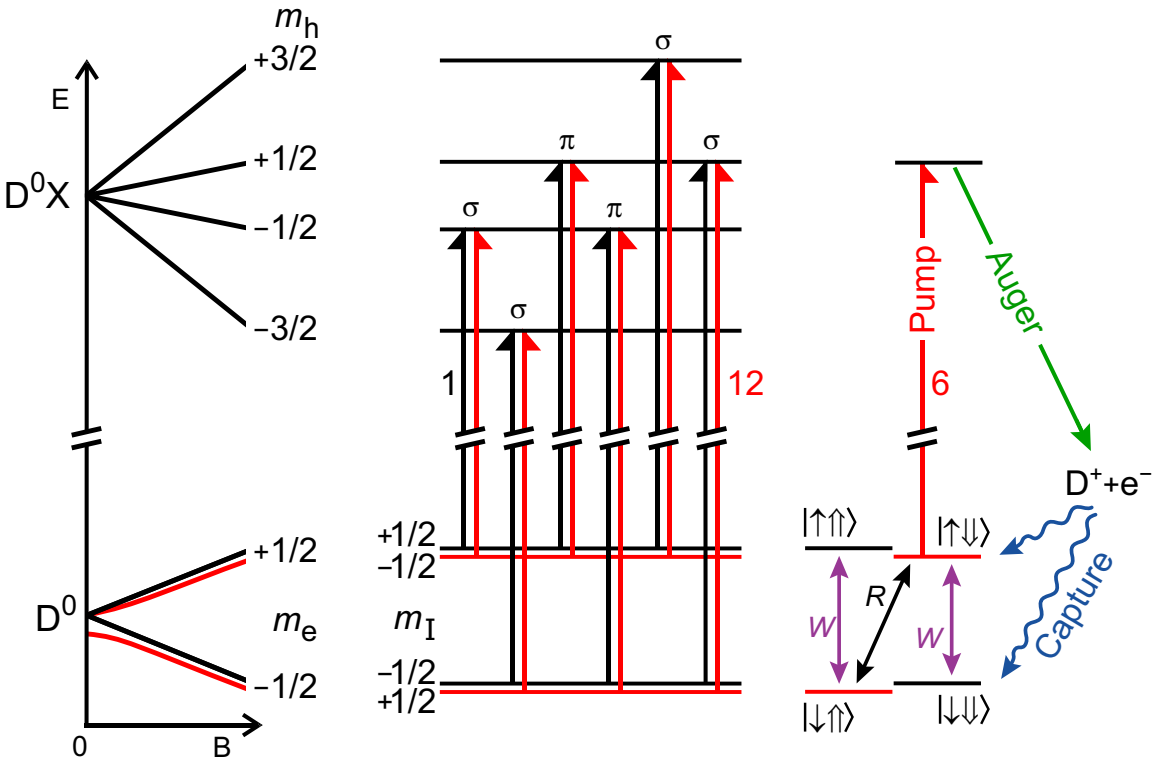

Figure 4.17: The Zeeman splittings of the neutral donor ground state (D^0) and the donor bound exciton (D^0X) under an applied magnetic field are shown on the left, while in the centre, the twelve allowed optical transitions between the four D^0 hyperfine states and the four D^0X states are shown, numbered from 1 to 12 in order of increasing energy. On the right is a simplified schematic of the optical polarization mechanism for the pump laser tuned to line 6.

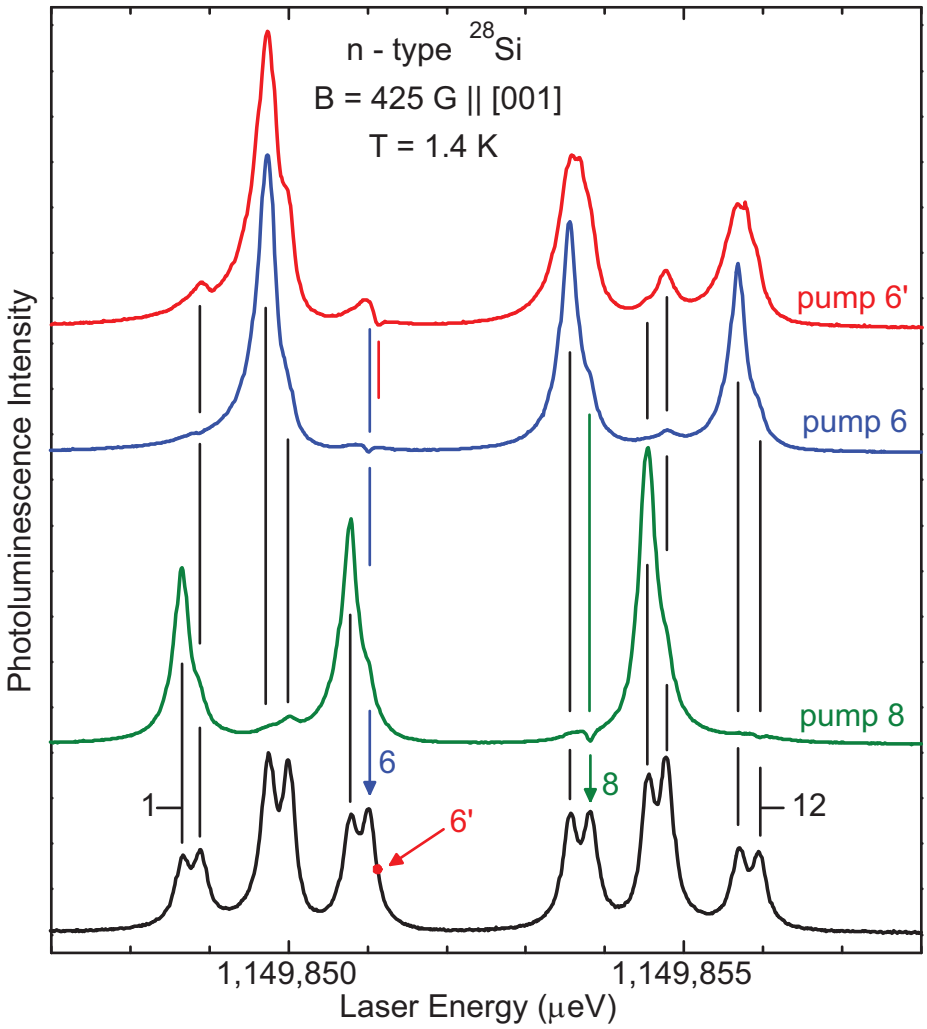

Figure 4.18: PLE spectra of the ^{31}P bound exciton in an n-type ^{28}Si sample (^{28}Si:P 3.3.6), revealing electron and nuclear polarizations obtained by selective optical pumping. At bottom is a spectrum without any resonant pumping, showing essentially equal populations in the four D^0 states. The upper spectra show the PLE signal when a strong pump field is tuned to either line 6 or line 8, or the half-height point on the high energy side of line 6, which is indicated as 6′.

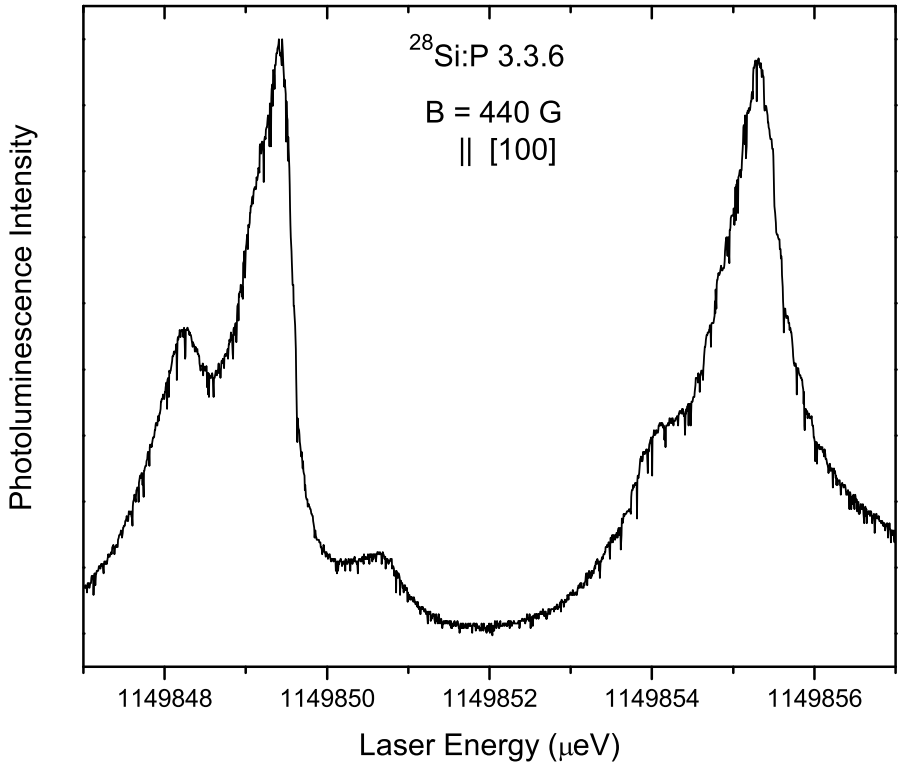

Figure 4.19: PLE spectrum of the ^{31}P D^0X for the n-type ^{28}Si:P 3.3.6 sample with an applied magnetic field of 440 G parallel to the [001] axis and with no above-gap excitation. The negative spikes are detector-related.

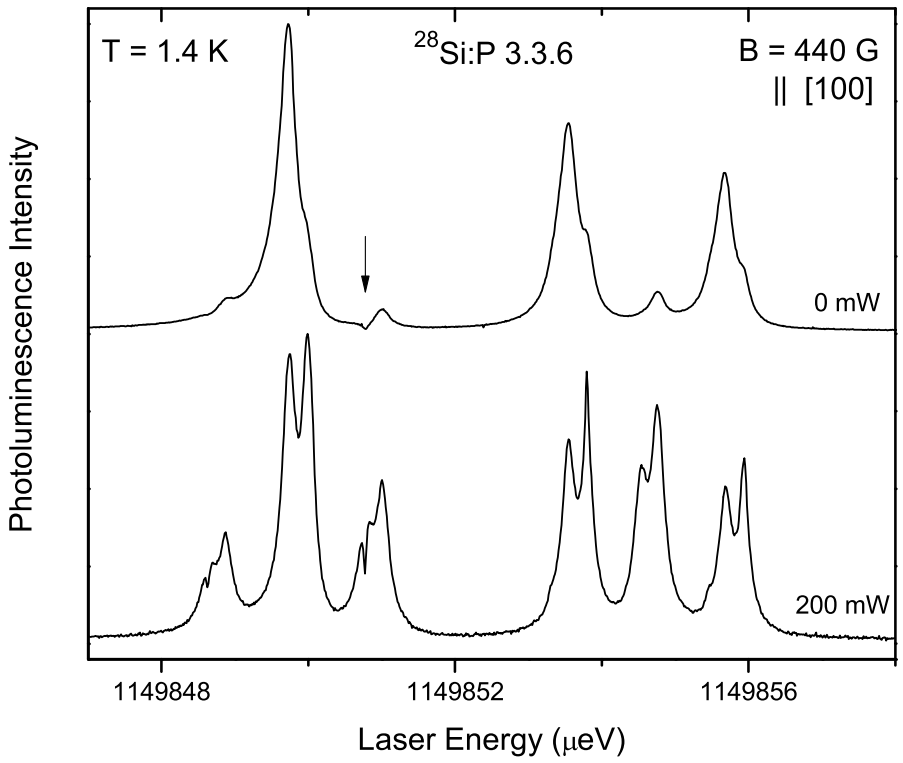

Figure 4.20: A comparison of the ^{31}P D^0X spectrum when the PLE pump laser is tuned to line 5 (as marked by the arrow), with and without above-gap excitation, under an applied magnetic field of 440 G parallel to the [001] axis. Without above-gap excitation, the electron and nuclear polarizations are much higher than when 200 mW of above-gap excitation is used.

tuned to line 5 is shown in FIG. 4.20. The bottom spectrum shows the PLE signal when 200 mW of above-gap excitation is used, while the top spectrum, which has significantly higher electron and nuclear polarizations, shows the PLE signal when no above-gap excitation is used. The effect is so dramatic that the nuclear polarizations for the electron population that is not being pumped, are in opposite directions in the two spectra.

Figure 4.21 shows a comparison of line 7 when the pump laser is tuned to line 5, with no above-gap excitation and with 200 mW. Without above-gap excitation, the line is noticeably broader, developing a low energy tail due to Stark broadening. In order to curve fit the Stark broadened PLE lines, a skewed Lorentzian function with a low energy edge of the following form was used:

$$L(x) = \begin{cases} \frac{1}{1+\left(\beta\left(\frac{x-x_0}{\gamma}\right)\right)^2} & \text{for } x < x_0 \\ \frac{1}{1+\left(\frac{x-x_0}{\gamma}\right)^2} & \text{for } x \geq x_0 \end{cases} \tag{4.9}$$

In Eq. 4.9, x_0 is the position of the peak and γ is the half width at half maximum (HWHM) of the high energy side ($x \geq x_0$) of the function, while $\frac{\gamma}{\beta}$ is the HWHM of the low energy side ($x < x_0$) of the function. Values between 0.7 and 0.9 for β were used for curve fitting the Stark broadened PLE lines. This functional form yielded good fits of the lines within the signal-to-noise for the pumped spectra in FIG. 4.18.

In FIG. 4.18, the resulting spectra for pumping line 6 and line 8 are shown. These are the two cases for which the largest (and opposite) electron and nuclear polarizations are observed. These spectra reveal an extremely high electron polarization, with transitions from D^0 states having the same electron spin as the pumped state almost vanishing from the spectra. A large nuclear polarization in the hyperfine doublets for the opposite electron spin state is also observed. The top spectrum of FIG. 4.18 shows the result when the pump laser was tuned to the half height point on the high energy side of line 6, referred to as $6'$. At this position, the hyperfine selectivity is higher than at the peak of line 6, since the contribution from the high energy tail of line 5 is reduced, while the contribution from the low energy tail of line 7, which is much further away, remains negligible. The results under the conditions of FIG. 4.18 are summarized in TABLE 4.1, which gives the observed populations of the four D^0

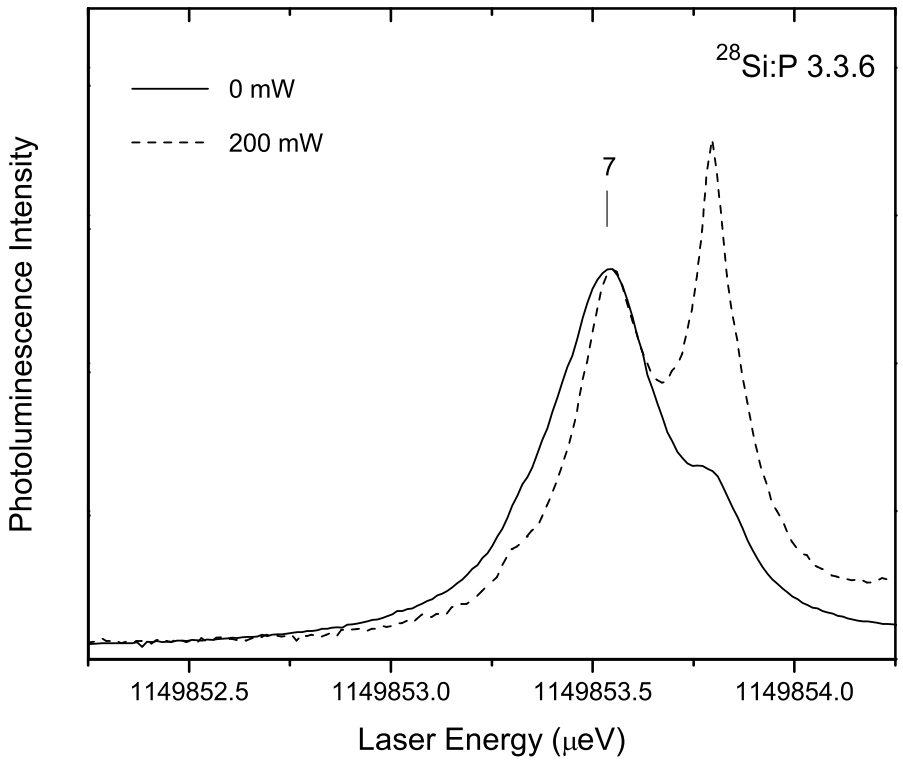

Figure 4.21: A comparison of line 7 in the ^{31}P D^0X spectrum when the PLE pump laser is tuned to line 5, with and without above-gap excitation, under an applied magnetic field of 440 G parallel to the [001] axis. Without above-gap excitation, the lines are broader and develop a low energy tail due to Stark broadening. The vertical axes of both spectra have been scaled to align the peaks of line 7 for comparison.

Table 4.1: D^0 populations and net electron and nuclear polarizations for optical pumping in n-type ^{28}Si with no above-gap excitation.

Pump	Populations (%)				Polarization(%)	
line	$\|\uparrow\Uparrow\rangle$	$\|\uparrow\Downarrow\rangle$	$\|\downarrow\Downarrow\rangle$	$\|\downarrow\Uparrow\rangle$	Elec.	Nucl.
3 $\|\downarrow\Downarrow\rangle$	44	38	4	14	64	16
4 $\|\downarrow\Uparrow\rangle$	63	22	7	8	70	42
5 $\|\uparrow\Uparrow\rangle$	1	8	75	16	-82	-66
6 $\|\uparrow\Downarrow\rangle$	1	4	84	11	-90	-76
6′ $\|\uparrow\Downarrow\rangle$	2	11	64	23	-74	-50
7 $\|\downarrow\Downarrow\rangle$	64	26	1	9	80	46
8 $\|\downarrow\Uparrow\rangle$	76	18	2	4	88	60
9 $\|\uparrow\Uparrow\rangle$	3	15	43	39	-64	-16
10 $\|\uparrow\Downarrow\rangle$	4	5	70	21	-82	-50

hyperfine states obtained by curve fitting to the spectra, and the resulting net electron and nuclear polarizations, when pumping at the peaks of lines 3 through 10 (pumping lines 1, 2, 11 and 12 give results very similar to lines 5, 6, 7 and 8, respectively). Results identical to these were obtained when the pump and probe intensities were both reduced by a factor of one hundred, indicating that high intensity is not needed to obtain high polarization. Also, when the magnetic field was doubled and quadrupled, essentially identical results were obtained (except of course for the energies of the transitions).

The basic mechanism responsible for these polarizations is outlined on the right hand side of FIG. 4.17 for the case of pumping line 6. Only D^0 in the $|\uparrow\Downarrow\rangle$ hyperfine state are converted into D^0X, which decay with high probability to ionized donors (D^+) plus free electrons (e^-), due to the dominance of Auger recombination [55] for D^0X in silicon. Subsequent electron capture may then populate the opposite donor electron spin state. The pure nuclear relaxation rate is assumed to be negligible and therefore not shown, and the pump rate is assumed to be much higher than either the optically enhanced electron relaxation rate W, or the cross relaxation rate R. Population is therefore removed directly from $|\uparrow\Downarrow\rangle$, and also from $|\uparrow\Uparrow\rangle$ and $|\downarrow\Uparrow\rangle$,

since these are coupled to $|\uparrow\Downarrow\rangle$ via R and W relaxation, and builds up in $|\downarrow\Downarrow\rangle$ to the extent that the effective pump rate exceeds W.

This mechanism is consistent with the results presented in TABLE 4.1, where it is seen that for a given hyperfine doublet, pumping the higher energy (i.e., even-numbered) component results in higher net electron and nuclear polarizations as compared to the lower energy (i.e., odd-numbered) component. For example, when pumping line 6, as in FIG. 4.17, population builds up in the $|\downarrow\Downarrow\rangle$ state due to the direct capture of free electrons into this state following Auger recombination and also due to the removal of population from the three other hyperfine states via W and R relaxation processes. On the other hand, when pumping line 5, only the removal of population from the other hyperfine states is responsible for the buildup in the $|\downarrow\Downarrow\rangle$ state. The absence of a pathway for populating the $|\downarrow\Downarrow\rangle$ state directly from the recombination of D^0X, as in the case of pumping line 5, results in a lower final $|\downarrow\Downarrow\rangle$ population as compared to that seen for pumping line 6.

For the n-type sample from which the spectra shown in FIG. 4.18 were generated, the low energy tail that the hyperfine components develop due to Stark broadening contributes to a reduction of the net electron and nuclear polarizations when pumping one hyperfine component compared to another. This is why pumping line 8, for example, results in lower net polarizations than when pumping line 6. The low energy Stark-broadened tail of line 9 underlies line 8, whereas for line 6 there is no nearby line at higher energy.

When the pump laser is tuned off a peak, the electron and nuclear polarizations are significantly reduced, as seen for $6'$ in FIG. 4.18 and TABLE 4.1. The achievable polarization is therefore likely limited by nonselective photoionization of D^0 in all four hyperfine states by the pump laser due to the tail of the D^0 photoionization continuum. Thus even larger hyperpolarizations could be achieved if the inhomogeneous broadening present in this sample could be reduced, as the sharper (and more intense) lines would mitigate the effects of the nonselective photoionization. At the same time, there would be higher selectivity for one hyperfine state over the other when pumping at the peak of a hyperfine component.

4.2.3 Nuclear polarization dynamics

To be useful for quantum computing and magnetic resonance, spin polarization must occur on a reasonably fast timescale. The detector used in the PLE apparatus is too slow to capture the electron polarization dynamics, but it is still capable of following the time dependence of the nuclear polarization. FIG. 4.22 shows the transient populations of the four D^0 hyperfine states with the pump laser tuned to line 6. The transient when pump and probe are turned on simultaneously is shown for both a fully polarized and a fully depolarized initial state. The transient from a polarized initial state is a fast step function, but from the fully depolarized state FIG. 4.22**a**, **b** and **c** all show an initial overshoot followed by a decay to the steady-state value, due to the transfer of the hyperfine populations to the dominant $|\downarrow\Downarrow\rangle$ state. On the other hand, FIG. 4.22**d** shows that the population in the $|\downarrow\Downarrow\rangle$ state has a buildup following the initial fast transient, with a $\sim$100 ms time scale. FIG. 4.22**c** also shows the transient behaviour for line 4 when the fully saturated sample is allowed to recover in the dark for 20 min. The partial recovery of the unpolarized population indicates that the nuclear spin relaxation time under these conditions is 35 min.

The polarization time and recovery time were measured at double and quadruple the original magnetic field to determine their dependencies on the field. This was done for the case of monitoring line 4 and pumping line 6 as in FIG. 4.22**c**. The results, summarized in TABLE 4.2, suggest that the polarization time goes as B^2 while the recovery time scales linearly with B. Since this data was collected within a limited magnetic field regime, it is not known over how wide a range these relationships hold. An attempt was made at measuring the time constants at one half of the original field, but signal-to-noise issues were encountered which made the data unreliable. This is possibly related to the reduced resolution of the Zeeman splittings at that field. It should be noted that the experimental conditions were not exactly the same as for the previous measurements, which produced the data shown in FIG. 4.22, so the time constants are slightly different, but nevertheless should be consistent amongst themselves.

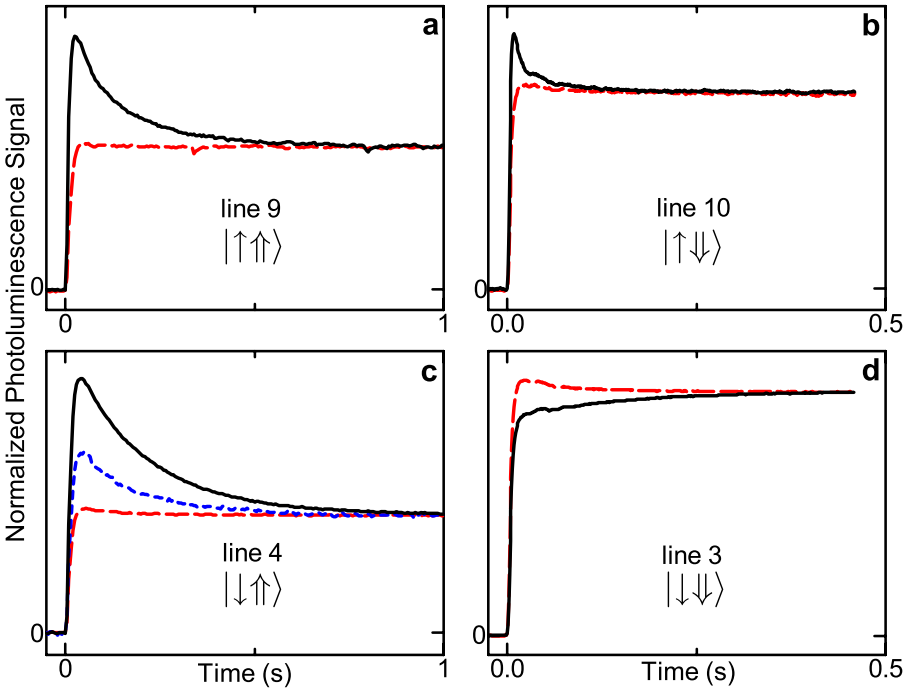

Figure 4.22: The transient behaviour of lines revealing the four D^0 populations are shown, with the pump laser tuned to line 6 in all cases. Pump and probe are switched on simultaneously at $t = 0$. The dashed curves show the transients with the populations in the fully polarized state, while the solid curves show the transients when the populations have been fully equilibrated. The middle curve in **c** shows the transient after the fully polarized sample has recovered in the dark for 20 min.

Table 4.2: Polarization time and recovery time at different magnetic fields for monitoring line 4 and pumping line 6.

B (G)	Polarization Time (s)	Recovery Time (min.)
425	0.29	28
850	1.2	54
1700	4.5	125

4.2.4 Polarization of electron and nuclear spins in p-type ^{28}Si measured using the capacitive photoconductivity method

A contactless capacitive photoconductivity method (as described in Section 3.3.1) was used to measure the electron and nuclear polarizations obtained by dynamic optical pumping using a p-type sample with 99.995% enrichment (^{28}Si Avo), which was the most highly enriched ^{28}Si sample available. At the bottom of FIG. 4.23, is the unpumped spectrum, which shows extremely well resolved hyperfine components, with an average FWHM of 100 neV. The two upper spectra show the photocapacitance signal when either line 6 or line 8 is pumped – the two cases that resulted in the highest polarizations in the n-type sample, as shown in FIG. 4.18 and TABLE 4.1. The polarizations for these two cases are much lower for this p-type sample, with electron polarizations of around 30% and nuclear polarizations of around 15%. This reduced polarization is a result of the use of above-gap excitation that is required to obtain any signal for this p-type sample.

When comparing the pumped spectra for the n-type and p-type ^{28}Si samples in FIG. 4.18 and FIG. 4.23, respectively, it is apparent that for transitions from D^0 states having the same electron spin as the pumped state, the nuclear polarization observed for the p-type sample is in the opposite direction from that seen for the n-type sample, in agreement with the PLE results for the p-type ^{28}Si sample discussed in Section 4.2.1. The resulting net electron and nuclear polarizations, when pumping at the peaks of lines 3 through 10, are summarized in TABLE 4.3.

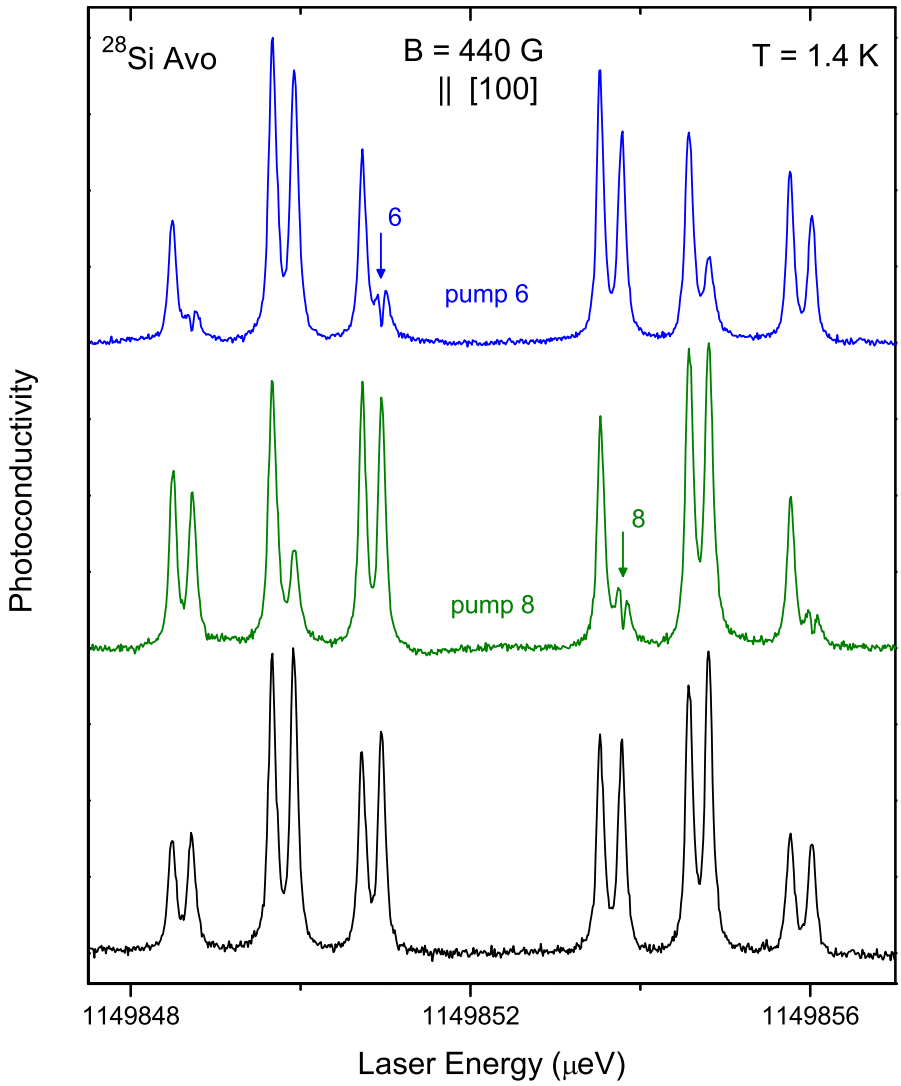

Figure 4.23: Photoconductance spectra of the ^{31}P D^0X in a p-type ^{28}Si sample with 99.995% enrichment (^{28}Si Avo) measured using the contactless capacitive coupling method, revealing electron and nuclear polarizations obtained by selective optical pumping. At the bottom is the spectrum without any resonant pumping, while the two upper spectra result when a strong pump field is tuned to either line 6 or line 8 (as in FIG. 4.18).

Table 4.3: Net electron and nuclear polarizations for optical pumping in p-type ^{28}Si.

Pump line	Polarization(%) Elec.	Nucl.
3 $\|\downarrow\Downarrow\rangle$	26	24
4 $\|\downarrow\Uparrow\rangle$	37	4
5 $\|\uparrow\Uparrow\rangle$	-28	-20
6 $\|\uparrow\Downarrow\rangle$	-29	13
7 $\|\downarrow\Downarrow\rangle$	25	19
8 $\|\downarrow\Uparrow\rangle$	26	-15
9 $\|\uparrow\Uparrow\rangle$	-27	-25
10 $\|\uparrow\Downarrow\rangle$	-38	-6

4.3 Homogeneous linewidth of the ^{31}P D^0X transition in silicon

A feature that is present in the optical pumping spectra shown in the previous section and which has not yet been discussed, is the spectral hole created at the pump laser energy. The observation of a spectral hole in those spectra is significant since it allows for a measurement of the homogeneous linewidth of the ^{31}P D^0X transition, which is important for single centre studies as it gives the bound exciton linewidth that would be observed for a single ^{31}P donor, even in ^{nat}Si.

The homogeneous linewidths of bound exciton transitions in bulk and epitaxial semiconductors has in the past been measured in materials such as nitrogen-doped GaP [88] and for donor bound excitons in GaAs [89] using spectral hole burning, but no such measurements have previously been made for bound excitons in bulk Si. While the narrowest linewidth obtained for those other materials is 70 MHz (∼300 neV), the homogeneous linewidth presented in this section for Si is more than one order of magnitude narrower, as might be expected given the longer exciton lifetimes in Si.

4.3.1 Hole burning in ^{nat}Si

Before presenting the results for ^{28}Si, it is useful to begin with a discussion of the simpler case of burning a spectral hole into the no-phonon ^{31}P D^0X transition in ^{nat}Si at zero field. The bottom spectrum in FIG. 4.24 is the unperturbed PLE spectrum of the ^{31}P D^0X transition in ^{nat}Si, which appears as a single broad line with a FWHM of 4.7 μeV. Directly above it is a spectrum of the same transition, with a 1 W pump beam (∼40 times the PLE probe power) tuned to the centre of the transition. In this case, a spectral hole with a FWHM of ∼70 neV appears at the pump laser energy, and two 'antiholes' (denoted by $*$) – one on either side of the hole – are observed in the PLE spectrum. It is important to realize that the ^{31}P D^0X spectrum observed in FIG. 4.24 is really the superposition of two transitions due to the ^{31}P zero-field hyperfine splitting. This 486 neV (117.53 MHz [56]) splitting is not resolved due to the dominance of inhomogeneous isotope broadening in ^{nat}Si [23], but can be observed

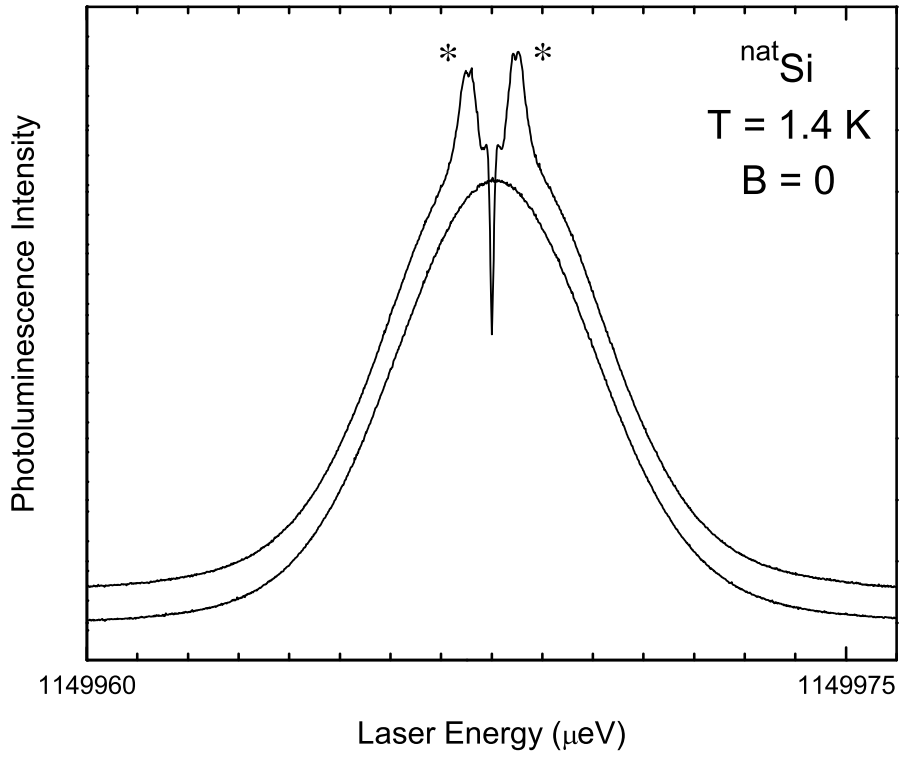

Figure 4.24: PLE spectra of the ^{31}P D^0X in an n-type sample of ^{nat}Si with zero external magnetic field. The lower spectrum shows the PLE signal when no pump laser is present, while directly above it is the resulting PLE spectrum when a strong pump laser is tuned to the centre of the transition, revealing a spectral hole at the pump laser energy and two 'antiholes' (denoted by $*$).

indirectly in the pumped spectrum, where the separation between the hole and either 'antihole' is equal to the zero field hyperfine splitting. The hole burning process is thus the creation of a bound exciton from a donor in either hyperfine state, followed by ionization due to the dominance of Auger decay in silicon, and eventual recapture of a free electron, sometimes resulting in the opposite donor hyperfine state.

In FIG. 4.24, it appears that there is additional structure present on the 'antiholes', making them wider than the spectral hole at the centre of the transition. This is likely due to a residual splitting of the light and heavy hole bands by the inhomogeneous broadening present in the ^{nat}Si sample.

4.3.2 Hole burning in ^{28}Si under an applied magnetic field

The spectrum that results from burning a spectral hole into the ^{31}P D^0X distribution becomes more complex in the presence of an applied magnetic field. For this experiment, an n-type sample of ^{28}Si enriched to 99.92% was used. For this particular sample, the ^{31}P hyperfine splitting is not resolved in the PLE spectrum, but only the six main Zeeman transitions are observed, as this makes any fine structure resulting from the presence of the pump laser more clearly distinguishable. The bottom spectrum in FIG. 4.25 shows the PLE signal for this ^{28}Si sample under an applied magnetic field of 440 G parallel to the [001] axis when no pump laser is present. The electron spin state corresponding to each main transition alternates for successive transitions, while the energies of the nuclear spin states for each underlying hyperfine doublet reverse for sucessive main transitions.

When one of these transitions is pumped, a spectral hole appears at the pump laser energy and additional structure, similar to that seen in the zero field ^{nat}Si pumped spectrum in FIG. 4.24, is observed in some of the other transitions. The top spectrum in FIG. 4.25 shows the PLE signal when the pump laser is tuned to the centre of the (5,6) transition so that both hyperfine components are being pumped simultaneously – the high energy shoulder of component 5 and the low energy shoulder of component 6. An image of the spectral hole (denoted by †) appears at the centre of the (1,2) transition, whose initial state originates from the same electron spin population as the pumped transition. On the other hand, the (7,8) and (11,12) transitions, which have initial states originating from the opposite electron spin population, each exhibit a pair of 'antiholes' (denoted by $*$). Because the energies of the nuclear spin states of the hyperfine doublets reverse for the opposite electron spin, an 'antihole' appears at the low energy shoulder of the lower energy hyperfine component and another appears at the high energy shoulder of the higher energy component, with the separation between the two 'antiholes' being equal to the ^{31}P zero field hyperfine splitting. In this spectrum, the only transitions that exhibit fine structure are those with a D^0X final state that belong to the same hole manifold as the pumped (5,6) transition, which has a $m_h = +1/2$ D^0X final state. This is likely due to the random splitting and broadening of the states in the $m_h = \pm 1/2$ and $m_h = \pm 3/2$ hole manifolds by

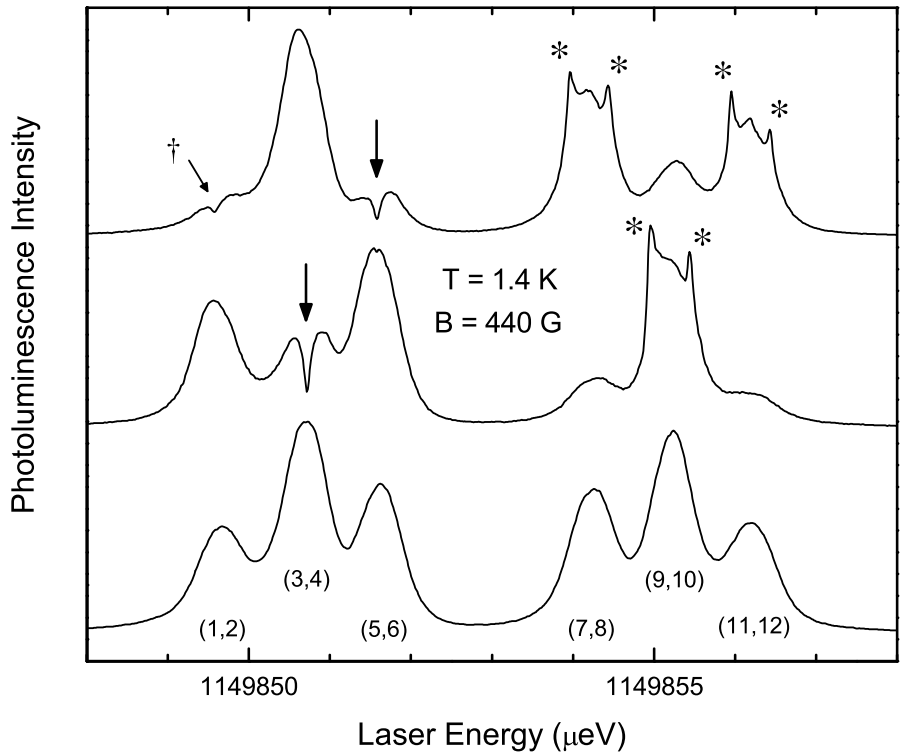

Figure 4.25: PLE spectra of the ^{31}P D^0X in an n-type sample of ^{28}Si with 99.92% enrichment (^{28}Si c), under an applied magnetic field of 440 G parallel to the [001] axis. At the bottom is the spectrum with no optical pumping, showing the six main Zeeman transitions. The hyperfine doublets are not resolved in this sample, but the same 1–12 labels that were used in the previous section to label the resolved transitions in more highly enriched ^{28}Si samples are used here. The middle spectrum shows the resulting PLE signal when the pump laser, indicated by the vertical arrow, is tuned to the centre of the (3,4) transition. The PLE spectrum at the top is for the case when the pump laser, indicated by the vertical arrow, is tuned to the centre of the (5,6) transition. Some of the transitions show images of the spectral hole (†), or 'antiholes' (∗).

the remaining inhomogeneous isotope broadening, which would result in any fine structure present in one hole manifold being smeared out in the other hole manifold. The scenario resulting from pumping the (5,6) transition is further illustrated in FIG. 4.26.

The middle spectrum in FIG. 4.25 shows the PLE signal when the pump laser is tuned to the centre of the (3,4) transition, which has a $m_h = -3/2$ D^0X final state. An 'antihole' pair appears on the (9,10) transition, whose initial state originates from the electron spin population that is not being pumped, while no structure is observed on any of the other transitions, all of which have D^0X final states belonging to the other ($m_h = \pm 1/2$) hole manifold. In both of the pumped spectra in FIG. 4.25, a significant overall electron polarization is observed, but due to the large inhomogeneous width it is much smaller than that seen in more highly enriched samples [90].

It should be noted that a small amount of above-gap excitation, provided by a 1047 nm Nd:YLF laser, was required to produce the spectra in FIG. 4.25. This above-gap excitation was used to moderate the large spin polarizations and saturation effects produced by the PLE pump and probe lasers.

The homogeneous linewidth of the ^{31}P D^0X transition can be determined from the hole burning spectra at pump powers sufficiently low to eliminate any power broadening or saturation effects. The set of spectra in the inset of FIG. 4.27 shows that both the width and depth of the hole increase dramatically with increasing pump power. The observed hole width can be described by a square root dependence on the pump power [91–93]:

$$\Delta E = \Delta E_0 \left(1 + \frac{P}{P_0}\right)^{1/2} \tag{4.10}$$

In Equation 4.10, ΔE is the observed FWHM of the spectral hole, ΔE_0 is the FWHM of the hole in the low power limit (and is also equal to twice the homogeneous linewidth), P is the pump power, and P_0 is the saturation pump power. Note that P_0 is not a fundamental property of the ^{31}P D^0X, but depends on the experimental conditions, especially on the amount of above-gap excitation, which acts to 'heal' the spectral hole. The solid line in FIG. 4.27 represents a fit of the data to Equation 4.10, yielding $\Delta E_0 = 20 \pm 3$ neV, and a homogeneous linewidth of 10 neV, which is ten times as narrow as the best resolved ensemble linewidths observed [94, 95] in ^{28}Si, and is

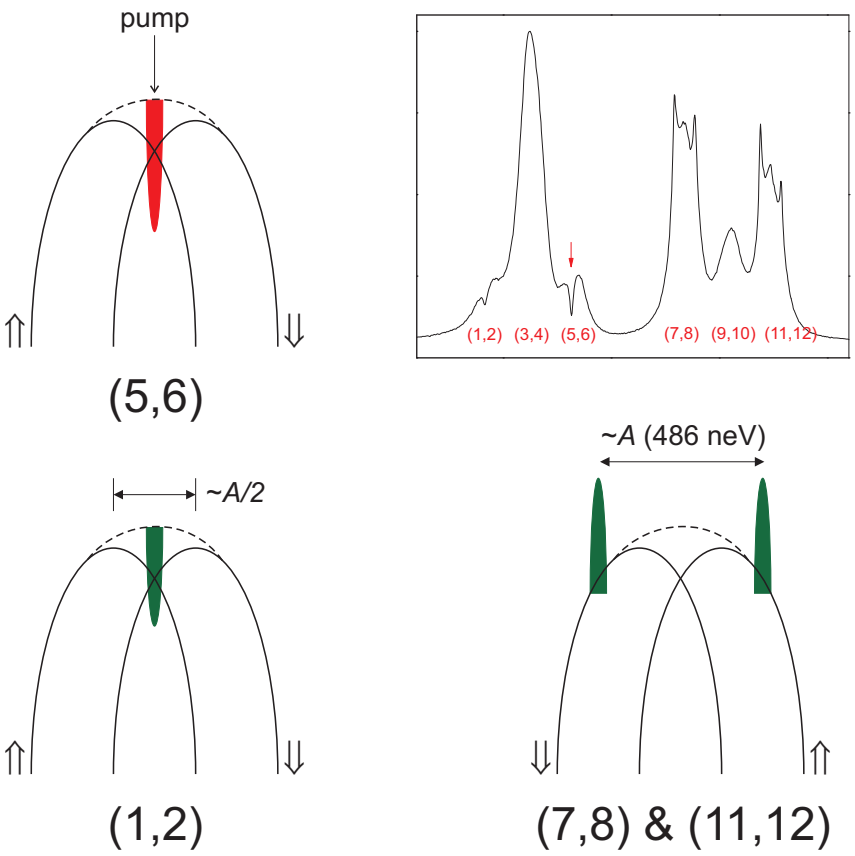

Figure 4.26: When the pump laser is tuned to the centre of the (5,6) transition, a spectral hole appears at the pump laser energy. An image of the hole appears at the centre of the (1,2) transition, while a pair of 'antiholes', separated by the ^{31}P zero field hyperfine splitting, appears on both the (7,8) and the (11,12) transitions. The double arrows beside the transition lines indicate the corresponding nuclear spin states of the lines.

only four times the lifetime limited linewidth set by the ^{31}P D^0X lifetime of 272 ns [55]. For a single centre with a linewidth of 10 neV, the selectivity for one hyperfine state over the other when pumping at the peak of a hyperfine component would be 25000. It is possible that the homogeneous linewidth for transitions to certain ^{31}P D^0X states will become even narrower at higher magnetic fields, as the likelihood of relaxation between different hole states of the ^{31}P D^0X decreases.

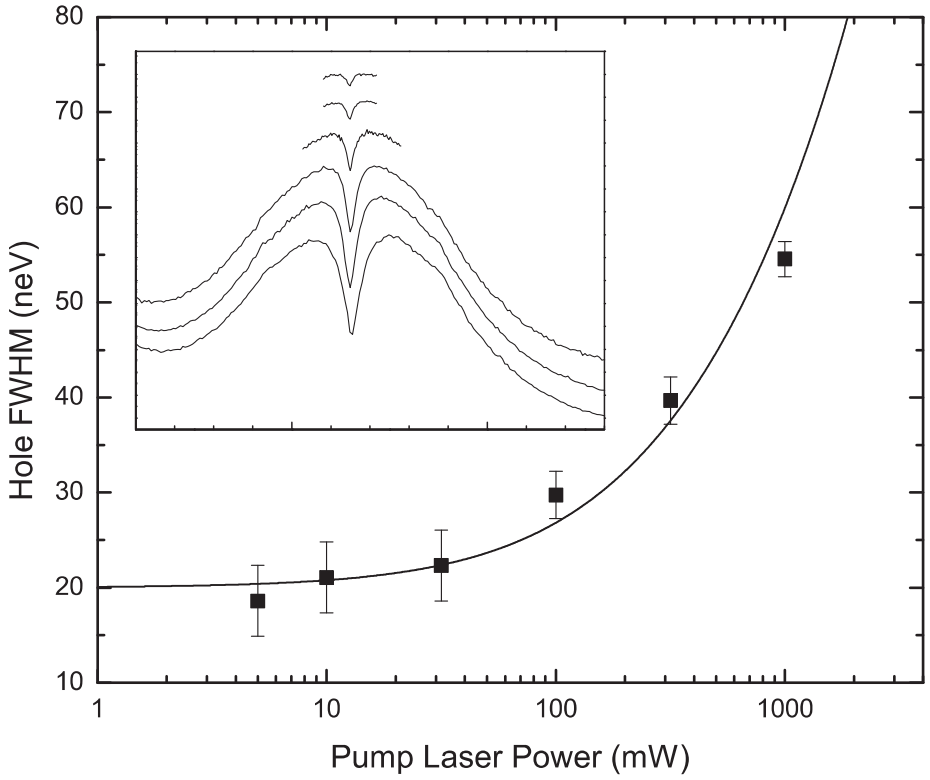

Figure 4.27: The full width at half maximum (FWHM) of the spectral hole, ΔE, with the pump laser at the centre of the (5,6) transition, as at the top of FIG. 4.25, is plotted against the pump laser power, P, for six different power levels ranging from 5 mW to 1000 mW. A fit of this data to Equation 4.10 is represented by the solid line and yields a saturation power of $P_0 = 125 \pm 15\,\mathrm{mW}$ and a hole FWHM of $20 \pm 3\,\mathrm{neV}$ in the low power limit. The PLE spectra of the hole at the six different power levels are shown in the inset, shifted vertically for clarity, with the lowest power spectrum at the top and the highest power one at the bottom (the inset spans $1.2\,\mu\mathrm{eV}$).

Chapter 5

Conclusions

In this thesis, we have presented results obtained from the PLE spectroscopy of the ^{31}P donor bound exciton in highly enriched ^{28}Si. The PLE spectrum of the ^{31}P D^0X ground state transition in the absence of an applied magnetic field revealed a sample-independent splitting approximately equal to 486 neV which was identified as the zero field hyperfine splitting [56] of the ^{31}P D^0 ground state. In this spectrum, we also observed a smaller sample-dependent splitting, which we believe could be due to a random splitting of the normally degenerate light hole and heavy hole bands by the remaining inhomogeneous broadening resulting from the small amounts of ^{29}Si and ^{30}Si present in the samples, or from other impurities such as carbon. Under a small magnetic field ($\sim$500 G) applied parallel to the [001] axis, the PLE spectrum of the ^{31}P D^0X transition revealed a more complex structure consisting of six sets of doublets. The six main transitions are the electric-dipole allowed transitions between the two D^0 Zeeman levels and the four D^0X Zeeman levels while the doublet splitting is due to the ^{31}P donor hyperfine interaction. At intermediate fields this splitting is approximately one half of the zero field hyperfine splitting. The ^{31}P D^0X PLE spectrum was first observed for p-type samples of ^{28}Si, where the use of above band gap excitation was required to produce spectra with well-resolved features. The presence of above-gap excitation (provided by a 1047 nm laser) has the effect of photoneutralizing the ^{31}P donors, which in p-type samples are ionized due to compensation from the higher boron acceptor concentration. Without sufficient above-gap excitation, the transitions become significantly broader and the hyperfine splitting becomes

unresolvable.

The ability to observe the hyperfine splittings in the ^{31}P D^0X spectrum and thus the populations of the four donor hyperfine states, led to the polarization of the electron and nuclear spins of ^{31}P donors by selectively ionizing donors in a specific hyperfine state via optical pumping of a specific hyperfine component in the ^{31}P D^0X spectrum. In our preliminary experiments using p-type ^{28}Si, we were able to achieve net electron and nuclear polarizations of only approximately 50% and 25%, respectively. The above-gap excitation in these experiments, needed to photoneutralize the donors, limited the achievable degree of polarization since it acts to equalize the populations in the four donor hyperfine states. However, an n-type crystal intententionally doped with ^{31}P was grown specifically for our polarization experiments. The use of an n-type sample allowed for optical pumping of the $D^0 \rightarrow D^0X$ transitions without any additional above-gap excitation, resulting in dramatically larger polarizations than those obtained in the preliminary attempts. Indeed, an electron polarization of 90% and a nuclear polarization of 76% were obtained using the new n-type sample. We also studied the nuclear polarization dynamics for this process and found that under the same conditions the nuclear spin polarization occurs with a time constant of $\sim$100 ms and the relaxation time of the nuclear spins is approximately 35 min.

The ^{31}P D^0X spectrum was also observed by detecting the photoconductivity resulting from the nonradiative Auger recombination. This method takes advantage of the low radiative quantum efficiencies of bound excitons in silicon by making use of the near-unity efficiency of the Auger process and detecting the free electrons released in Auger recombination. A variation of the photoconductivity method utilizing a contactless capacitive technique was used to observe the ^{31}P D^0X spectrum in our most highly enriched sample of (p-type) ^{28}Si revealing extremely well resolved hyperfine components with an average linewidth of 100 neV FWHM. This method was also used to measure the electron and nuclear spin polarizations for the same p-type sample. In more highly enriched samples of ^{28}Si, we would expect to see even sharper D^0X transition lines and to achieve even higher electron and nuclear spin polarizations of the ^{31}P donors, provided that the samples are n-type.

The work presented here has potential applications in quantum computing schemes based on the spin states of ^{31}P donors in ^{28}Si [38–40]. The ability to optically hyper-

polarize the electron and nuclear spins simultaneously in less than a second satisfies the requirement of initialization of the spins in a reasonably fast timescale, and the detection of the spin states using the photoconductivity method could potentially be useful as a readout mechanism for single nuclear spins.

We also measured the homogeneous linewidth of the ^{31}P D^0X transition using spectral hole burning and found it to be only four times the limit set by the bound exciton lifetime. This quantity is important for single centre studies as it gives the bound exciton linewidth that would be observed for a single ^{31}P donor, even in ^{nat}Si.

It would be interesting to extend the PLE spectroscopy of the ^{31}P D^0X to higher magnetic fields where the Zeeman splittings of the D^0 and D^0X states become larger than k_BT, and the electron spins are highly polarized at thermal equilibrium. This may result in even higher nuclear spin polarizations with optical pumping than those observed at the intermediate fields used in this study. Going beyond the PLE spectroscopy, we have started investigating hyperpolarized ^{31}P nuclear spins using optically detected NMR. We have recently performed a two-pulse Ramsey fringe experiment to measure the ^{31}P hyperfine constant with a precision of 10 significant figures, improving upon the previous value [56], which is precise to 5 significant figures. Additionally, a three-pulse experiment using the Hahn-echo method allowed for a measurement of the nuclear spin coherence time T_2 of 250 ms at a magnetic field of 845 G. In the near future, this currently ongoing optically detected NMR study will be extended to magnetic fields of over 1 Tesla to measure T_2 times which can be compared with those reported in other studies.

Another direction would be the study of optical transitions of bound excitons associated with shallow donors other than ^{31}P. This has already begun [96], in ^{nat}Si, for the bismuth donor. Bismuth, the deepest group V donor in Si, is an interesting case since it has a hyperfine coupling more than ten times that of ^{31}P, and an $I = 9/2$ nuclear spin, resulting in a rich hyperfine structure.

Bibliography

[1] M. Cardona, P. Etchegoin, H. D. Fuchs, and P. Molinas-Mata. Effects of isotopic disorder and mass on the electronic and vibronic properties of three-, two- and one-dimensional solids. *J. Phys. Condens. Matter*, 5:A61, 1993.

[2] E. E. Haller. Isotopically engineered semiconductors. *J. Appl. Phys.*, 77:2857, 1995.

[3] V. G. Plekhanov. Exciton spectroscopy of isotopic crystals. *Opt. Spectrosc.*, 79:715, 1995.

[4] M. Cardona. Isotopic effects in the phonon and electron dispersion relations of crystals. *Phys. Stat. Solidi (b)*, 220:5, 2000.

[5] M. Cardona and T. Ruf. Phonon self-energies in semiconductors: anharmonic and isotopic contributions. *Solid State Commun.*, 117:201, 2001.

[6] M. Cardona and M. L. W. Thewalt. Isotope effects on the optical spectra of semiconductors. *Rev. Mod. Phys.*, 77:1173, 2005.

[7] A.T. Collins, S.C. Lawson, G. Davies, and H. Kanda. Indirect energy gap of ^{13}c diamond. *Phys. Rev. Lett.*, 65:891, 1990.

[8] K. C. Hass, M. A. Tamor, T. R. Anthony, and W. F. Banholzer. Lattice dynamics and Raman spectra of isotopically mixed diamond. *Phys. Rev. B*, 45:7171, 1992.

[9] P. Etchegoin, J. Weber, M. Cardona, W. L. Hansen, K. Itoh, and E. E. Haller. Isotope effect in Ge: a photoluminescence study. *Solid State Commun.*, 83:843, 1992.

[10] G. Davies, E. C. Lightowlers, K. Itoh, W. L. Hansen, E. E. Haller, and V. Ozhogin. Isotope dependence of the indirect energy gap of germanium. *Semicond. Sci. Technol.*, 7:1271, 1992.

[11] G. Davies, E. C. Lightowlers, T. S. Hui, V. Ozhogin, K. M. Itoh, W. L. Hansen, and E. E. Haller. Isotope dependence of the lowest direct energy gap in crystalline germanium. *Semicond. Sci. Technol.*, 8:2201, 1993.

[12] C. Parks, A. K. Ramdas, S. Rodriguez, K. M. Itoh, and E. E. Haller. Electronic band structure of isotopically pure germanium: Modulated transmission and reflectivity study. *Phys. Rev. B*, 49:14244, 1994.

[13] P. Etchegoin, H. D. Fuchs, J. Weber, M. Cardona, L. Pintschovius, N. Pyka, K. Itoh, and E. E. Haller. Phonons in isotopically disordered Ge. *Phys. Rev. B*, 48:12661, 1993.

[14] H. D. Fuchs, C. H. Grein, C. Thomsen, M. Cardona, W. L. Hansen, E. E. Haller, and K. Itoh. Comparison of the phonon spectra of ^{70}Ge and natural Ge crystals: Effects of isotopic disorder. *Phys. Rev. B*, 43:4835, 1991.

[15] H. D. Fuchs, C. H. Grein, R. I. Devlen, J. Kuhl, and M. Cardona. Anharmonic decay time, isotopic scattering time, and inhomogeneous line broadening of optical phonons in ^{70}Ge, ^{76}Ge, and natural Ge crystals. *Phys. Rev. B*, 44:8633, 1991.

[16] J. M. Zhang, M. Giehler, A. Göbel, T. Ruf, and M. Cardona. Optical phonons in isotopic Ge studied by Raman scattering. *Phys. Rev. B*, 57:1348, 1998.

[17] H. D. Fuchs, C. H. Grein, M. Bauer, and M. Cardona. Infrared absorption in ^{76}Ge and natural Ge crystals: Effects of isotopic disorder on q$\neq$0 phonons. *Phys. Rev. B*, 45:4065, 1992.

[18] A. Göbel, D. T. Wang, M. Cardona, L. Pintschovius, W. Reichardt, J. Kulda, N. M. Pyka, K. Itoh, and E. E. Haller. Effects of isotope disorder on energies and lifetimes of phonons in germanium. *Phys. Rev. B*, 58:10510, 1998.

[19] S. Zollner, M. Cardona, and S. Gopalan. Isotope and temperature shifts of direct and indirect band gaps in diamond-type semiconductors. *Phys. Rev. B*, 45:3376, 1992.

[20] F. Widulle, T. Ruf, A. Göbel, I. Silier, E. Schönherr, M. Cardona, J. Camacho, A. Cantarero, W. Kriegseis, and V. I. Ozhogin. Raman studies of isotope effects in Si and GaAs. *Physica B*, 263B-264B:381, 1999.

[21] F. Widulle, T. Ruf, M. Konumaa, I. Silier, M. Cardona, W. Kriegseis, and V. I. Ozhogin. Isotope effects in elemental semiconductors: a raman study of silicon. *Solid State Commun.*, 118:1–22, 2001.

[22] T. Ruf, R.W. Henn, M. Asen-Palmer, E. Gmelin, M. Cardona, H.-J. Pohl, G. G. Devyatych, and P. G. Sennikov. Thermal conductivity of isotopically-enriched silicon. *Solid State Commun.*, 115:243, 2000.

[23] D. Karaiskaj, M. L. W. Thewalt, T. Ruf, M. Cardona, H.-J. Pohl, G. G. Deviatych, P. G. Sennikov, and H. Riemann. Photoluminescence of Isotopically Purified Silicon: How Sharp are Bound Exciton Transitions? *Phys. Rev. Lett.*, 86:6010, 2001.

[24] D. Karaiskaj, M. L. W. Thewalt, T. Ruf, M. Cardona, and M. Konuma. 'intrinsic' acceptor ground state splitting in silicon: an isotopic effect. *Phys. Rev. Lett.*, 89:016401, 2002.

[25] D. Karaiskaj, M. L. W. Thewalt, T. Ruf, and M. Cardona. Photoluminescence studies of isotopically enriched silicon. *Phys. Status Solidi B*, 235:63, 2002.

[26] M. L. W. Thewalt, D. Karaiskaj, T. Ruf, and M. Cardona. Ultrahigh resolution photoluminescence spectroscopy of isotopically pure silicon. *Inst. Phys. Cong. Ser.*, 171:101, 2003.

[27] D. Karaiskaj, J. A. H. Stotz, T. Meyer, M. L. W. Thewalt, and M. Cardona. Impurity Absorption Spectroscopy in ^{28}Si: The Importance of Inhomogeneous Isotope Broadening. *Phys. Rev. Lett.*, 90:186402, 2003.

[28] M. Steger, A. Yang, D. Karaiskaj, M. L. W. Thewalt, E. E. Haller, J. W. Ager III, M. Cardona, H. Riemann, N. V. Abrosimov, A. V. Gusev, A. D. Bulanov, A. K. Kaliteevskii, O. N. Godisov, P. Becker, H.-J. Pohl, and K. M. Itoh. Shallow Impurity Absorption Spectroscopy in Isotopically Enriched Silicon. *AIP Conf. Proc.*, 893:231, 2007.

[29] M. Steger, A. Yang, D. Karaiskaj, M. L. W. Thewalt, E. E. Haller, J. W. Ager III, M. Cardona, H. Riemann, N. V. Abrosimov, A. V. Gusev, A. D. Bulanov, A. K. Kaliteevskii, O. N. Godisov, P. Becker, and H.-J. Pohl. Shallow impurity absorption spectroscopy in isotopically enriched silicon. *Phys. Rev. B*, 79:205210, 2009.

[30] M. Steger, A.Yang, M. L. W. Thewalt, M. Cardona, H. Riemann, N. V. Abrosimov, M. F. Churbanov, A. V. Gusev, A. D. Bulanov, I. D. Kovalev, A. K. Kaliteevskii, O. N. Godisov, P. Becker, H.-J. Pohl, J. W. Ager III, and E. E. Haller. Impurity absorption spectroscopy of the deep double donor sulfur in isotopically enriched silicon. *Physica B*, 401-402:600–603, 2007.

[31] M. Steger, A. Yang, M. L. W. Thewalt, M. Cardona, H. Riemann, N. V. Abrosimov, M. F. Churbanov, A. V. Gusev, A. D. Bulanov, I. D. Kovalev, A. K. Kaliteevskii, O. N. Godisov, P. Becker, H.-J. Pohl, E. E. Haller, and J. W. Ager III. High-resolution absorption spectroscopy of the deep impurities S and Se in ^{28}Si revealing the ^{77}Se hyperfine splitting. *Phys. Rev. B*, 80:115204, 2009.

[32] M. L. W. Thewalt, M. Steger, A. Yang, N. Stavrias, M. Cardona, H. Riemann, N. V. Abrosimov, M. F. Churbanov, A. V. Gusev, A. D. Bulanov, I. D. Kovalev, A. K. Kaliteevskii, O. N. Godisov, P. Becker, H.-J. Pohl, J. W. Ager III, and E.E. Haller. Can highly enriched ^{28}Si reveal new things about old defects? *Physica B*, 401-402:587–592, 2007.

[33] A. Yang, M. Steger, M. L. W. Thewalt, M. Cardona, H. Riemann, N. V. Abrosimov, M. F. Churbanov, A. V. Gusev, A. D. Bulanov, I. D. Kovalev, A. K. Kaliteevskii, O. N. Godisov, P. Becker, H.-J. Pohl, J. W. Ager III, and E.E. Haller. High resolution photoluminescence of sulfur- and copper-related isoelectronic bound excitons in highly enriched ^{28}Si. *Physica B*, 401-402:593–596, 2007.

[34] M. Steger, A.Yang, N. Stavrias, M. L. W. Thewalt, H. Riemann, N. V. Abrosimov, M. F. Churbanov, A. V. Gusev, A. D. Bulanov, I. D. Kovalev, A. K. Kaliteevskii, O. N. Godisov, P. Becker, and H.-J. Pohl. Reduction of the linewidths of deep luminescence centers in ^{28}Si reveal fingerprints of the isotope constituents. *Phys. Rev. Lett.*, 100:177402, 2008.

[35] M. Steger, T. Sekiguchi A. Yang, K. Saeedi, M. L. W. Thewalt, M. O. Henry, K. Johnston, H. Riemann, N. V. Abrosimov, M. F. Churbanov, A. V. Gusev, A. D. Bulanov, A. K. Kaliteevskii, O. N. Godisov, P. Becker, and H.-J. Pohl. Isotopic fingerprints of gold-containing luminescence centers in ^{28}Si. *Physica B*, 404:5050, 2009.

[36] M. Cardona, T. A. Meyer, and M. L. W. Thewalt. Temperature dependence of the energy gap of semiconductors in the low temperature limit. *Phys. Rev. Lett.*, 92:196403–1 to 4, 2004.

[37] A. Yang, M. Steger, T. Sekiguchi, D. Karaiskaj, M. L. W. Thewalt, M. Cardona, K. Itoh, H. Riemann, N. V. Abrosimov, M. F. Churbanov, A. V. Gusev, A. D. Bulanov, I. D. Kovalev, A. K. Kaliteevskii, O. N. Godisov, P. Becker, H.-J. Pohl, J. W. Ager III, and E. E. Haller. Single-frequency laser spectroscopy of the boron bound exciton in ^{28}Si. *Phys. Rev. B*, 80:195203, 2009.

[38] B. E. Kane. A silicon-based nuclear spin quantum computer. *Nature*, 393:133, 1998.

[39] D. P. DiVincenzo. The physical implementation of quantum computation. *Fortschr. Phys.*, 48:771, 2000.

[40] R. Vrijen, E. Yablonovitch, K. Wang, H. W. Jiang, A. Balandin, V. Roychowdhury, T. Mor, and D. P. DiVincenzo. Electron-spin-resonance transistors for quantum computing in silicon-germanium heterostructures. *Phys. Rev. A*, 62:012306, 2000.

[41] C. Hamaguchi. *Basic semiconductor physics*. Springer-Verlag, Berlin, 2001.

[42] Landolt-Börnstein. *Numerical Data and Functional Relationships in Science and Technology, New Series, group III, vol. 22, Semiconductors, subvolume b.* Springer-Verlag, Berlin, 1989.

[43] P. Y. Yu and M. Cardona. *Fundamentals of Semiconductors: Physics and Materials Properties.* Springer, Berlin, 2005.

[44] W. Kohn. *Shallow Impurity States in Silicon and Germanium, in Vol. 5 of Solid State Physics.* Academic Press, New York, 1957.

[45] W. Kohn. Shallow impurity states in semiconductors. *Nuovo Cimento*, 7:713, 1958.

[46] G. F. Koster. *Space groups and their representations, in Vol. 5 of Solid State Physics.* Academic Press, New York, 1957.

[47] T. M. Rice. *in Vol. 32 of Solid State Physics.* Academic Press, New York, 1977.

[48] O. Madelung. *Introduction to solid-state theory, in Vol. 2 of Springer series in solid state science.* Springer-Verlag, Berlin, 1978.

[49] M. A. Lampert. Mobile and Immobile Effective-Mass-Particle Complexes in Nonmetallic Solids. *Phys. Rev. Lett.*, 1:450, 1958.

[50] J. R. Haynes. Experimental Proof of the Existence of a New Electronic Complex in Silicon. *Phys. Rev. Lett.*, 4:361, 1960.

[51] M. Tajima. Determination of boron and phosphorus concentration in silicon by photoluminescence analysis. *Appl. Phys. Lett.*, 32:719, 1978.

[52] K. Nishikawa and R. Barrie. Phonon broadening of impurity spectral lines. I. General theory. *Can. J. Phys.*, 41:1135, 1963.

[53] G. Kirczenow. A new model for bound multiexciton complexes. *Solid State Commun.*, 21:713, 1977.

[54] G. Kirczenow. A shell model of bound multiexciton complexes in silicon.

[55] W. Schmid. Auger lifetimes for excitons bound to neutral donors and acceptors in Si. *Phys. Stat. Sol. (b)*, 84:529, 1977.

[56] G. Feher. Electron spin resonance experiments on donors in silicon. i. electronic structure of donors by the electron nuclear double resonance technique.

[57] A. S. Kaminskii, L. I. Kolesnik, B. M. Leiferov, and Ya. E. Pokrovskii. Luminescence analysis of group III and V impurities in silicon. *Zh. Prikl. Spektrosk.*, 36:745, 1982.

[58] P. McColley and E. C. Lightowlers. Calibration of the photoluminescence technique for measuring B, P and Al concentrations in Si in the range 10^{12} to 10^{15} cm^{-3} using Fourier transform spectroscopy. *Semicond. Sci. Technol.*, 2:157, 1987.

[59] M. Tajima, T. Masui, D. Itoh, and T. Nishino. Calibration of the Photoluminescence Method for Determining As and Al Concentrations in Si. *J. Electrochem. Soc.*, 137:3544, 1990.

[60] I. Pelant, J. Dian, J. Matouskova, J. Valenta, J. Hala, M. Ambroz, M. Vacha, V. Kohlova, K. Vojtechovsky, and K. Kaslik. Photoluminescence assessment of B, P, and Al in Si wafers: The problem of sample heating by a laser beam. *J. Appl. Phys.*, 73:3477, 1993.

[61] I. Broussell, J. A. H. Stotz, and M. L. W. Thewalt. Method for shallow impurity characterization in ultrapure silicon using photoluminescence. *J. Appl. Phys.*, 92:5913, 2002.

[62] P. Becker, D. Schiel, H.-J. Pohl, A. K. Kaliteevski, O. N. Godisov, M. F. Churbanov, G. G. Devyatykh, A. V. Gusev, A. D. Bulanov, S. A. Adamchik, V. A. Gavva, I. D. Kovalev, N. V. Abrosimov, B. Hallmann-Seiffert, H. Riemann, S. Valkiers, P. Taylor, P. de Bievre, and E. M. Dianov. Large-scale production of highly enriched ^{28}Si for the precise determination of the Avogadro constant. *Meas. Sci. Technol.*, 17:1854, 2006.

[63] R. C. Jaeger. *Introduction to Microelectronic Fabrication.* Prentice Hall, Upper Saddle River, NJ, 2001.

[64] W. Keller and A. Mühlbauer. *Float zone silicon, in Vol. 5 of Preparation and properties of solid state materials*. Marcel Dekker, New York, 1981.

[65] A. N. Safonov, G. Davies, and E. C. Lightowlers. Lineshape of the no-phonon luminescence of excitons bound to phosphorus in carbon-doped silicon. *Phys. Rev. B*, 54:4409, 1996.

[66] W. Burger and K. Lassman. Continuous high-resolution phonon spectroscopy up to 12 meV: Measurement of the A^+ binding energies in silicon. *Phys. Rev. B*, 33:5868, 1986.

[67] B. Pajot. *Semiconducting and Insulating Crystals, Optical Absorption of Impurities and Defects: Volume 1: Hydrogen-like Centres*. Springer, New York, 2009.

[68] A. S. Kaminskii, V. A. Karasyuk, and Ya. E. Pokrovskii. Luminescence of excitons bound to phosphorus atoms in silicon subjected to a magnetic field. *Sov. Phys. JETP*, 52:211, 1980.

[69] G. P. Berman, G. D. Doolen, P. C. Hammel, and V. I. Tsifrinovich. Magnetic Resonance Force Microscopy Quantum Computer with Tellurium Donors in Silicon. *Phys. Rev. Lett.*, 86:2894, 2001.

[70] K. M. Itoh. An all-silicon linear chain NMR quantum computer. *Solid State Commun.*, 133:747, 2005.

[71] K.-M. C. Fu, T. D. Ladd, C. Santori, and Y. Yamamoto. Optical detection of the spin state of a single nucleus in silicon. *Phys. Rev. B*, 69:125306, 2004.

[72] J. J. L. Morton, A. M. Tyryshkin, R. M. Brown, S. Shankar, B. W. Lovett, A. Ardavan, T. Schenkel, E. E. Haller, J. W. Ager, and S. A. Lyon. Solid-state quantum memory using the ^{31}P nuclear spin. *Nature*, 455:1085, 2008.

[73] T. D. Ladd, J. R. Goldman, F. Yamaguchi, Y. Yamamoto, E. Abe, and K. M. Itoh. All-Silicon Quantum Computer. *Phys. Rev. Lett.*, 89:017901, 2002.

[74] A. M. Tyryshkin, S. A. Lyon, A. V. Astashkin, and A. M. Raitsimring. Electron spin relaxation times of phosphorus donors in silicon. *Phys. Rev. B*, 68:193207, 2003.

[75] A. M. Tyryshkin, J. J. L. Morton, A. Ardavan, and S. A. Lyon. Davies electron-nuclear double resonance revisited: Enhanced sensitivity and nuclear spin relaxation. *J. Chem. Phys.*, 124:234508, 2006.

[76] T. D. Ladd, D. Maryenko, Y. Yamamoto, E. Abe, and K. M. Itoh. Coherence time of decoupled nuclear spins in silicon. *Phys. Rev. B*, 71:014401, 2005.

[77] G. Feher and E. A. Gere. Polarization of Phosphorus Nuclei in Silicon. *Phys. Rev.*, 103:501, 1956.

[78] A. Abragam, J. Combrisson, and I. Solomon. Dynamic polarization of ^{29}Si in silicon. *C. R. Acad. Sc. Paris*, 246:1035, 1958.

[79] G. Feher. Nuclear polarization via hot conduction electrons.

[80] W. G. Clark and G. Feher. Nuclear Polarization in InSb by a dc Current. *Phys. Rev. Lett.*, 10:134, 1959.

[81] G. Lampel. Nuclear Dynamic Polarization by Optical Electronic Saturation and Optical Pumping in Semiconductors. *Phys. Rev. Lett.*, 20:491, 1968.

[82] N. T. Bagraev and L. S. Vlasenko. Optical Polarization of Lattice Nuclei in Strongly Deformed Silicon. *Sov. Phys. Solid State*, 24:1974, 1982.

[83] A. S. Verhulst, I. G. Rau, Y. Yamamoto, and K. M. Itoh. Optical pumping of ^{29}Si nuclear spins in bulk silicon at high magnetic field and liquid helium temperature. *Phys. Rev. B*, 71:235206, 2005.

[84] H. Hayashi, W. Ko, T. Itahashi, A. Sagara, K. M. Itoh, L. S. Vlasenko, and M. P. Vlasenko. Dynamic nuclear polarization of ^{29}Si nuclei in the isotope enriched n-type silicon. *Phys. Status Solidi c*, 3:4388, 2006.

[85] L. S. Vlasenko, M. P. Vlasenko, D. S. Poloskin, R. Laiho, H. Hayashi, T. Itahashi, A. Sagara, and K. M. Itoh. Electron paramagnetic resonance and dynamic nuclear polarization via the photoexcited triplet states of radiation defects in natural and ^{29}Si isotope enriched silicon. *Phys. Status Solidi c*, 3:4376, 2006.

[86] D. R. McCamey, J. van Tol, G. W. Morley, and C. Boehme. Fast Nuclear Spin Hyperpolarization of Phosphorus in Silicon. *Phys. Rev. Lett.*, 102:027601, 2009.

[87] A. Yang, M. Steger, M. L. W. Thewalt, T. D. Ladd, K. M. Itoh, E. E. Haller, J. W. Ager III, H. Riemann, N. V. Abrosimov, P. Becker, and H.-J. Pohl. Nuclear Polarization of Phosphorus Donors in ^{28}Si by Selective Optical Pumping. *AIP Conf. Proc.*, 1199:375–376, 2010.

[88] R. T. Harley and R. M. Macfarlane. Saturation spectroscopy of bound excitons in GaP:N. *J. Phys. C: Solid State Phys.*, 16:L1121, 1983.

[89] H. Oohashi, H. Ando, and H. Kanbe. Homogeneous linewidth of bound excitons in high-purity GaAs measured by spectral hole burning. *Phys. Rev. B*, 54:4702, 1996.

[90] A. Yang, M. Steger, T. Sekiguchi, M. L. W. Thewalt, T. D. Ladd, K. M. Itoh, H. Riemann, N. V. Abrosimov, P. Becker, and H.-J. Pohl. Simultaneous Subsecond Hyperpolarization of the Nuclear and Electron Spins of Phosphorus in Silicon by Optical Pumping of Exciton Transitions. *Phys. Rev. Lett.*, 102:257401, 2009.

[91] A. E. Siegman. *Lasers*. University Science Books, Sausalito, CA, 1986.

[92] L. Allen and J. H. Eberly. *Optical Resonance and Two-Level Atoms, 2nd ed.* Dover, New York, 1987.

[93] J. J. Berry, M. J. Stevens, R. P. Mirin, and K. L. Silverman. High-resolution spectral hole burning in InGaAs-GaAs quantum dots. *Appl. Phys. Lett.*, 88:061114, 2006.

[94] A. Yang, M. Steger, D. Karaiskaj, M. L. W. Thewalt, M. Cardona, K. M. Itoh, H. Riemann, N. V. Abrosimov, M. F. Churbanov, A. V. Gusev, A. D. Bulanov,

A. K. Kaliteevskii, O. N. Godisov, P. Becker, H.-J. Pohl, J. W. Ager III, and E. E. Haller. Optical Detection and Ionization of Donors in Specific Electronic and Nuclear Spin States. *Phys. Rev. Lett.*, 97:227401, 2006.

[95] M. L. W. Thewalt, A. Yang, M. Steger, D. Karaiskaj, M. Cardona, H. Riemann, N. V. Abrosimov, A. V. Gusev, A. D. Bulanov, I. D. Kovalev, A. K. Kaliteevskii, O. N. Godisov, P. Becker, H.-J. Pohl, E. E. Haller, J. W. Ager III, and K. M. Itoh. Direct observation of the donor nuclear spin in a near-gap bound exciton transition: ^{31}P in highly enriched ^{28}Si. *J. Appl. Phys.*, 101:081724, 2007.

[96] T. Sekiguchi, M. Steger, K. Saeedi, M. L. W. Thewalt1, H. Riemann, N. V. Abrosimov, , and N. Nötzel. Hyperfine Structure and Nuclear Hyperpolarization Observed in the Bound Exciton Luminescence of Bi Donors in Natural Si. *Phys. Rev. Lett.*, 104:137402, 2010.